Overcorrected Implants for Total Shoulder Arthroplasty

Présentée le 28 janvier 2021

Faculté des sciences et techniques de l'ingénieur
Laboratoire de biomécanique en orthopédie
Programme doctoral en mécanique

pour l'obtention du grade de Docteur ès Sciences

par

Yasmine BOULANAACHE

Acceptée sur proposition du jury

Prof. C. Ancey, président du jury
Prof. D. Pioletti, Dr A. Terrier, directeurs de thèse
Prof. Ph. Buechler, rapporteur
Dr E. Dall'Ara , rapporteur
Prof. J. M. Kolinski, rapporteur

École
polytechnique
fédérale
de Lausanne

2021

Acknowledgements

Abstract

Glenohumeral osteoarthritis is a degenerative shoulder joint disease, which causes the breakdown of articular cartilage and bone. People affected by this disease suffer from severe pain and eventually reduced mobility and poor life quality. This disease is unfortunately prevalent in the elderly population. In most advanced cases, a total joint replacement or total shoulder arthroplasty (TSA) is needed. There are two types of TSA: the anatomical Total Shoulder Arthroplasty (aTSA) and the reverse Total Shoulder Arthroplasty (rTSA). aTSA is usually performed in cases of intact rotator cuff muscles. It involves the replacement of the damaged cartilage and exposed bones by prostheses, thereby re-establishing the relative motion of the joint and dramatically reducing pain. As a result, basic human functions such as lifting a coffee pot or combing one's hair are restored. With the elderly population constantly growing, the number of aTSAs performed each year is increasing: in Switzerland, the hospitalization rate due to shoulder problems has exceeded the number due to other injuries for the first time in 2013. However, although the aTSA is usually an excellent procedure, its failure rate is relatively high mostly because of the aseptic glenoid implant loosening, often associated to an unstable loading on the glenoid implant. This instability may be reinforced by the presence of glenohumeral subluxation, defined as the relative position of the humeral head with respect to the glenoid fossa.

A new design of prosthesis, called overcorrected (OC) prosthesis, was proposed as a means to reduce the postoperative subluxation; however, it was never tested experimentally nor clinically. The objective of this thesis was to evaluate the potential of posterior OC implants on the reduction of posterior subluxation of patients planned for aTSA. Due to inherent difficulties in acquiring in-vivo measurements as well as testing prosthesis designs on real-life patients, finite element (FE) models have been developed worldwide with the aim of first describing then predicting shoulder biomechanical behavior under various conditions. Thus, a patient-specific FE model of the glenoid bone bone after aTSA was developed in order to compare OC versus standard implants. This FE model was based on patients of the Lausanne University Hospital (CHUV) who were planned for aTSA, and required three main steps:

First, it was important for the FE model to account for patient-specific anthropometric data such as glenoid orientations, glenoid density or muscle strength, responsible for movements. Based on the patients' pre-operative computed tomography (CT) data, the glenoid bone FE model of each patient was developed. Virtual

implant placement was performed for each FE model, replicating preoperative planning and matching post-operative CT.

Second, patient-specific loading was computed thanks to a patient-specific musculoskeletal model (MSM). This MSM allowed the evaluation of the joint reaction force during activities of daily living such as lifting a coffee cup or combing one's hair. As such, each of the patient's FE model contained patient-specific anatomical information and patient-specific glenohumeral loading for three activities of daily living.

Third, this FE model required a material law for the bone in order to predict the bone reaction to the implant design. In order to evaluate this material law, two parts were required. First, an experimental set-up involving Digital Volume Correlation (DVC) was designed. DVC is a recent noninvasive technique, which enables the measurement of displacement and deformation in 3D, usually at the micro-level using a micro-CT (μCT) scanner. In this part of the project, cadaveric implanted glenoids were loaded in a μCT-compatible device and scanned before and during loading. DVC was used to extract displacement and compressive strain at the peri-implant area, with an accuracy of 694.3 με and a precision of 440.3 με. Displacement random error was 6.1 μm. In the second part, FE models replicating the experiment were developed with the first goal of predicting the displacement and strain measured by DVC and the secondary goal of finding the most suitable bone material law that enabled a good replication of the experiment. Five specimen-specific FE models were created. While the displacement was very well replicated (Slope =1.0, R^2 = 1.0), the strain was poorly replicated (Slope = 0.51 - 0.70, R^2 = 0.28 - 0.37).

The workflow and the most suitable material law found in the above-described part of the thesis were used to create patient-specific FE models that compared OC to standard implants. First results indicate that the OC design can reduce subluxation without over-constraining the underlying bone. It would be interesting to extend this study to a larger population to confirm the potential advantage of the OC implants over standard ones.

To conclude, this thesis presents a framework to create advanced patient-specific numerical models of the glenohumeral joint after aTSA, which are able to include patient's anthropometric data and patient-specific loading conditions. The latter entails also the ability to replicate activities of daily living. This framework is composed of (i) a procedure to convert preoperative CT data in patient-specific FE models of the glenoid bone after aTSA; (ii) a patient-specific MSM able to evaluate the glenohumeral joint reaction forces; (iii) an experimentally validated bone material law to evaluate the behavior of novel prosthetic designs in a simulated environment. This work is a first step towards the development of a computer tool to assess optimal implant design, implantation strategy, as well as to offer personalized predictions in the clinic.

Keywords

Shoulder, glenoid, anatomical total shoulder arthroplasty, finite element, musculoskeletal model, micro-CT, digital volume correlation, glenoid strain.

Résumé

L'arthrose gléno-humérale ou omarthrose est une pathologie dégénérative de l'épaule qui se traduit par la dégradation progressive du cartilage qui recouvre l'os. Cette pathologie s'accompagne de douleurs aiguës et d'une réduction progressive de la mobilité dans l'articulation et par conséquent d'une détérioration de la qualité de vie. Cette pathologie touche le plus souvent la population âgée. Dans les cas les plus avancés d'omarthrose, le remplacement articulaire de l'épaule par une prothèse, plus communément appelé l'arthroplastie d'épaule, est fortement conseillé. Il existe actuellement deux types d'arthroplastie d'épaule : le premier consiste à remplacer l'articulation par une prothèse totale d'épaule de type anatomique (PTEa) et le second par une prothèse totale d'épaule de type inversée (PTEi). Cette dernière est utilisée dans le cas où les muscles de la coiffe des rotateurs ne sont pas endommagés. L'arthroplastie d'épaule de type anatomique remplace le cartilage endommagé et les os exposés par des prothèses, rétablit le mouvement dans l'articulation et réduit fortement les douleurs. Ainsi les fonctions humaines basiques telles que prendre une tasse de café ou se coiffer les cheveux sont restituées. Avec le vieillissement de la population, the nombre de PTEa implantées augmente : en Suisse, le nombre d'hospitalisations dûes à des pathologies de l'épaule a dépassé, pour la 1ère fois en 2013, le nombre d'hospitalisations dûes à d'autres pathologies. Bien que l'arthroplastie d'épaule de type anatomique soit une chirurgie réussie, son taux de complications reste élevé. Le descellement aseptique du composant glénoïdien en est l'une des principales complications. Une charge excentrée sur le composant glénoïdien entrainant une instabilité est souvent citée comme cause de ce descellement. Cette instabilité peut être accentuée par la présence de subluxation, définie par la position de la tête humérale relative à la cavité glénoïde.

Un nouveau concept de prothèse, appelée prothèse « surcorrigée », a été proposé pour palier à une éventuelle subluxation postopératoire récurrente mais n'a jamais été testé cliniquement. L'objectif principal de cette thèse est donc d'évaluer le potentiel de cette prothèse surcorrigée à réduire la subluxation postérieure chez les patients ayant besoin d'une PTEa.

Il est difficile voire impossible d'effectuer certaines mesures in-vivo ou de tester des concepts de prothèses sur des patients. Pour cette raison, le développement de modèles numériques est en plein essor, leur but étant d'évaluer puis de prédire le fonctionnement de l'épaule sous différentes conditions. Ainsi, un modèle par éléments finis (FE) de l'épaule, spécifique au patient, a été développé afin de comparer la prothèse stan-

dard et la prothèse surcorrigée. Ce modèle numérique est basé sur des patients du Centre Hospitalier Universitaire Vaudois (CHUV) qui avaient une pose de PTEa prévue. Ce modèle a été développé suivant ces trois axes :

En premier lieu, il était important que le modèle FE contienne les données anthropométriques spécifiques à chacun de ces patients comme l'orientation de la glène, la densité osseuse ou encore la force musculaire, responsables du fonctionnement de l'épaule. Les tomodensitogrammes pré-chirurgicaux de la glène ont permis la construction du modèle FE pour chacun des patients. La PTEa a été implantée virtuellement dans chaque modèle FE et a pu être placée correctement en suivant la planification chirurgicale et en se basant sur les tomodensitogrammes post-chirurgicaux.

En second lieu, la force gléno-humérale (GHF) prédite durant des activités de la vie quotidienne telles que prendre une tasse de café ou se coiffer les cheveux, a été calculée grâce à un modèle musculosquelettique (MSM) spécifique à chaque patient. Ainsi, chacun des modèles FE proposés contient les données anatomiques ainsi que la GHF spécifique au patient et prédite pour trois activités de la vie quotidienne.

En troisième lieu, le modèle FE requiert une loi de comportement des matériaux de l'os afin de prédire la réaction de ce dernier face à différents concepts de prothèses. Pour cela, deux étapes ont été nécessaires : dans la première, un dispositif expérimental de Corrélation Volumique Numérique (communément appelée DVC) a été développé. DVC est une technique de mesure non-invasive permettant la mesure de champs de déplacement et de déformation en trois dimensions, à l'échelle microscopique et avec l'aide d'un micro tomographe (μCT). Dans cette partie du projet, des glènes cadavériques ont été implantées avec des prothèses standard, puis mises sous charge dans un μCT et scannées avant et durant la mise en charge. La méthode DVC a été utilisée pour mesurer les champs de déplacement et de compression dans la région autour de la prothèse avec une exactitude de 694.3 με et une précision de 440.3 με. L'erreur aléatoire de déplacement s'est élevée à 6.1 μm. La seconde partie consistait à construire des modèles FE répliquant l'expérience afin de prédire les champs de déplacement et compression ainsi que de trouver la meilleure loi de comportement de matériaux de l'os permettant une bonne réplication de l'expérience. Un modèle FE pour chacun des cinq spécimens mis sous charge a été créé. Le déplacement prédit par le modèle FE présentait une très bonne corrélation avec l'expérience (coefficient de détermination R^2 = 1.0 et pente =1.0) mais les champs de compression n'ont pas été assez bien corrélés (R^2 = 0.28-0.37 et pente = 0.51-0.70).

La loi de comportement de matériaux ainsi que les étapes requises pour le développement du modèle FE ont été utilisés pour créer des modèles FE spécifiques aux patients afin de comparer numériquement les deux concepts de prothèses standard et surcorrigée. Les résultats préliminaires indiquent que le concept de prothèse surcorrigée réduit le risque de subluxation postopératoire sans pour autant surcontraindre l'os. Il serait

intéressant d'étendre cette étude à une plus large population afin de confirmer l'avantage de la prothèse surcorrigée.

Pour conclure, cette thèse propose une structure pour créer des modèles par éléments finis de l'articulation gléno-humérale spécifiques à des patients ayant besoin d'une PTEa. Ces modèles contiennent des données anthropométriques et anatomiques de chaque patient ainsi que la force gléno-humérale spécifique à chacun et à certaines activités de la vie quotidienne. Cette structure est composée comme suit : i) une méthode de conversion des tomodensitogrammes pré-chirurgicaux en modèles par éléments finis de l'os, ii) un modèle musculosquelettique spécifique à chaque patient permettant de prédire la force gléno-humérale, iii) une loi de comportement de matériaux validée expérimentalement permettant l'évaluation du comportement osseux en présence de différents concepts de prothèses. Ce travail est une première étape vers le développement d'un outil numérique qui permettrait la sélection du concept de prothèse idéal, de la meilleure stratégie d'implantation ainsi que d'un diagnostic personnalisé dans un contexte clinique.

Mots-clés

Épaule, glène, arthroplastie totale de l'épaule de type anatomique, éléments finis, modèle musculosquelettique, micro tomographe, corrélation volumique numérique, contraintes sur la glène.

Contents

List of Figures

List of Tables

List of Equations

Chapter 1   Introduction

1.1   Clinical Background

Daily activities such as moving the arms, grabbing, lifting and sports such as swimming and climbing are pos-sible due to the large and complex joint known as shoulder. It is composed of four bones: the humerus, the scapula (commonly known as shoulder blade), the clavicle (commonly known as collarbone) and the sternum [1]. The shoulder is composed of four joints: the glenohumeral (GH) joint, the acromioclavicular (AC) joint, the sternoclavicular (SC) joint and the scapulothoracic (SC) joint. The coordination of these four joints and their associated bone segments and muscles enables the shoulder function (Figure 1:1).
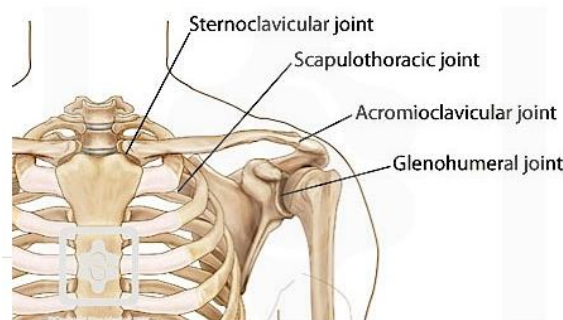
Figure 1:1 Joints of the Shoulder Complex.

(Image courtesy of https://www.physio-pedia.com/Shoulder)

The GH joint is the main joint of the shoulder, accounting for about two thirds of its range of motion. It is generally described as a synovial ball-and-socket joint where the humeral head (ball) is received into the glenoid cavity (socket) [2]. Due to the much smaller concavity of the glenoid fossa, the humeral head is able to slide over the surface of the glenoid fossa enabling complex movements and an extended range of motion. Indeed, the GH joint displays the highest range of motion of any joint in the human body. Nonetheless, this high mobility comes at the price of stability [1]. Stability is achieved through a complex mechanism of active (muscles) and passive stabilizers. The four rotator cuff muscles are known to provide one of the main mech-anisms of shoulder stabilization, those muscles are the Supraspinatus, Subscapularis, Infraspinatus and Teres

Minor (Figure 1:2). They all arise from the scapula and attach to the humeral head [2–4]. The passive stabilizers are composed by the glenohumeral capsule, the labrum, the bursae and all the ligaments of the shoulder [5] (Figure 1:3).
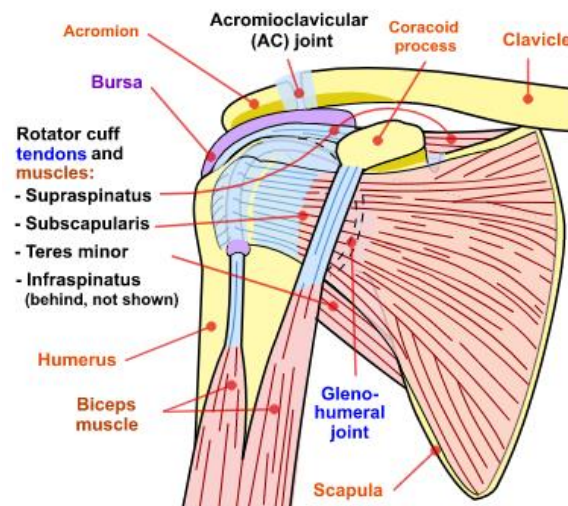
Figure 1:2 Rotator cuff muscles of the shoulder.

(Image courtesy of National Institute Of Arthritis And Musculoskeletal And Skin Diseases, NIAMS.)
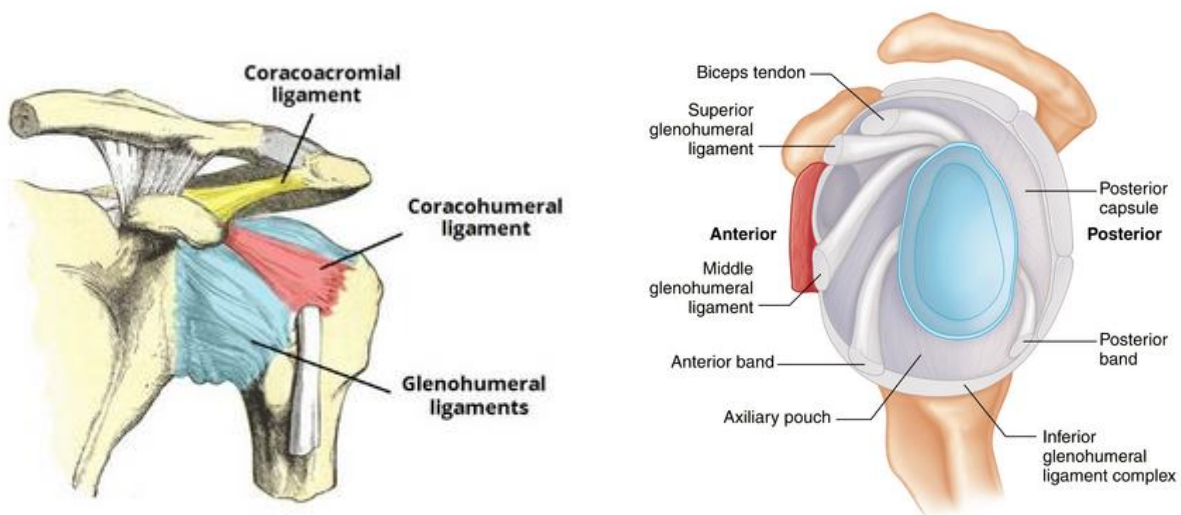
Figure 1:3 Passive stabilizers of the shoulder: left: frontal view and right: sagittal view.

(Left image courtesy of https://teachmeanatomy.info/upper-limb/joints/shoulder) and right image courtesy of https://musculoskeletalkey.com/clinical-anatomy-and-biomechanics-of-the-glenohumeral-joint-including-stabilizers/)

A failure of the rotator cuff muscles can lead to serious consequences: the uncontrolled posterior/anterior translation of the humeral head could lead to shoulder dislocation [3] or in more moderate cases, to a gradual wear of the glenoid cavity as well as the humeral head cartilage, therefore reducing the movement of the GH joint and causing the onset of pain. This reduction, coupled with cartilage damage may lead to problematic shoulder pathologies such as osteoarthritis and osteoporosis [4].

1.2   Glenohumeral Osteoarthritis

Glenohumeral Osteoarthritis (OA) is a degenerative joint disease, which causes the breakdown of articular cartilage and bone. It is different from Rheumatoid Arthritis (RA), which is an inflammatory autoimmune condition [6,7] . People affected by OA suffer from severe pain and eventually reduced mobility and life quality. Several joints might be affected by OA, but the most common ones are knees, hips and fingers. Shoulder OA is not as prevalent but is still very common and increases with age [8]. Two types of OA are identified: "Primary" describes first-time OA without any available pre-existing condition and "secondary" OA may be caused by previous conditions such as chronic instability, humeral fracture, rotator cuff tears, surgery or trauma [8–10] . In Switzerland, 2013 was the first year in which the number of patients hospitalized due to osteo-articular and musculoskeletal pathologies exceeded the number of patients hospitalized because of other injuries [11].

1.3   Total Shoulder Arthroplasty

In most advanced cases of OA, a total shoulder replacement, called Total Shoulder Arthroplasty (TSA) is advised. TSA consists in replacing the damaged cartilage and exposed bone by human-made implants in order to reestablish the basic shoulder function. Surgeons have the choice between two kinds of replacement: treatment using anatomical shoulder prosthesis, called anatomical Total Shoulder Arthroplasty (aTSA) or the newer reverse Total Shoulder Arthroplasty (rTSA). rTSA is preferred when faced with rotator cuff tears [4,12] (Figure 1:4).
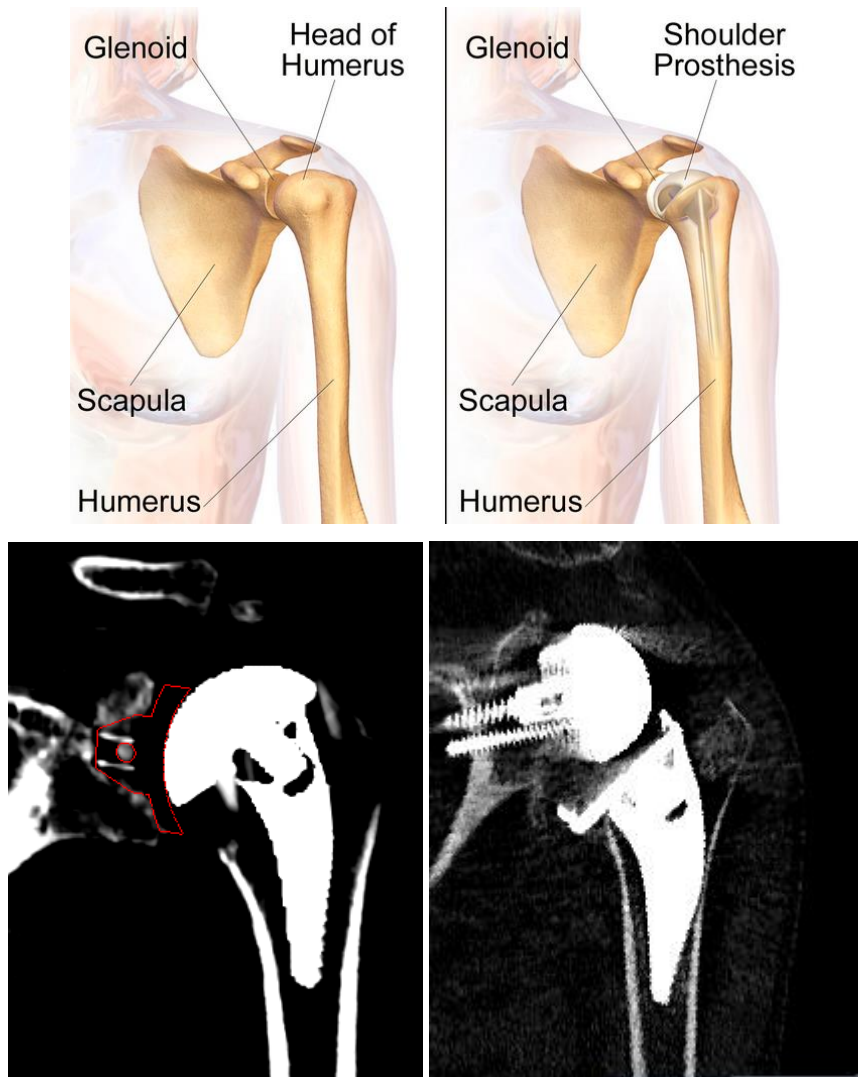
Figure 1:4 Top: Depiction of Total Shoulder Arthroplasty. Bottom: Postoperative computed tomography images of anatomical Total Shoulder Arthroplasty (aTSA, left) versus reverse Total Shoulder Arthroplasty (rTSA, right).

(Top image courtesy of Wikimedia.org. Image under Creative Commons Attribution-Share Alike 4.0 International license. Author Bruce Blaus)

Aiming to improve implant stability and to restore the mobility of the shoulder joint, but at the same time to protect the injured rotator cuff muscles, the implant used in rTSA was first invented in 1985 by Grammont [4,13,14]. The rTSA procedure consists in replacing the glenoid by a spherical implant and adding a cup at the humeral head (Figure 1:4, right). Although rTSA was successful in relieving pain and restoring function in many cases [4], this design had many drawbacks. The main complications associated with rTSA are: implant loosening and failure at the bone-baseplate interface, scapular notch (glenoid bone resorption due to cyclic contact with the humeral component), micromotion or wear of the humeral cup.

The implant used for aTSA mimics the anatomy of the GH joint (Figure 1:4, left) and was first developed by Neer in 1972 [15]. The procedure consists in replacing the humeral head by a metallic sphere and the glenoid

by a polyethylene socket. In this case, the rotations in the joint are still performed mostly by the rotator cuff muscles and thus proved to be inefficient in case of damaged rotator cuff muscles [3]. Although aTSA may also be used in cases of rotator cuff insufficiency [15].

Although aTSA is an established procedure with very positive outcomes in terms of reduction of pain and restoring patient's mobility [15,16], its failure and revision surgery rates are relatively high compared to other joints, such as hip arthroplasty [17]. One of the main causes of aTSA failure is the aseptic loosening of the glenoid component [3,4,15,18–22], but the mechanisms behind this phenomenon are still unclear [19,22,23]. It may be caused by excessive stresses at the bone-implant interface [3], by bone resorption and micromotion, or by component instability due to off-center loadings, the so-called "rocking horse effect" [12,14,15,20].

1.4   Shoulder Instability after aTSA

There are three types of shoulder instability: first the luxation, commonly known as shoulder dislocation, happens when the humeral head pops out of the glenoid cavity without returning to its stable position. Second, subluxation is known as an unstable situation of the native joint where the humeral head "briefly" slides away from the glenoid cavity but returns back inside the glenoid fossa without any treatment. Some persons report that this subluxation might happen during sleep. This subluxation may happen anteriorly, posteriorly and inferiorly [24]. Third, the most commonly used definition though is the GH subluxation expressed by the Glenohumeral Subluxation Index (GHSI). This GH subluxation is defined as the relative position of the humeral head with respect to the glenoid fossa and/or to the scapular axis, measured on the transverse slice of a CT [25,26]. This subluxation is expressed in terms of distance (millimeters) or by the GHSI, defined as the relative position of the humeral head with respect to the glenoid fossa center, normalized by the humeral head diameter and expressed in percentage subluxation [27]. GHSI is measured in 3D as it was proven to be more reliable than the conventional 2D measurements [28,29].

OA causes the erosion of the joint, thus decentering the humeral head with respect to the glenoid fossa center. Historically, OA glenoid types were first categorized by Walch et al. [26]: Type A represents no subluxation, the glenoid is symmetrically eroded. Subcategories include A1 presenting small glenoid erosion and A2 presenting severe glenoid erosion. Type B occurs when there is a posterior subluxation: the wear of the joint occurs asymmetrically. Subcategories include B1: minor posterior erosion and B2: severe posterior erosion. Type C is not associated to osteoarthritic wear, but to dysplasia. Later, a more detailed classification was proposed by Bercik [30] who introduced type B3 as monoconcave and posterior erosion of glenoid inducing a retroversion of at least 15° and/or a 70% subluxation. Moreover, glenoid anteversion and anterior humeral head subluxation was introduced and defined as type D. This study also presented a precision for

A2: this type should present a line, if drawn between anterior and posterior rims of the glenoid, that transects the humeral head.

If the preoperative subluxation is not corrected during aTSA, the eccentric humeral head component may apply an off-center loading postoperatively on the glenoid component which may accelerate its failure (rocking horse effect) [25,31]. As such, patients planned for aTSA and presenting a risk of recurrent postoperative GH subluxation, asymmetrical overcorrected glenoid implants have been suggested as an alternative to classical implants. The potential advantages and drawbacks of these asymmetrical implants have however never been assessed clinically.

Although measurement techniques may exist, investigating shoulder pathologies and their causes is a complicated task because the needed parameters cannot be obtained in a non-invasive manner. For example, the behavior of deep muscles and the measurement of joint reaction forces cannot be acquired in vivo for healthy patients. In order to overcome these experimental limitations, non-invasive experimental set-ups such as motion capture devices were introduced. On the other hand, numerical models are flourishing. Two types of numerical models are distinguished: musculoskeletal models (MSM) and finite element (FE) models [5]. Usually MSM are multi-body systems, based on rigid body dynamics which determine joint reaction force and muscle forces. Their main advantage is their ability to compute a large number of physiological components such as bones and soft tissues as well as their respective interactions. However, by using the rigid body assumption they do not give any information about material deformations or about bone internal quantities such as stress or strain. On the other hand, FE models have the capacity to predict stress, strain, micromotion at the bone-implant interface and more instability factors but are not adapted to simulate the interaction of a large number of anatomical structures such as the effect of all the different independent muscles acting together on the shoulder.

1.5 Musculoskeletal Modeling of Shoulder Joint

The human shoulder is a highly complex joint based on the interplay between bones and muscles. Quantifying this interplay is highly difficult due to the limited available measurement techniques and to general ethical aspects. In this sense, musculoskeletal modeling turned out to be a helpful means to describe and estimate the biomechanical role of each component of the shoulder complex.

A number of musculoskeletal models (MSM) were developed in the last decades aiming to provide a deeper understanding of the shoulder joint in a non-invasive way. The long-term goal of most MSM is to be a clinical tool to improve the diagnosis, pathology, treatment and post-treatment processes [32,33]. However, most of these models either use values obtained from cadaveric measurements based on scaling [32,34] or are based on a small number of subjects [35].

Some of the known and used shoulder models are the Delft shoulder and elbow model [36,37], Garner and Pandy model based on the visible human project [38,39], the Swedish model [40], the AnyBody model [41], the Opensim model [42], the UK National shoulder model [43], the Waterloo model [44], the Case model [45] and the Portuguese model [46]. All these models contain the joints and muscles of the shoulder complex.

Most of the shoulder MSM are based on an inverse dynamics principle, meaning that the joint and muscle forces are obtained from input kinematics of the joints. All these models are based on static or dynamic cost function minimizations, for example the minimization of the squared muscle forces over the physiological cross sectional area (PCSA) [44], the sum of squared errors between predicted and constrained angles [43], the difference between measured electromyography (EMG) and predicted muscle activity [47], the muscle-energy consumption during complete motion [46], a stability function to avoid luxation [48].The kinematics input into the models were obtained either from motion recordings available in the literature or were specifically measured for the study using 3D motion capture systems. The latter method is very useful as it provides more accurate movements of the joints and bone segments compared with literature-based data but the soft tissue artefacts remain an important source of uncertainties, especially for the scapula [33].

As validation techniques, comparison against available literature data (on joint reaction force amplitude, GH center location or muscle forces), against EMG signal measurements or instrumented prostheses [49] were mostly used [32,33]. Moreover, the provided data from instrumented prostheses is more and more established as a good validation method. Recent review papers argued however, that these validation methods are limited since surface EMG cannot measure deep muscles and are subject to skin movement artefacts and instrumented prostheses do not provide indication on healthy subjects [33].

The emerging tendency in MSM of the last decade is to take account of the subject-specific data [32,33,50], the final goal being to create a MSM in a clinical setting that can be adapted quickly to each new patient and thus provide a custom-made diagnosis and treatment approach. The most common and simple approach for patient-specific modeling is to scale the whole model with patient height and bodyweight. Recently, specific parameters were adjusted, such as muscle properties based on imaging [50] or kinematic data [32].

Recent publications [32,50] highlighted the lack of sensitivity analysis and its utmost importance to validate the models. This lack of validation is due to many factors: the huge amount of parameters present in the model steps, the challenge of choosing the correct behavior model for the study, the correct parameters to study and their range; and finally the expensive computational time.

The sensitivity of MSM to predict GH joint reaction force was reported to be largely determined by GH joint center location, input kinematics, Physiological Cross Sectional Area (PCSA) of muscles, scapular shape, scaling of muscle insertions and origin locations or segment length [32,33]. These studies used either parametric approaches, comparisons to experimental data or probabilistic approaches [32,33].

1.6 Finite Element Modeling of Total Shoulder Arthroplasty

Finite Element (FE) models have proved their potential in the analysis and prediction of the mechanisms around total joint arthroplasty and have been used for the past 40 years [51]. Many FE models simulating shoulder arthroplasty exist and are getting more and more sophisticated, with a clear tendency towards patient-specific modeling. However due to the complexity of the musculoskeletal system of the shoulder and the difficulty to get accurate measurements, simplifications and assumptions need to be made on several levels: 2D models, ideal boundary conditions, joint force taken from literature, soft tissues not taken into account, isotropic, elastic, homogenous bone material properties, ideal or approximate friction coefficients, no subluxation or absence of humeral head translations [12,52–58].

FE models were developed to investigate different clinical questions and pathologies such as rotator cuff tears, GH joint instability or effect of different implant designs on outcome of shoulder arthroplasty [5]. In the context of TSA, most FE models investigated different implant material, designs and orientations [54,59–63], use of cement [64,65] or articular conformity [53,66,67] with respect to glenoid component aseptic loosening [5].

Three important steps are needed for the construction of a FE model: first the geometry of the bone or soft tissue is collected either by using cadaveric data, literature data, average measured data or subject-specific data acquired thanks to imaging techniques such as Computed Tomography (CT), Micro Computed Tomography (μCT) and Magnetic Resonance Imaging (MRI) [5,68]. The second milestone is to apply mechanical properties. The scapula is usually modelled as rigid or linear elastic material. Recently, density-Young's Modulus (ρ-E) relationships, with density (apparent, bone mineral or ash) derived from CT data were applied on the scapula [5,65,69–72]. The third milestone consists in assigning boundary conditions on the FE model: some studies used boundary conditions from the experimental set-up they designed while others imposed artificial boundary conditions [5]. Recently, muscle forces from MSM were used in order to make the loading situation more realistic [5,68].

Although FE models are very useful non-invasive tools that predict general bone biomechanical behavior of the shoulder joint [19,71,73,74], they have three most common limitations: First, the lack of patient-specific parameters such as exact patient geometry or in-vivo loading [5]. The second limitation is the lack of a real-

istic constitutive material law to describe the mechanical behavior of the glenoid bone [5,75,76]. Bone constitutive material law was reported to have a direct impact on the validation potential of FE models [69,76]. The third major limitation of FE modeling is the lack of experimental validation [5,69,73,74]. Especially, in the context of aTSA, FE models are helpful to identify the causes of glenoid implant loosening which was reported as the most common sort of implant failure [19,21–23]. In this light, three studies recently attempted at validating their FE models by comparing displacement measurements on scapula [73], strain measurements on humeral head [77] and strain measurements on scapula [77] from the non-invasive measurement technique Digital Volume Correlation with specimen-specific FE model-predicted displacement and strain. Boundary conditions from the experiment were applied. For these studies, good agreement was found between measurements and FE model-predicted quantities when the boundary conditions of the experiment were replicated: slope ranged between 0.87 and 1.09 and coefficient of determination R^2 between 0.79 and 1.00 for glenoid bone displacement [73]; slope = 0.83 and R^2 = 0.80 for humeral head strain [77] and slope = 0.54 − 0.59 and R^2 = 0.73 − 0.75 for scapula compressive strain [78].

1.7 Digital Volume Correlation

A few different in vitro measurements have been proposed to analyze the glenoid bone-implant mechanical system. Experimental setups approved by the American Society for Testing and Materials (ASTM) were developed to track the bone-implant relative movement with the help of differential variable reluctance transducers (DVRT) [21,79]. However, these methods affect the bone structure and are limited to a small set of discreet measurement points. Thus, they do not fully describe the bone-implant behavior. To overcome this limitation, a method combining micro-CT (µCT) and digital volume correlation (DVC) was proposed [69].

DVC is a measurement technique first introduced in 1999 by Bay et al [80] to track pattern of microstructural features in a volume of interest (VOI). DVC is based on a non-rigid registration obtained by optimizing an objective function that compares samples from unloaded and loaded images [81,82]. DVC needs high resolution images such as µCT images and is thus able to provide full-field displacement and strain maps in a VOI.

The emerging DVC combined to µCT technique was used extensively in the hip arthroplasty and vertebroplasty [19,82–91]. More specifically to the shoulder joint, DVC - µCT technique was used to track micromotion around cementless porcine glenoid implants [69] with errors ranging between 20 and 30 µm. Moreover, DVC was used to investigate displacements around cadaveric scapulae due to axial loading [73]. Most recently, DVC was used to measure strain on humeral head [77], and on glenoid under loading [74]. The latter study reported strain measurements of cemented glenoid bone under concentric, anterior and posterior loading (750 N). Medio-lateral bone strain was measured using DVC before and after implantation. Comparing deformation at a virtual section at 5.7 mm away from glenoid face, the authors found that the implanted glenoid

was more deformed than the native glenoid and that anteriorly and posteriorly loaded specimens achieved higher range of strain than the concentric loaded specimen [74].

Only very recently, have there been attempts at creating and validating FE models against DVC measurements: Kusins et al. [73] quantified the accuracy of Quantitative Computer Tomography (QCT)-derived FE models of four cadaveric scapulae in replicating the displacements measured by DVC. The specimens were loaded mechanically and the displacement captured via μCT. The authors found a very good correlation (co-efficient of determination $R^2 = 0.79 - 1.99$ and slope = 0.87 − 1.09) between experimentally measured displacements and specimen-specific FE model-predicted displacements. This was true only when the experimental displacements were used as boundary conditions to the FE model. Another study [76] investigated displacement and reaction force predictions of FE models using 15 different material mapping density-elasticity laws. The authors also found an excellent experiment-FE model agreement when boundary conditions of the experiment (experiment displacements) were used. Lastly, only two studies quantified compressive strains predicted by specimen-specific model of osteoarthritic humeral head [77] resp. of scapula [78] compared to measured strain by DVC. The authors found an excellent agreement ($R^2 = 0.80$ and slope = 0.83) [77] resp. good agreement ($R^2 = 0.73 - 0.75$ and slope = 0.54 − 0.59) [78] when boundary conditions of the experiment were applied in the model.

An important aspect in DVC is the error and uncertainty quantifications. Most reported uncertainty studies evaluated uncertainties either by a zero-strain analysis (two consecutive unloaded scans) [84,86,88,89,92–94], or by virtually deforming an image set [92,95]. More recently, different DVC parameters were compared on the same image sets [92,93]. It was reported that accuracy and precision of displacement and strain outputs are influenced by a number of factors such as DVC objective function [82] or image resolution [82,92,93]. Most recently, one study [96] published error analysis involving repeated virtually deformed images: the authors found the highest errors in the direction of the applied virtual loading and further argued that this conservative method should be used to assess errors associated with measurement technique.

1.8   Sensitivity Analysis

The development of patient-specific (PS) models is the trend of the last decade [32]. Recent MSM reviews highlighted the lack of sensitivity analysis and their utmost importance to validate the models because of the important amount of parameters present in the model steps, the challenge of choosing the correct behavior model for the study, the correct range for input parameters, the correct parameters to study and finally the expensive computational time.

In general, the use of modeling comes with a goal of proving the usefulness of the model at hand and its ability to correctly predict the system it represents. In this area, often the concepts of verification, validation

and sensitivity analysis are not easily distinguishable. Based on The American Society of Mechanical Engineers (ASME), the verification is the "process of determining that a computational model accurately represents the underlying mathematical model and its solution" [97], in other words "are the equations solved correctly?"; whereas the validation is the "process of determining the degree to which a model is an accurate representation of the real world from the perspective of the intended uses of the model" [97], in other words, "does the model correctly predict the system it represents?".

The Sensitivity Analysis (SA) is a method to assess the variation in the output of a model after varying its inputs. If a slight change in the inputs causes dramatic changes in the output of the model, the latter is not robust enough and thus cannot be used widely. The main aim of a SA is to provide a quantitative confidence level of a model by first assessing the uncertainties or errors associated with the different input sources of that model, with the implementation of that model, with the propagation of input uncertainty through the model and finally with the correctness of the output [98–100].

SA can answer the following questions: Does the model I built resemble my system? What are the most contributing factors in my study? Are there groups of factors that interact with each other? Where is my output variation most visible and significant? Answering these questions helps first to assess the most significant sources of errors in the model, second to provide a ranking of the most influential factors in a model and third to find a direction for the bettering of the model [100].

Numerous methods exist to perform SA, but three approaches are mainly used in numerical biomechanical studies: the simple parametric study, the probabilistic approach and the design of experiment method. We will review these three important approaches briefly with focus on their usability, their advantages and disadvantages [98–100]. A parametric study consists in varying one input at a time and studying the consequent output changes. It is a fast and humanly understandable method however; it provides information only about one factor. The probabilistic approach is used for random and continuous input variables. The input is given as a normal distribution and the analysis is performed by repeating the analysis for randomized input values. This method provides the contribution of each of the inputs to the uncertainty of the model output. The probabilistic approach, although considered the gold standard, is usually too time consuming for numerical simulations. The Design Of Experiment (DOE) method is quite new in the biomechanics modeling world but is more and more used. It consists in varying all inputs at the same time. The result is a hierarchy of importance of the factors as well as the interaction of these input factors on the model output. This method has many different approaches (e.g. Factorial design, Taguchi) and thus may be more or less time consuming depending on the chosen method and the simplifications made. The most important drawback of this method is the so called "lack-of-random error". The method is indeed restricted to look for a solution around the discrete input numbers given while the correct value may lie outside this spectrum. Moreover, varying more

than three different parameters at the same time is quite challenging to human understanding, if compared to the simple parametric study. The method ends with an analysis of variance to get a statistical significance of the ranked factors. Its main strength is the relative ranking of the most influential parameters in a model [99–101].

Most of the recently published FE studies still use a simple parametric study but there is an increasing tendency to use DOE methods to investigate the sensitivity of models in knee, hip, shoulder and back biomechanics [101–107]. The main driving force of the above-mentioned publications is ranking the most influential parameters in their multi-step / multi-factor model for the first time in their respective fields. With this method, they were able to gain more in-depth knowledge of the important factors in numerical modeling as well as directions of bettering the modeling process.

Past studies of MSM investigating sensitivities of shoulder joint reaction forces determined an important influence of joint center location, input kinematics, PCSA of muscles, scapular shape and scaling of muscle wrapping, segment length and muscle insertions. All these studies used either parametric approaches, comparisons to experimental data or probabilistic approaches [32,33].

1.9 Limitations of Current State of the Art

In light of the state of the art presented, four main limitations were identified and addressed in the present work.

First, for patients planned with aTSA and presenting a risk of recurrent postoperative GH subluxation, asymmetrical overcorrected (OC) glenoid implants were suggested as an alternative to classical implants, however, the underlying mechanisms behind shoulder recurrent instability after aTSA are still unknown and the biomechanical advantages of OC implants has not been assessed clinically nor biomechanically.

Second, although shoulder FE modeling in the context of aTSA has been an established procedure for the last four decades, the correct representation of boundary conditions and experimental validation remain challenging.

Third, although the use of PS models for aTSA has been rising during the last decade, both FE modeling and in MSM, numerous questions remain unsolved: which parameters to change from one patient to another? Which of those are relevant to the model? How to extract the patient's data?

Last, even if optimal PS parameters were found, a huge gap in the sensitivity analysis of these (FE and musculoskeletal) models of shoulder arthroplasty would remain. Although probabilistic approaches are considered as the gold standard, both the FE models and the MSM still mostly use one-at-a-time SA strategies. The

latter is a good-enough local strategy to one's own model, but does not give an importance-ranking of the input parameters. A ranking of importance is preferable especially in light of the large number of parameters that may be considered in a PS model.

1.10   Thesis objectives

The aim of the present work was to evaluate the potential biomechanical advantages of overcorrected (OC) implants in the context of aTSA by answering the two following research questions: 1) Do OC implants reduce postoperative subluxation? 2) Do OC implants transfer excessive stresses to the cement at the bone–implant interface? Four objectives were considered to answer these questions. An overview is provided in Figure 1:5.

The first objective of the thesis, presented in Chapter 2, was to measure full-field displacement and deformation of the glenoid bone under axial loading. Digital Volume Correlation technique was applied to cadaveric human glenoid bones imaged with µCT while undergoing various mechanical loadings.

The second objective of this thesis, presented in Chapter 3, was to create and validate FE models of three cadaveric glenoids under axial loading, using the experimental set-up developed in the previous Chapter.

The third objective of the thesis, presented in Chapter 4, was to extend a generic MSM of the shoulder to include the forearm and to become a patient-specific model. The updated model would then be used to predict GH joint reaction forces during three activities of daily living. This part was performed in collaboration with two other PhD projects.

The final objective of this thesis, presented in Chapter 5, was divided in four steps: first the workflow of the validated specimen-specific FE model of Chapter 3 was used to create patient-specific FE models. Second, the MSM developed in Chapter 4 was used to predict shoulder joint reaction forces of patients recruited for the study. These joint reaction forces were put as boundary conditions in the FE models. Third, OC implants were designed and imported into the FE models. Last, subluxation, cement stress and bone compressive strains predicted by FE models were compared between both implant designs (standard and OC) to answer the research questions.
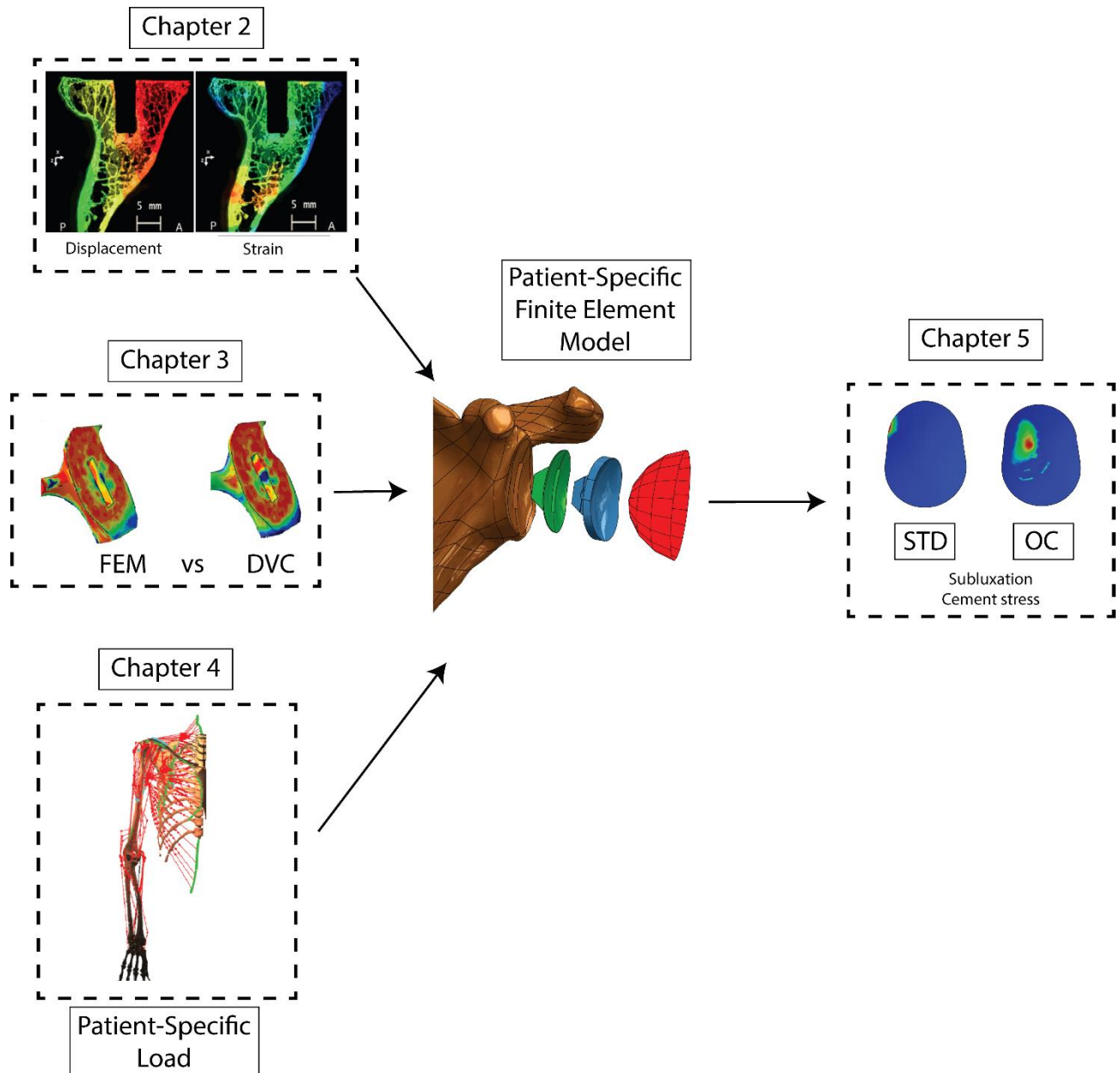
Figure 1:5 Overview thesis objectives.

Chapter 2   Glenoid bone strain after anatomical total shoulder arthroplasty: In vitro measurements with micro-CT and digital volume correlation
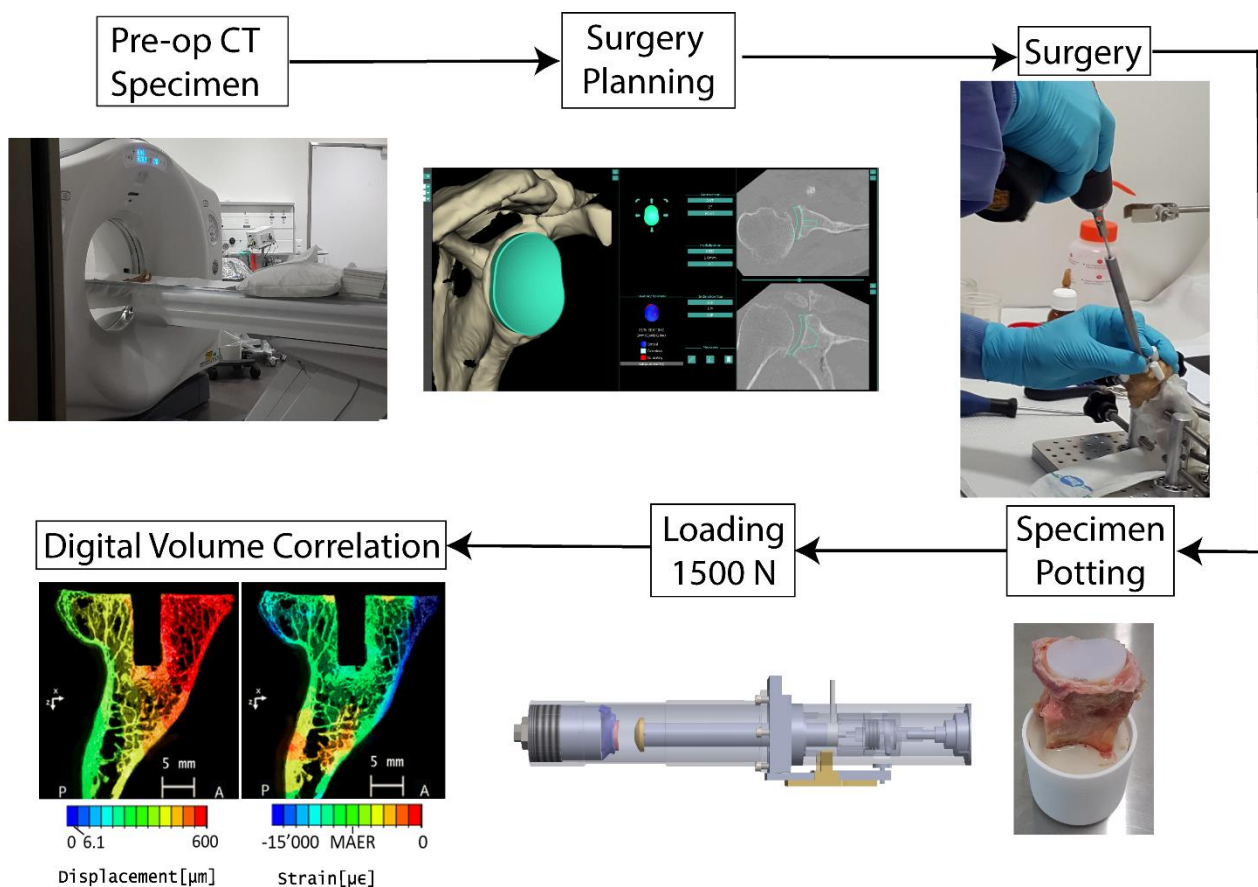
2.1   Abstract

Glenoid implant loosening remains a major source of failure and concern after anatomical total shoulder arthroplasty (aTSA). It is assumed to be associated with eccentric loading and excessive bone strain, but direct measurement of bone strain after aTSA is not available yet. Therefore, our objective was to develop an in vitro technique for measuring bone strain around a loaded glenoid implant. A custom loading device (1500 N) was designed to fit within a micro-CT scanner, to use digital volume correlation for measuring displacement and calculating strain. Errors were evaluated with three pairs of unloaded scans. The average displacement random error of three pairs of unloaded scans was 6.1 μm. Corresponding systematic and random errors of strain components were less than 806.0 με and 2039.9 με, respectively. The average strain accuracy (MAER) and precision (SDER) were 694.3 με and 440.3 με, respectively. The loaded minimum principal strain (8738.9 με) was 12.6 times higher than the MAER (694.3 με) on average, and was above the MAER for most of the glenoid bone volume (98.1%). Therefore, this technique proves to be accurate and precise enough to eventually compare glenoid implant designs and fixation techniques, or to validate numerical models.

2.2   Introduction

Although anatomical total shoulder arthroplasty (aTSA) is an effective surgical treatment for advanced gleno-humeral osteoarthritis, aseptic loosening of the glenoid implant remains a major cause of failure and concern [19,21–23]. While various causes have been identified [19], there are still several open questions, as for example on the optimal glenoid implant design. To answer such questions, in vitro studies are frequently performed.

A few different in vitro measurements have been proposed to analyze the glenoid bone-implant mechanical system. Experimental setups approved by the American Society for Testing and Materials (ASTM) were developed to track the bone-implant relative movement with the help of differential variable reluctance transducers (DVRT)[21,79]. However, these methods affect the bone structure and are limited to a small set of discreet measurement points. Thus, they do not fully describe the bone-implant behavior. To overcome this limitation, a method combining micro-CT and digital volume correlation (DVC) was proposed to measure micromotion around cementless porcine glenoid implants after aTSA [69]. DVC has already been used to evaluate strain in trabecular bone [82,84,86,89], cortical bone [83,84], whole bones [87,88,91] after hip arthroplasty and vertrebroplasty, and recently on in situ mice tibiae [87]. DVC was applied to investigate displacements around cadaveric scapulae due to axial loading [73]and very recently in the context of cemented polyethylene glenoid implants [74]. This study reported strain measurements of glenoid bone under concentric, anterior and posterior loading (750 N). Medio-lateral bone strain was measured using DVC before and after implantation. Comparing deformation at a virtual section at 5.7 mm away from glenoid face, the authors found that the implanted glenoid was more deformed than the native glenoid and that anteriorly and posteriorly loaded specimens achieved higher range of strain than the concentric loaded specimen.

Furthermore, in order to correctly interpret DVC measurements, uncertainties must be evaluated. Most previous studies evaluated uncertainties either by a zero-strain (two consecutive unloaded scan) [84,86,88,89,92–94], or by virtually deforming an image set [92,95]. More recently, different DVC parameters were compared on the same image sets [92,93]. These studies showed that precision and accuracy depend on the spatial resolution of images and on DVC settings.

Therefore, the objective of the present study was to develop a technique based on micro-CT and DVC to measure in vitro glenoid bone strain after aTSA. More specifically, a custom loading device was designed to replicate physiological loading after aTSA, optimal parameters of the measurement technique were evaluated, and errors associated with the measurement of displacement and strain were quantified.

2.3 Materials and Methods

2.3.1 Specimen preparation

A fresh cadaveric scapula (harvested from a 69-year-old female) was obtained from Science Care (Phoenix, AZ, USA), wrapped into saline-moistened gauze (10% phosphate-buffered saline) and vacuum sealed to be stored at -80°C. Preoperative planning was performed using standard-of-care conventional shoulder computed tomography (CT) scans (Discovery CT750 HD, GE Healthcare, Waukesha, WI, USA). Data acquisition settings were: 120 kVp tube potential; 200 mA tube current; 0.7 s gantry revolution time; 64 x 0.625 mm beam collimation; 0.984 pitch. Image reconstruction parameters were: 1.25/0.7 mm section thickness/interval, 488 x 488 μm in-plane spatial resolution; sharp (bone plus) kernel. An anthropomorphic thorax phantom (QRM, Moehrendorf, Germany) with a synthetic humerus (Sawbones, Vashon Island, WA, USA) and saline plastic bags simulating rotator cuff muscles were used to replicate in vivo x-ray attenuation in the experimental setup. The scapula was thawed in saline at room temperature for 24 hours prior to CT scanning and refrozen (-80°C) immediately after.

A senior shoulder surgeon (AF) performed the surgical planning from this CT dataset by using a preoperative planning software (BLUEPRINT™ 3D Planning, Tornier-Wright Medical, Montbonnot-Saint-Martin, France). This planning helped selecting the optimal glenoid implant type, size (AEQUALIS™ PERFORM keeled size S, Tornier-Wright Medical, Montbonnot-Saint-Martin, France) and positioning within the glenoid bone. To avoid beam hardening metal artifacts, the two original metallic radiopaque markers were removed from the keel of the glenoid implant by the manufacturer.

The scapula was thawed in saline at room temperature 24 hours prior to implantation. The implant was cemented (TBCem 3, Class IIb, European Medical Contract Manufacturing, Nijmegen, The Netherlands) within the glenoid bone using patient-specific instruments. The scapula was then vacuum-sealed in saline-moistened gauze and then refrozen (-80°C).

The implanted scapula was thawed in saline at room temperature 24 hours prior to mechanical testing. The implanted scapula needed to fit into an aluminum tube with a diameter of 60 mm, thus requiring cutting. A diamond band saw (312 Pathology Saw, EXAKT Technologies, Oklahoma City, OK, USA) was used to remove the acromion, spine, coracoid process, inferior pillar (23 mm from the center of the glenoid cavity), and medial part (70 mm from the center of the glenoid cavity) of the scapula. The soft tissues were kept in order to preserve the natural moisture of the specimen as much as possible (Figure 2:1). To center the glenoid within the tube and align the medio-lateral scapular axis with the tube axis, we used a custom 3D printed guide. The specimen was then potted 30 mm deep in polyurethan resin (NEUKADUR MultiCast 20, Altropol Kunstoff, Stockelsdorf, Germany).
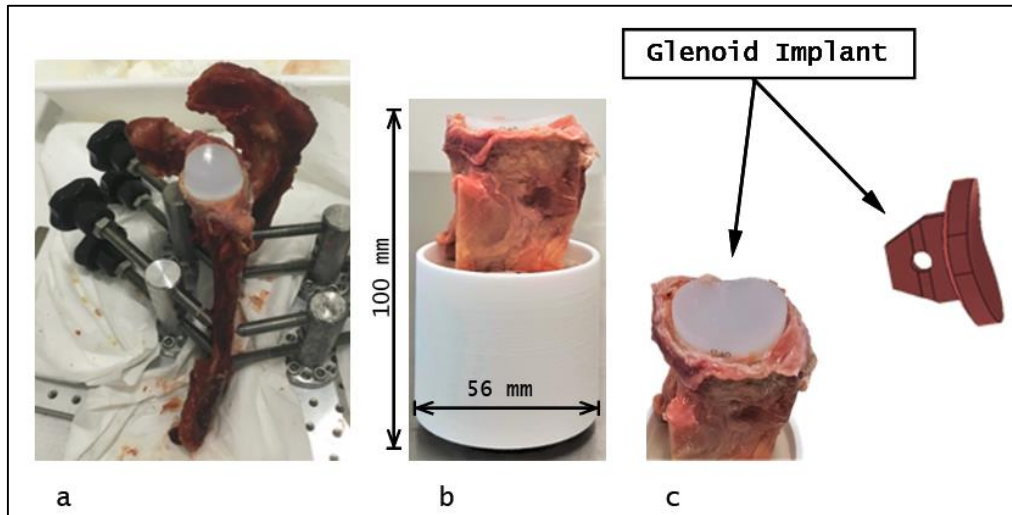
Figure 2:1 a) Implanted specimen in implantation setup. b) Potted specimen in polyurethan resin. c) image and CAD image of implant.

2.3.2   Loading device and micro-CT imaging

A micro-CT loading device was adapted to reproduce a force of 1500 N applied by the humeral component on the glenoid implant [108–110]. To avoid beam hardening metal artifacts, we built a spherical cap of polyether ether ketone (PEEK) to replicate the head of the humeral component. This part was mounted on an aluminum piston, aligned with the tube axis. A 2000 N load cell (LCM202-2KN, Omega Engineering, Stamford, CT, USA) and a NI-USB-9215 acquisition card (National Instruments, Austin, TX, USA) were used to monitor the compressive force.

The loading device (Figure 2:2) containing the specimen was inserted into a micro-CT scanner (Skyscan 1076 in vivo micro-CT, Bruker micro-CT, Kontich, Belgium). We first scanned the unloaded glenoid six times subsequently (mCTi, i = 1, …, 6), for error estimation, also known as zero-strain analysis. The scans were performed consecutively pairwise: mCT1-mCT2, mCT3-mCT4, and mCT5-mCT6. After each scan pair, the specimen was removed from the micro-CT and repositioned. The same scanning position was imperatively kept between two consecutive scans. For strain estimation, the glenoid was scanned first in the unloaded state (mCT7), then in the loaded state at 1500 N (mCT8) after preconditioning (10 cycles at 1500 N) and relaxation delay (10 minutes). Scanning parameters were as follows: 36 µm spatial resolution, 100 kV tube potential, 100 µA tube current, 1 mm aluminum filter, 310 ms exposure time, 0.5° rotation step, 360° scanning, 68 mm scanning width and frame averaging 4. The entire glenoid required three sub-scans (3x21 mm = 63 mm total longitudinal coverage), for 130 minutes overall acquisition time. Images were reconstructed using a ring artifact reduction of level 2 and beam hardening correction of 80% (NRecon v1.6.10.4, Bruker micro-CT, Kontich, Belgium).
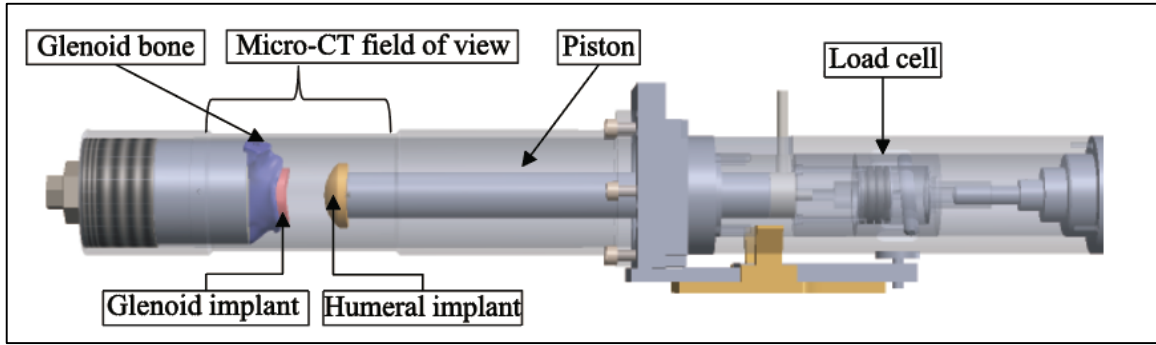
Figure 2:2 Custom-designed loading device fitting into the micro-CT scanner.

2.3.3 Digital volume correlation

DVC was used to estimate 3D displacement maps between each micro-CT scan pair. In each pair, one scan was superimposed to the other by the built-in Euclidean rigid registration of the fixed side (5-mm-thick resin-immersed bone) using Amira 6.7 (FEI SAS, Burlington, MA, USA). All scans were then cropped to include the glenoid bone, but exclude the resin (> 20 mm from the glenoid implant keel) and PEEK sides. A mask was applied on each scan to remove the implant and the soft tissues around the bone and cement. This procedure was performed in Amira. For DVC, Elastix-Transformix open-source registration software [111] was used: Displacement maps were obtained from non-rigid registration with multi-resolution B-spline transform and gradient-descent optimization of normalized correlation coefficient similarity metric. Strain maps were derived from displacement maps using Abaqus finite element solver (v.6.14, Simulia, Dassault Systèmes, Providence, RI, USA).

2.3.4 Parametric study

To find optimal DVC parameters, a parametric study of 53 different settings was performed. The parameters considered were: grid size, number of resolutions[1], sample size, similarity metric, number of histogram bins and the optimization routine. This optimization was performed on three sets of scan pairs: Set1, Set2, and Set3. Set1 contained two same scans (mCT3-mCT3). Set2 contained an unloaded scan (mCT3) and the same scan virtually deformed (mCT3s) with a stretch of 0.5% in the three orthogonal directions. Set3 consisted of two repeated unloaded scans (mCT3 and mCT4). From Set1, we rejected all settings producing non-zero displacement. From Set2, we rejected all settings not predicting the controlled stretch. The check was performed visually and quantitatively by computing the median of the resulting strain in the three orthogonal directions (E11, E22, and E33). We kept only settings visually reproducing the applied stretch and with an error below 150 με. This limit was set for convenience in order to limit the number of settings to 3. It is

---

[1] "Resolutions" is a term used by the software developers to designate "iterations"

important to mention that although some settings produced the lowest errors, they were not kept if they did not reproduce the applied deformation. From Set3, we chose the settings that produced the lowest random errors for the three displacement components (U1, U2, and U3). The direction of U3 is along the scanning and loading axis, and the other two are orthogonal, approximately corresponding to antero-posterior and infero-superior axes. Details are provided in Section 2.6.1.

2.3.5 Error analysis

The errors associated with this measurement technique (optimal DVC parameter set for loaded displacement and strain described above) were evaluated by a zero-strain analysis on the three unloaded micro-CT scan pairs (mCT1-mCT2, mCT3-mCT4, and mCT5-mCT6). Strains were derived from displacement maps on a 2 mm-sized hexahedral mesh of the entire scan. Several errors were evaluated for each of the three scan pairs: We calculated the displacement random errors defined by the standard deviation of the measured displacement. We calculated for each of the six components of strain the systematic and random errors defined respectively by the mean and standard deviation of strain values [93]. Systematic and random errors of the principal strain invariants were calculated. Finally, in order to be consistent with previous studies on DVC, for each scan pair, we evaluated the accuracy and precision defined by the mean absolute error (MAER) and standard deviation of absolute error (SDER) of strain, respectively [81,89,93]. An overview of the error analysis described above is presented in Section 2.6 at Figure 2:6.

For sake of comparison with other studies, the above-mentioned errors were evaluated in a volume of interest (VOI). The VOI (125x226x190 voxels) was located on the anterior part of the glenoid (Figure 2:3).

An additional error calculation was performed between two repeated unloaded and masked scans (mCT3 and mCT4): the first scan remained undeformed (mCT3) and a virtual compression of 1% was applied on the second scan (mCT4def). The virtual compression was applied along X, Y and Z axis, separately. This error analysis was based on a recent study on bovine cortical bone [96] and is presented in section 2.6.4.

2.3.6 Loaded displacements and strains

Displacements of the loaded scapula were calculated with the optimal DVC parameter set (Appendix A) using unloaded (mCT7) and loaded (mCT8) scans. Strains were derived from displacements on a tetrahedral mesh (2 mm size) of the glenoid bone, which was segmented with Amira. We report the amplitude of displacement and the minimum principal strain stain invariant. All other displacement and strain components are provided in Section 2.6.2.

2.4 Results

2.4.1 Parametric analysis

The parametric analysis provided the following optimal parameter set: five-resolution B-spline transform (40-voxel grid size) and gradient-descent optimization (gain factor 100 and 32 histogram bins) of normalized correlation coefficient similarity metric using a sample size of 12'000. Extended data can be found in Section 2.6.1.

2.4.2 Error analysis

The random error of displacement in all three directions ranged between 2.9 and 11.7 μm. The average random error in loading direction was 6.1 μm and peaked at 9.0 μm (Figure 2:3).

The systematic error of the six components of strain ranged between -172.7 με and 806.0 με, while random error ranged between 395.3 με and 2039.9 με. The systematic error of principal strain invariants ranged between -1367.2 με and 1348.7 με, while random error of principal strain invariants ranged between 280.6 με and 1656.3 με. On average, systematic and random errors of the third principal strain invariant were -1129.4 με and 1274.7 με, respectively.

Over the three zero-strain analysis, the accuracy of the method (MAER) ranged between 484.2 με and 800.2 με while the precision (SDER) ranged between 313.2 με and 579.8 με. On average, accuracy (MAER) was 694.3 με, while precision (SDER) was 440.3 με.

Within the VOI, the random errors of displacement ranged between 1.62 μm and 2.17 μm. The systematic error of the six components of strain ranged between -321.7 με and 637.9 με, while random error ranged between 410.1 με and 964.9 με. The systematic error of the third principal strain invariant was -681.7 με while its random error was 539.4 με. MAER was 626.0 με and SDER was 195.7 με.
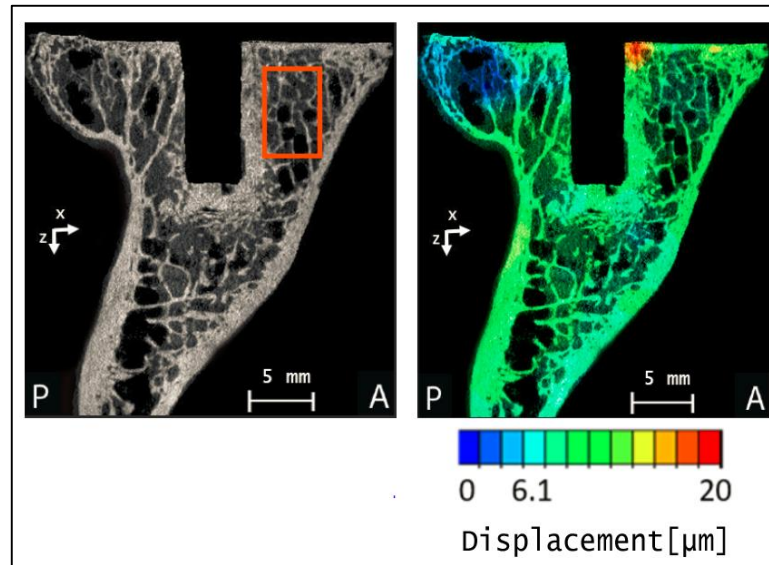
Figure 2:3 Left: Unloaded masked specimen with VOI in orange.

Right: Random error of displacement in loading direction (U3).

2.4.3 Loaded displacement and strain

Maximum displacement amplitude was 825.4 µm (Suppl. Material Table 2:4). Displacement in the axial (loading) direction was up to 797.6 µm (Figure 2:4, left), while maximum displacement in the transverse direction was 825.4 µm. The axial displacement was greater on the anterior than posterior side, revealing a bending deformation. The bone volume fraction of axial displacement above the average random error of 6.1 µm was 99.6%.

Minimum principal strain was more negative (compressive) on the anterior than posterior side (Figure 2:4, right). Average and peak compressive strain (absolute minimum principal strain) were 8738.9. µε and 46'000.0 µε, respectively. The bone volume fraction of minimum principal strain above accuracy (MAER) was 98.1% (Figure 2:5). The minimum principal strain percentile values 5%, 25%, 50%, 75%, 95% were respectively: -22400, -11160, -6540, -3770, -1210 µε. Extended data can be found in Section 2.6.2.
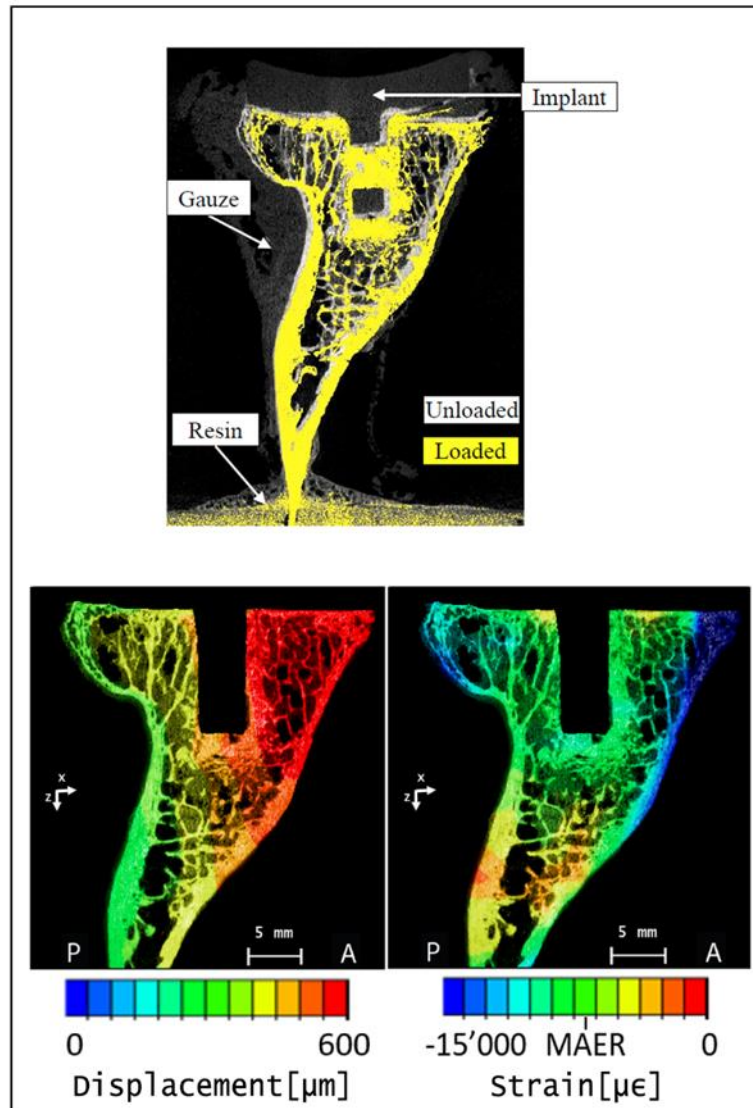
Figure 2:4 Top: Loaded unmasked image of specimen (yellow) superposed on unloaded unmasked image of specimen (grey). Bottom: Displacement along loading axis (U3) (left) and minimum principal strain (right) resulting from a 1500 N force applied in the z-direction.
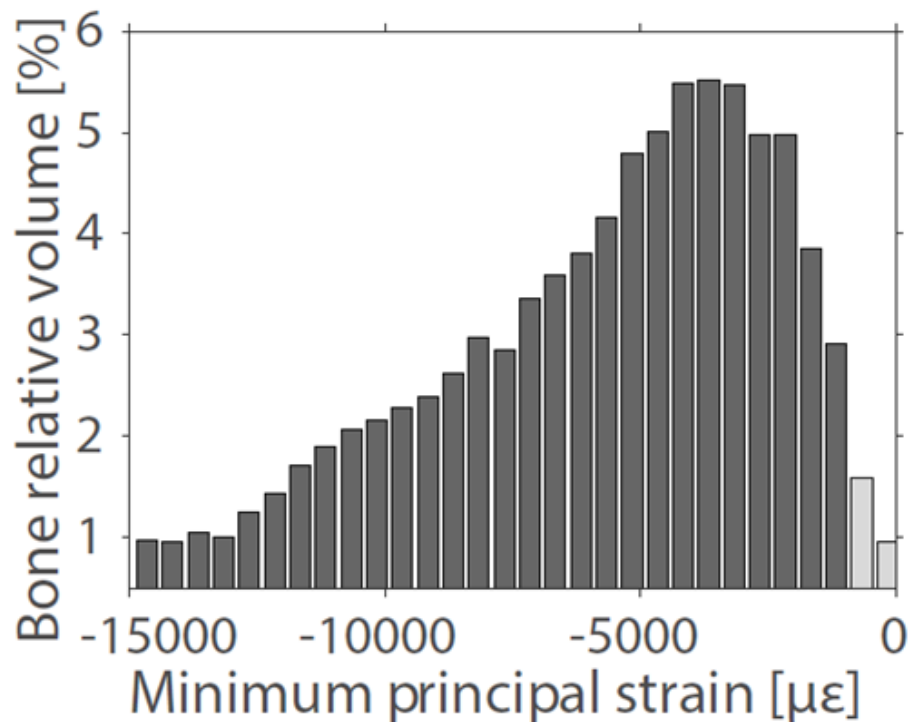
Figure 2:5 Volumetric distribution of minimum principal strain within the loaded glenoid bone, where the light grey bars represent the accuracy (MAER).

2.5   Discussion

Although total shoulder arthroplasty is an effective procedure to relieve pain and restore range of motion, its failure rate is higher than hip arthroplasty [17,112]. Component loosening was identified as a possible cause of failure. Loosening may be due to excessive bone deformation. The aim of this study was to develop a method to measure strain within the glenoid bone after aTSA, while a load was applied to the glenoid implant by its humeral counterpart. Micro-CT images and DVC were combined to evaluate glenoid bone strain with sufficient accuracy and precision for future numerical bone model validation studies; which in turn might help predict bone behavior and diagnose shoulder problems in a clinical environment.

The peak random error of displacement in the loading direction corresponded to 1.1% of the maximum loaded displacement (797.6 μm). The random error was evenly distributed over the glenoid bone with the exception of localized peaks found at the edges. Away from the edges, on the VOI, this error decreased to 2.2 μm. The random errors of displacement were in the same range as other DVC studies using similar scanning spatial resolutions: from 0.5 to 63.1 μm random errors [93].

The systematic and random errors of strain were consistent with other similar cemented bone measurements at 16-voxel size, but higher for 48-voxel size [93]. The highest errors were localized at the edges of the image. A variability in error values was observed between the three zero-strain tests due to the unavoidable repositioning, as reported by a recent study which found higher errors after repositioning (mean strain differences up to -4427 με). It would have been interesting to report zero-strain errors using two consecutive scans without repositioning but it was not possible due to the size of the specimen which required three subscans. The specimen holder movement between repeated scans was thus unavoidable.

The reported MAER (626.0 με) and SDER (195.7 με) values on the VOI were within the range of a previous study on cemented specimens (VOI-3 and VOI-5 of [93]) but higher than a recent in situ study on loaded mouse tibiae that reported MAER and SDER around 158 for an equivalent subvolume [87].The MAER represented 7.2% of the average compressive strains in bone. According to [89], the MAER is below the recommended 10%, thus ensuring the usability of our method for future numerical model validation.

Previous studies on vertebrae, femur and tibia found compressive yield strain to range between 7'000 – 10'000 με [113,114]. If we assume the glenoid bone to yield around 10'000 με, 72.3% of our glenoid sample was in the elastic range under 1500 N of compressive axial loading. Although the peak compressive strain value of 46'000 exceeds bone failure strain, it concerned only 0.1% of the bone and was thus considered an outlier. When outliers are not considered, the compressive strains peak at -22'400 με. Our loading device induced a complex bone deformation. In the middle axial slice, it appears mainly as a bending strain. This bending was caused by the eccentric (relative to loading axis) fixation of the medial part of the scapula in the

cement but especially by the natural curved form of the scapula. The axial force of 1500 N was selected as a maximal worst-case scenario value, derived from instrumented prostheses measurements reporting forces higher than 200% of body weight during activities of daily living [115].

The non-rigid registration was obtained using the Elastix package, which provides a wide range of parameters to achieve optimal accuracy (presented in Section 2.6.2). All previous studies on bone used B-spline transform for their non-rigid registration with Elastix [116–118]. Elastix indeed recommends a cubic B-spline order. The B-spline function uses a grid on the target image, which the user should refine for each iteration. Conducting a parametric study to determine the optimal registration parameters is critical [118]. In our study, the optimal parameters were obtained by using virtually stretched images and comparing the outcome both qualitatively and quantitatively. Although a stretch instead of compression was applied, it did not change the quality of the transformed image. It was important to stretch the images in the expected deformation directions and by the expected deformation amount in order to optimize the parameters' sensitivity to the applied loading. Registration was obtained within 20 minutes on a 32 CPUs server.

The main strength of this study was to provide original measurements of 3D strain maps within the whole glenoid bone after aTSA. These measurements were obtained using a custom-made loading device, specifically designed for this study. Furthermore, we faithfully replicated the standard clinical surgical setting with the help of preoperative CT scans, preoperative surgical planning software, and patient-specific instruments. We also analyzed the error, by using three consecutive micro-CT scan pairs, instead of the commonly reported analysis performed on single scan pairs only. Another strength of this study was the evaluation of the errors on three different types of scans and especially on a virtually stretched scan, while all previous studies which investigated DVC errors used only one repeated unloaded scan. Besides, our study showed that some DVC parameters can output very small errors for repeated unloaded scans, but may also underestimate the deformation when applied to virtually stretched image. Therefore, we eventually chose DVC parameters providing optimal confidence of the measured deformation after loading, although these parameters did not output the lowest zero-strain error.

In this feasibility study, we applied the technique only to a single sample. In a next step, we will evaluate the variability of the glenoid strain after aTSA with a series of scapulae. A natural variability is indeed expected since the glenoid implant is usually not aligned with the medio-lateral loading axis. For this case, the planned version was 7 degrees (retroversion) and the inclination was zero degrees. In a series of scapulae, the range of glenoid version and inclination should be less than 10 degrees. The measured strain was limited to bone by masking micro-CT images. This masking excluded soft tissue artefacts surrounding the scapula and reduced the measurement errors [93,119].

In conclusion, this technique provides the 3D maps of displacement and strain within the glenoid bone after aTSA. It is based on a custom-made loading device for micro-CT imaging and DVC analysis, and its accuracy and precision levels are sufficient to eventually compare different surgical techniques (reaming, cementing, implant types) or validate numerical models.

2.6 Supplementary Material
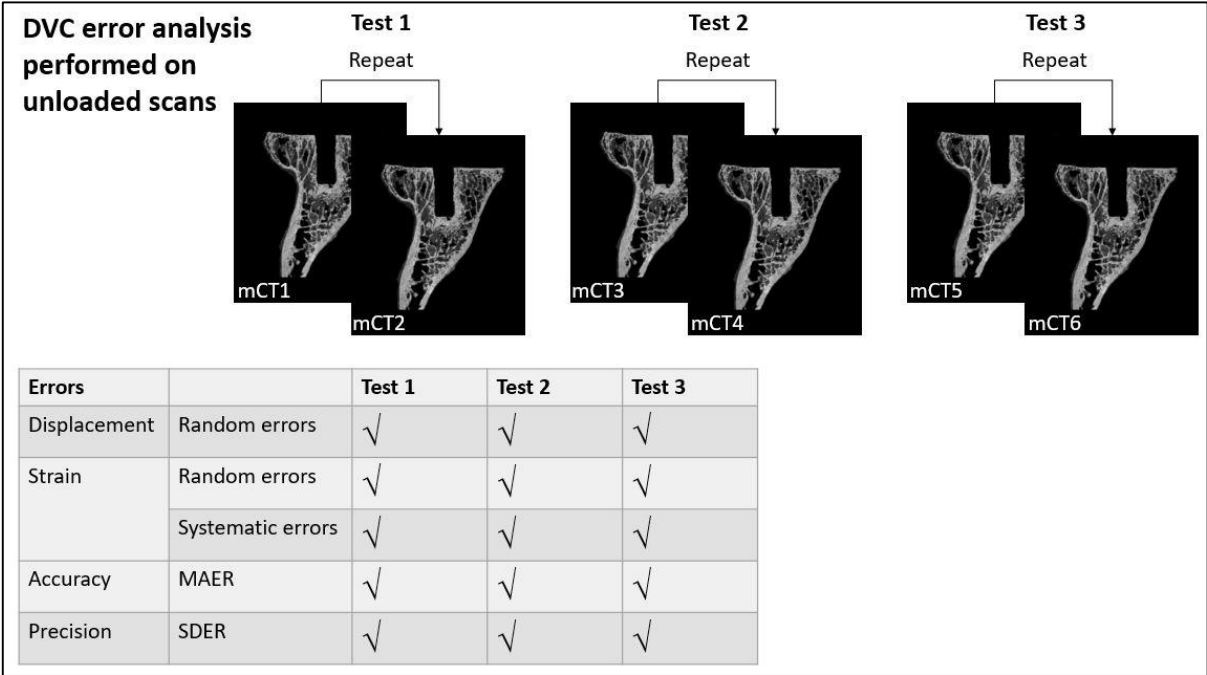
Figure 2:6 Error analysis performed on three pairs of unloaded scans.

2.6.1 Optimal parameters for DVC

The Elastix package provides a wide range of parameters to get optimal non-rigid registration[2]. This optimization was performed on three sets of scan pairs: Set1, Set2, and Set3. Set1 was two same scans (mCT3-mCT3). Set2 was an unloaded scan (mCT3) and the same scan virtually deformed (mCT3s) with a stretch of 0.5% in the three orthogonal directions. Set3 consisted of two repeated unloaded scans (mCT3, mCT4). Each pair was then non-rigidly registered using a combination of parameters (Table 2:1).

Among the most important parameters to tune, grid size, optimization routine and similarity metric were considered. In the present study, a B-spline transform was used. It is important to know that for each registration, Elastix provides a resulting image which needs to be compared to the input images and thus helps to visually eliminate wrong registrations.

The optimization routine was performed in three steps: first, the random displacement errors were computed for Set1. The parameter sets that did not provide zero displacement in all three directions (U1, U2 and U3) were removed. Second, more parameter sets were removed if they provided images that did not match the virtually stretched image of Set2 even if they produced low displacement errors on Set3. For the remaining parameters (i.e. that reproduced the applied stretch), the median of the resulting applied strain in the three axial directions (E11, E22 and E33) were computed. Only three parameter sets remained acceptable (Table 2:2). The third optimization step consisted in calculating the random displacement errors in the three axial directions (U1, U2, U3) for Set3. The parameter set that provided the lowest displacement errors was considered the optimal parameter set. From this parameter analysis (Table 2:2), the optimal setting chosen was #41.

- FinalGridSpacing: 40
- Resolution[3]: 5
- SampleSize: 12000
- Metric: Normalized Correlation Coefficient
- Bins:32
- Optimizer: Standard Gradient Descent gain factor SP_a = 100.

Image properties: For computer memory reasons, all images (8-bit grayscale) were sized around: 1100x1300x1000 voxels, around 40x47x38 mm. In total, around 1060 slices were reconstructed. Registration was obtained within 20 minutes on a linux server with 32 CPUs and 128 GB RAM.

---

[2] elastix.bigr.nl/wiki/index.php/Parameter_file_database
[3] "Resolutions" is a term used by the software developers to designate "iterations

Settings	FinalGridSpacing (voxels)	Resolution	SampleSize	Metric	Bins	Optimizer
1	42	3	12000	AdMattMutInfo	32	StdGradDesc SP=10
2	42	4	12000	AdMattMutInfo	32	StdGradDesc SP=10
3	42	5	12000	AdMattMutInfo	32	StdGradDesc SP=10
4	42	7	12000	AdMattMutInfo	32	StdGradDesc SP=10
6	42	5	12000	AdMattMutInfo	24	StdGradDesc SP=10
7	42	5	12000	AdMattMutInfo	40	StdGradDesc SP=10
8	42	5	12000	AdMattMutInfo	48	StdGradDesc SP=10
9	42	5	12000	AdMattMutInfo	56	StdGradDesc SP=10
10	42	5	12000	AdMattMutInfo	64	StdGradDesc SP=10
11	42	5	12000	AdMattMutInfo	255	StdGradDesc SP=10
12	42	5	12000	AdMattMutInfo	270	StdGradDesc SP=10
13	42	5	12000	AdMattMutInfo	16	StdGradDesc SP=10
14	42	5	24000	AdMattMutInfo	32	StdGradDesc SP=10
15	42	5	32000	AdMattMutInfo	32	StdGradDesc SP=10
16	42	5	24000	AdMattMutInfo	64	StdGradDesc SP=10
17	42	5	12000	AdMattMutInfo	32	StdGradDesc SP=100
18	42	5	12000	AdMattMutInfo	32	StdGradDesc SP=500
19	42	5	12000	AdMattMutInfo	32	StdGradDesc SP=1000
20	42	5	12000	AdMattMutInfo	32	StdGradDesc SP=2000
21	42	5	12000	AdMattMutInfo	32	StdGradDesc default values
22	42	5	12000	AdMattMutInfo	32	AdapStochGrad
23	42	5	12000	AdNormCorr	32	AdapStochGrad
24	42	5	12000	AdNormCorr	32	StdGradDesc SP=10
25	42	5	12000	AdNormCorr	32	StdGradDesc SP=100

26	42	5	12000	AdNormCorr	32	StdGradDesc SP=500
26	42	5	12000	AdNormCorr	32	StdGradDesc SP=1000
27	42	5	12000	AdNormCorr	32	StdGradDesc SP=2000
28	42	5	12000	AdNormCorr	32	StdGradDesc default values
29	42	5	12000	MSD	32	StdGradDesc SP=10
30	42	5	12000	MSD	32	StdGradDesc SP=0.5
31	42	5	12000	MSD	32	StdGradDesc SP=1
32	42	5	12000	MSD	32	StdGradDesc SP=0.2
33	42	5	24000	AdNormCorr	32	AdapStochGrad
34	42	5	12000	AdNormCorr	64	AdapStochGrad
35	42	5	24000	AdNormCorr	64	AdapStochGrad
36	42	5	12000	AdNormCorr	16	StdGradDesc SP=100
37	42	5	12000	AdNormCorr	24	StdGradDesc SP=100
38	42	5	24000	AdNormCorr	32	StdGradDesc SP=100
39	42	5	32000	AdNormCorr	32	StdGradDesc SP=100
40	32	5	12000	AdNormCorr	32	StdGradDesc SP=100
41	40	5	12000	AdNormCorr	32	StdGradDesc SP=100
42	48	5	12000	AdNormCorr	32	StdGradDesc SP=100
43	52	5	12000	AdNormCorr	32	StdGradDesc SP=100
44	56	5	12000	AdNormCorr	32	StdGradDesc SP=100
45	64	5	12000	AdNormCorr	32	StdGradDesc SP=100
46	72	5	12000	AdNormCorr	32	StdGradDesc SP=100
47	80	5	12000	AdNormCorr	32	StdGradDesc SP=100
48	52	5	12000	AdNormCorr	32	StdGradDesc SP=100
49	52	5	12000	AdNormCorr	32	StdGradDesc SP=100

50	42	3	12000	AdNormCorr	32	StdGradDesc SP=100
51	56	3	12000	AdNormCorr	32	StdGradDesc SP=100
52	52	3	12000	AdNormCorr	32	StdGradDesc SP=100
53	56	3	12000	AdNormCorr	32	StdGradDesc SP=100

Table 2:1 List of settings used for the parametric study for non-rigid registration.

	Random displacement errors for Set2 (voxels)		
	U1	U2	U3
41	0.09	0.08	0.12
44	0.10	0.09	0.13
53	0.29	0.22	0.35

Table 2:2 Settings considered for comparison in Set3.

2.6.2 Extended data

This section extends the result section of the main document with more detailed figure and tables associated to error quantification of displacement and strain, and loaded displacement. Test 1 represents DVC applied on mCT1-mCT2, Test 2 represents DVC applied on mCT3-mCT4 and Test 3 represents DVC applied on mCT5-mCT6.

Displacement errors
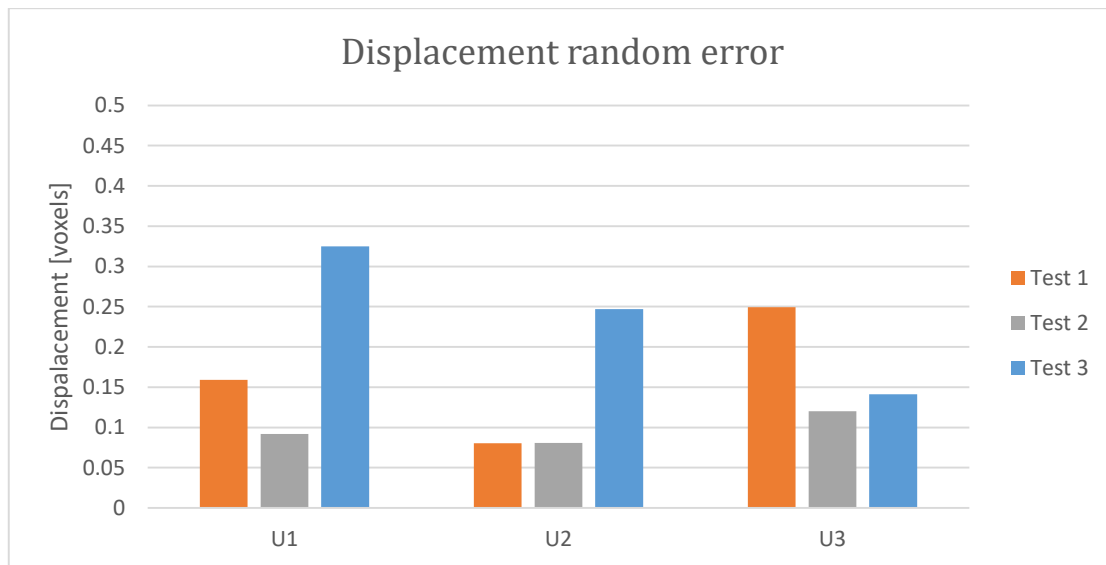
Figure 2:7 Displacement random errors in zero-strain conditions (voxels).
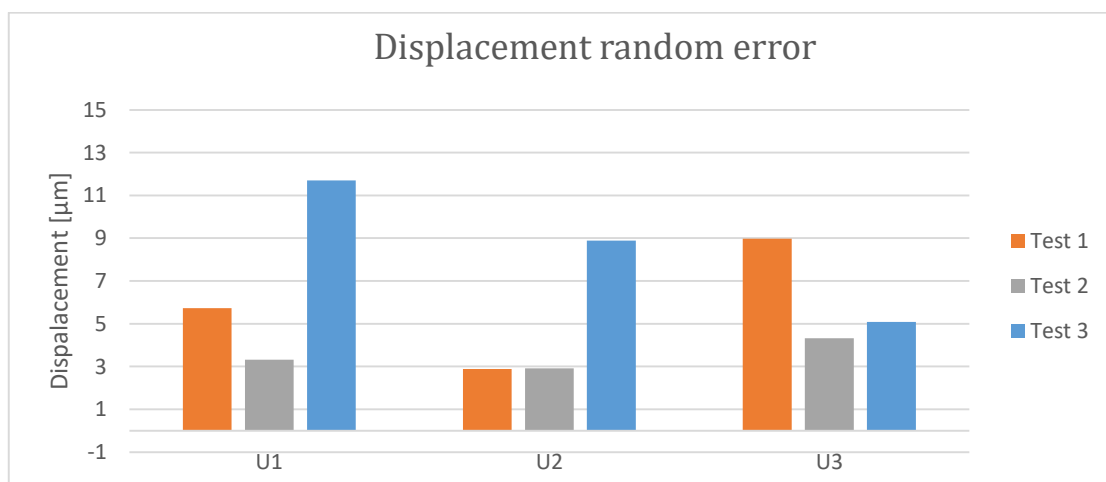
Figure 2:8 Displacement random errors in zero-strain conditions.

	Random error [µm]		
	U1	U2	U3
Test 1	5.7	2.9	9.0
Test 2	3.3	2.9	4.3
Test 3	11.7	8.9	5.1
Average	6.9	4.9	6.1

Table 2:3 Random displacement errors in zero-strain conditions.

Strain errors
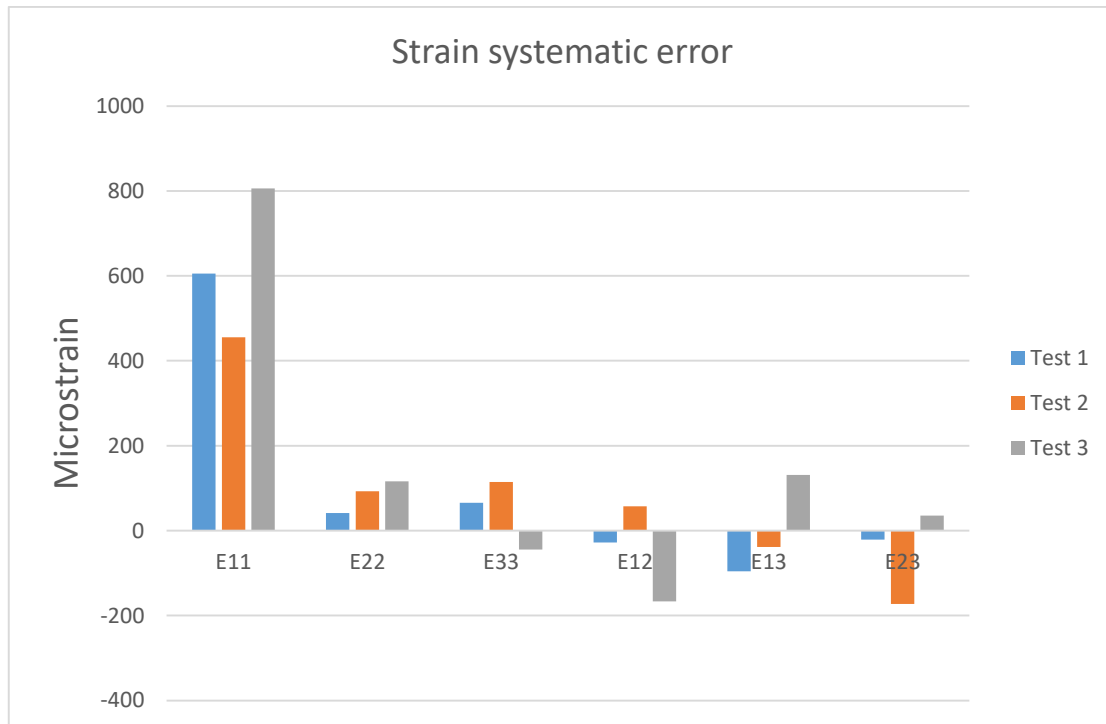
Figure 2:9 Systematic errors in zero-strain conditions for the six components of strain.
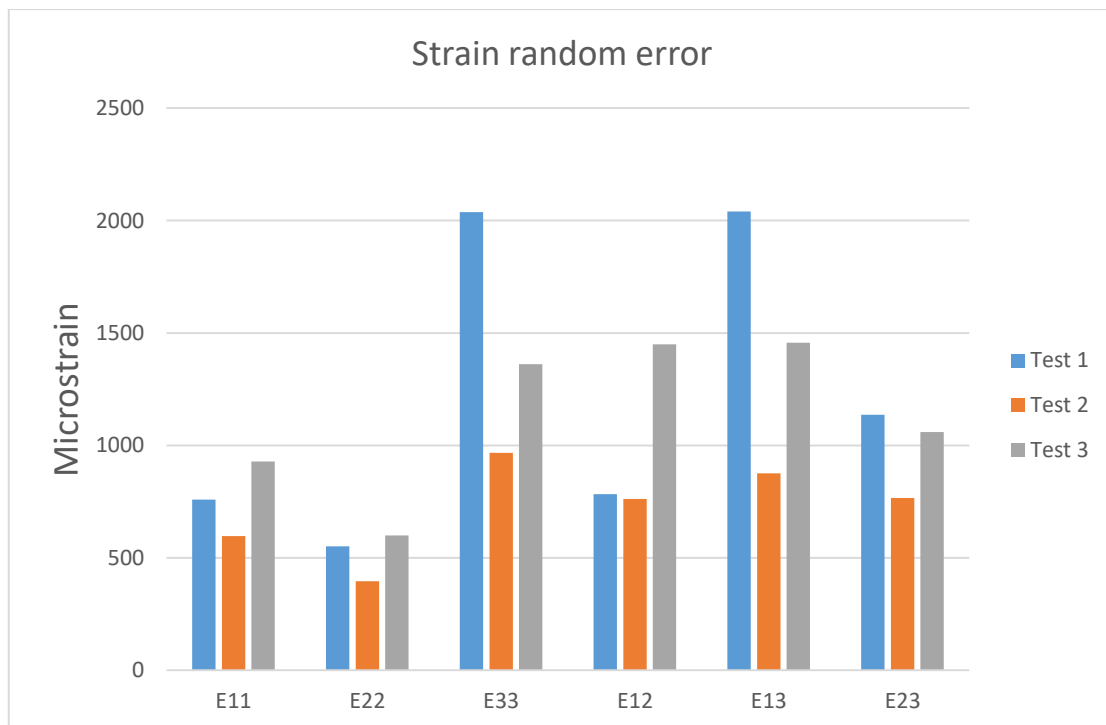
Figure 2:10 Random errors in zero-strain conditions for the six components of strain.
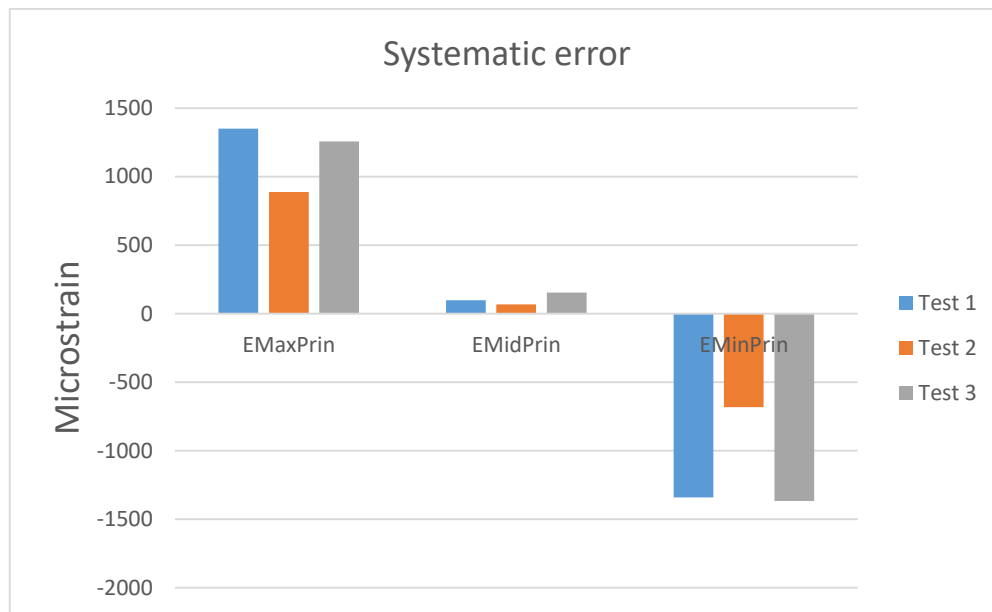
Figure 2:11 Systematic errors for the three principal strain invariants.
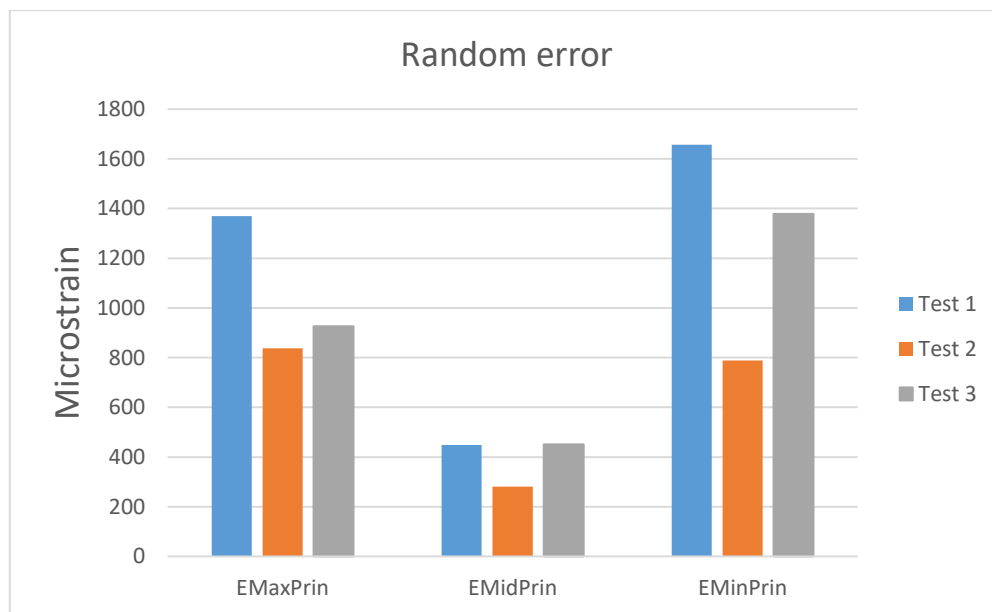
Figure 2:12 Random errors for the three principal strain invariants.

	MAER [με]	SDER [με]
Test 1	800.2	579.8
Test 2	484.2	313.2
Test 3	798.5	427.8
Average	694.3	440.3

Table 2:4 Average accuracy (MAER) and precision (SDER) of strain measurements in zero-strain conditions**.**

	MAER [με]	SDER [με]
Test 1	800.2	579.8
Test 2	484.2	313.2
Test 3	798.5	427.8
Average	694.3	440.3

Table 2:5 Average accuracy (MAER) and precision (SDER) of strain measurements in zero-strain conditions.

VOI error analysis
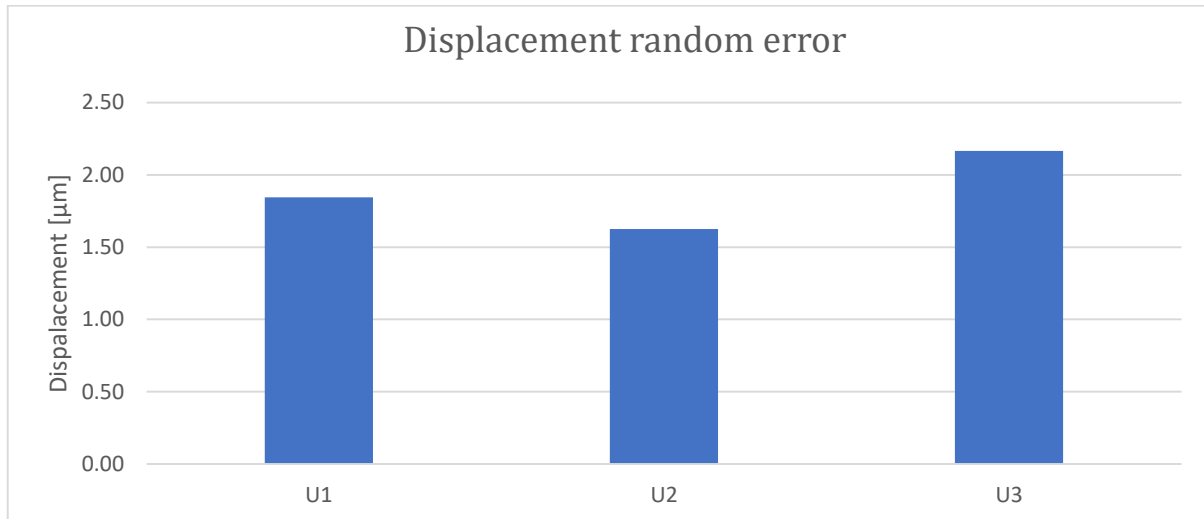
Figure 2:13 Random displacement errors in zero-strain conditions for VOI.
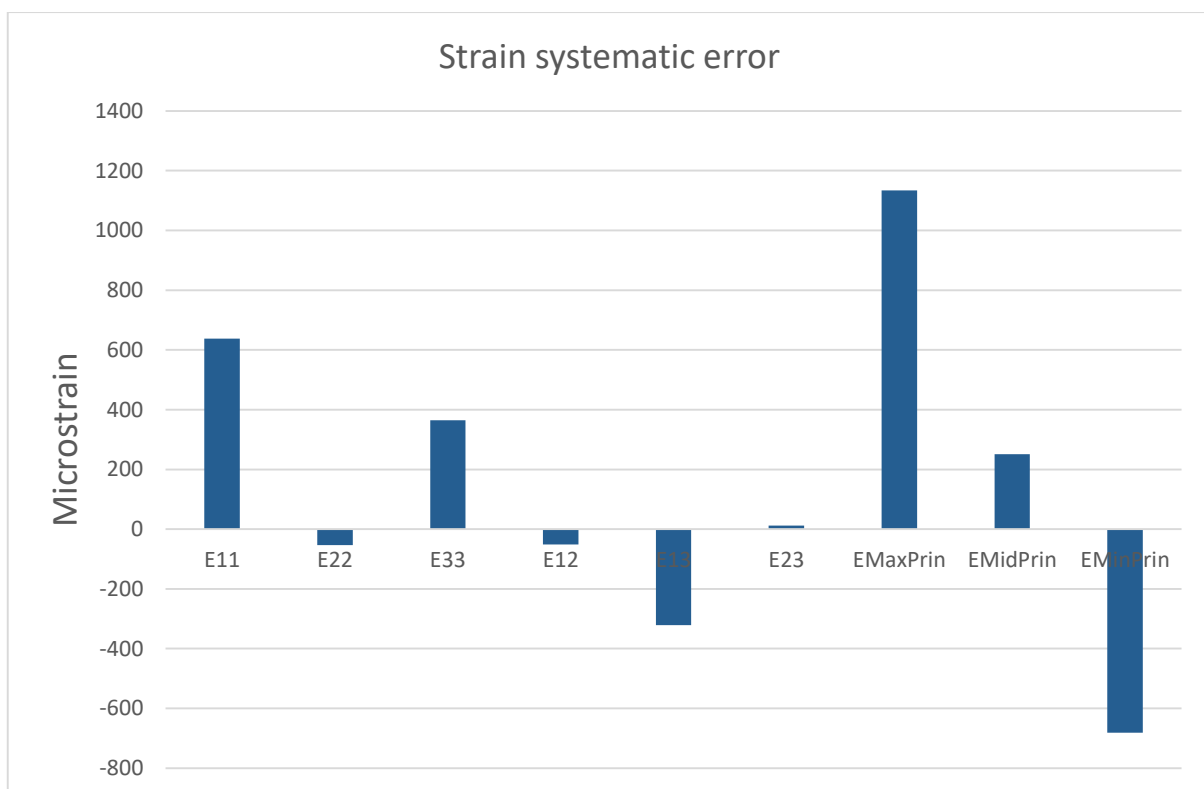
Figure 2:14 Systematic strain errors in zero-strain conditions for VOI.
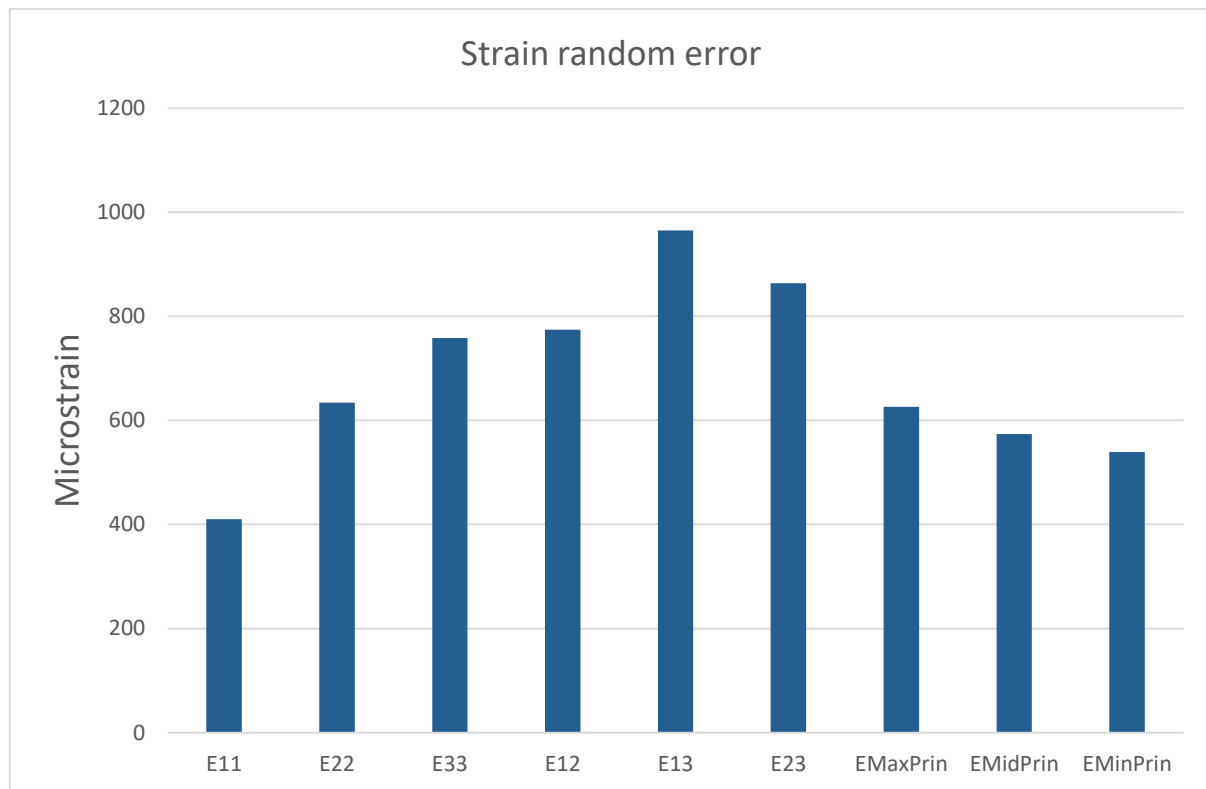
Figure 2:15 Random strain errors in zero-strain conditions for VOI

Loaded displacement

	U1	U2	U3
Average [μm]	-601.0	411.6	145.4
Standard deviation [μm]	600.5	131.6	221.0
Maximum [μm]	-818.9	825.4	797.6

Table 2:6 Average, standard deviation and maximum value of displacement during axial loading (1500 N).

2.6.3   Extended explanations on Elastix software

This section presents details about the Elastix software registration process. For more information, please refer to the manual

For its registration, one image (called moving image, grayscale Intensity ($I_M(x)$)) is aligned to another image (called fixed image, grayscale Intensity ($I_F(x)$), x being the spatial coordinate. Using suitable metric and optimiser, the registration aims at finding the correct transformation $T(x) = x + u(x)$ so that $I_M(x)$ and $I_F(x)$ are aligned. This registration produces the displacement map $u(x)$ we are looking for. Formulated differently, our goal is to find the values of the transformation parameters that minimize the metric (which is a cost function) with respect to the transform T. Mathematically, the goal is to solve the optimization problem of finding the best transformation parameter vector $\mu = arg_\mu^{min} C(\mu; I_F, I_M)$, with C being the cost function to be minimized. The following diagram was taken from the Elastix manual (Figure 2:16) and summarizes the steps and the components needed in the registration process.
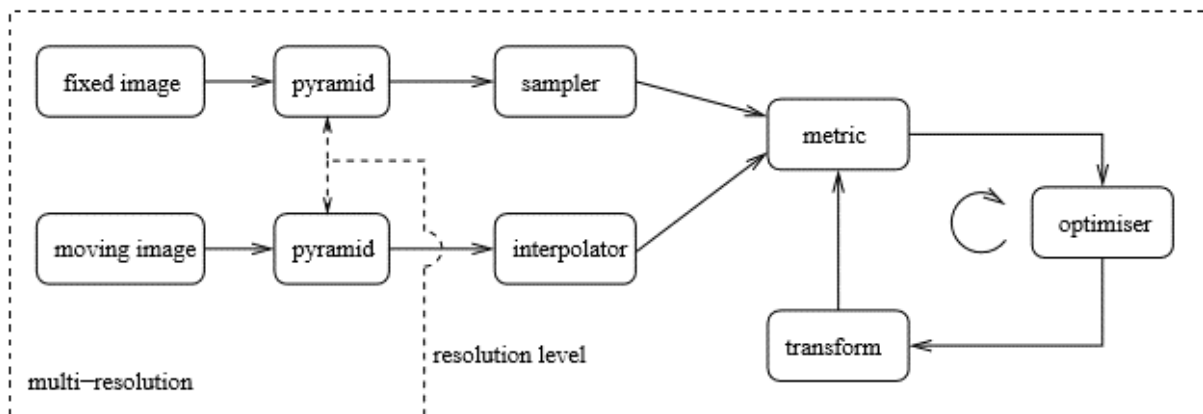
Figure 2:16 Most important components of registration in Elastix.

(Image courtesy of Elastix The Manual v4.8 [120])

In our study, we chose the following components.

Sampler: this component loops over the voxels of the fixed image and compares them to the voxels of the moving image. Many ways are possible: compare each voxel of the images or only an area/subset chosen randomly. In order to reduce memory usage, we chose not to loop over all the voxels of the image but to compare a random subset of voxels on each image. The subset size is determined by the user but its location is chosen randomly at each new iteration. The number of iterations is called "number of resolutions" in Elastix and is represented by the arrow in the Figure above.

Transform: Amongst a wide choice of transformations (translation, rigid, affine etc), we chose a B-Spline transformation with its associated 3rd order B-Spline interpolator. Associated to this transform is the grid spacing. Grid spacing is known in other studies by "nodal spacing". Basically the nodal spacing determines how dense the grid is. The grid is applied on the image to compare it to the fixed image. Elastix gives the possibility to choose a fixed size of grid or to change it (refine it) after each iteration. It is important to mention that in our study and as recommended by Elastix, we start at a high grid size in order to capture the big structures in the image and then to reduce the grid size to capture more detailed structures. For this reason, our approach is both global and local.

Metric: In order to give a measure of transformation quality or similarity measure as called in the manual, a wide choice of metric is available. We chose the Normalized Correlation Coefficient defined in equation 2.6 in the Elastix Manual [120].

$$NCC(\mu; I_F, I_M) = \frac{\sum_{x_i \in \Omega_F}(I_F(x_i) - \overline{I_F}) * (I_M\left(T_\mu(x_i)\right) - \overline{I_F})}{\sqrt{\sum_{x_i \in \Omega_F}(I_F(x_i) - \overline{I_F})^2 * \sum_{x_i \in \Omega_F}(I_M(T_\mu(x_i)) - \overline{I_M})^2}}$$

With $\overline{I_F} = \frac{1}{|\Omega_F|}\sum_{x_i \in \Omega_F} I_F(x_i)$ and $\overline{I_M} = \frac{1}{|\Omega_F|}\sum_{x_i \in \Omega_F} I_M(T_\mu(x_i))$ being the average grey-values.

Optimizer: In order to solve the optimization problem, an iterative optimization routine is needed which involves a "search direction" and a scalar gain factor which controls the step size of this "search". Many optimizers are implemented in Elastix and we chose the Standard Gradient Descent:

$\mu_{k+1} = \mu_k - a_k g(\mu_k)$, with $g(\mu_k) = \frac{\partial C}{\partial \mu}$ evaluated at the current position μ_k and $a_k = \frac{a}{(A+k+1)^\alpha}$

In our case and using Elastix recommendations $a = 100, A = 50$ and $\alpha = 0.6$.

2.6.4   Error analysis on repeated virtually deformed images

This section presents the error analysis performed on repeated virtually deformed images of the unloaded specimen: mCT3-mCT4.

Methods: A fourth error calculation was performed, following a recent study on bovine cortical bone (PMID 30736962) which consists in evaluating the error between two repeated unloaded and masked scans (mCT3 and mCT4): the first scan remained undeformed (mCT3) and a virtual compression of 1% was applied on the second scan (mCT4def). The deformation was applied along X, Y and Z axis, separately. The same DVC and post-processing method were used as presented for the error calculation on virtually deformed scans (Set 2). Systematic (median) and random (standard deviation) errors for each component of strain and for the third principal strain were calculated. Errors were evaluated on the mesh containing the whole image. In a second step, the mesh was cropped to around 50% of its initial volume (VOI1) but still contained: cortical bone, trabecular bone and masked volume. Third, the errors were evaluated on a volume of interest (VOI2) containing bone without the surrounding mask nor cement (Figure 2:17).

Results: Systematic (Figure 2:18) and random (Figure 2:19) errors were highest for the normal components of strain along the deformation direction. Averaged across all three deformation directions, peak systematic errors represented up to 60.4% of the applied deformation when the whole image was considered and decreased to 22.5% for VOI1 and to 0.2% for VOI2. Similar decrease was observed for minimum principal strain which decreased from 43.5% to 15.2 % (VOI1) and to 1% (VOI2).
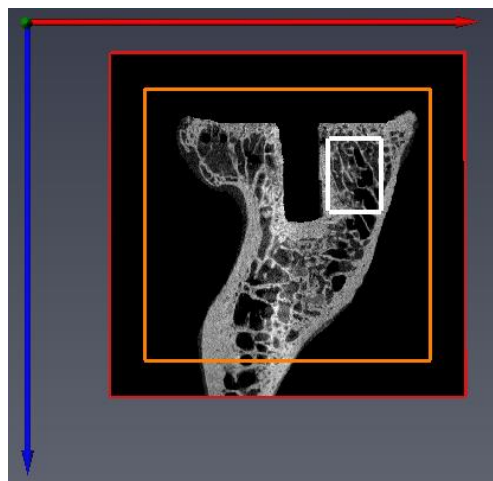
Figure 2:17 MicroCT image of deformed scan (mCT4def), red border. Orange border: cropped image, VOI1. White border: VOI2.

Figure 2:18 Systematic errors for repeated virtually deformed scans (mCT3-mCT4def).

Figure 2:19 Random errors for repeated virtually deformed scans (mCT3-mCT4def).

Discussion: The error calculation on repeated deformed scans (mCT3-mCT4def) was a supplementary step to evaluate the errors associated with the measurement technique presented. The systematic and random errors were highest in the direction of applied deformation, similarly to the study that first introduced this error calculation concept (PMID 30736962). The systematic errors were up to 60% of the applied deformation when the entire volume was investigated and decreased drastically (around 22%) when the outer layers of the image were removed (VOI1) even if VOI1 still included areas of different bone types and border of the bone with the mask. When only bone was investigated (VOI2), the errors were extremely small (0.2%). This trend was observed in the previous study: errors were around 15% of applied deformation (for 1% deformation) and decreased to be similar to zero-strain errors when the outer layers of the images were removed.

Our study found high percentage errors compared to the published study which may have the following causes: the present study analyzed images of the whole specimen (including edges, trabecular bone, cortical bone and cement) while the previous study investigated a VOI containing cortical bone. Moreover, this relative high error may be due to relatively noisier images of the single specimen investigated. More specimens need to be tested in order to confirm the trend. Lastly, a close comparison is not fair due to the different machines (micro – CT versus Synchrotron) and scanning resolutions (36 µm versus 1.6 µm) used.

Chapter 3   Bone displacement after anatomical Total Shoulder Arthroplasty measured by Digital Volume Correlation and predicted by CT-derived finite element model

This chapter describes the validation of patient-specific finite element models with respect to measured DVC displacement, strain and joint reaction force.
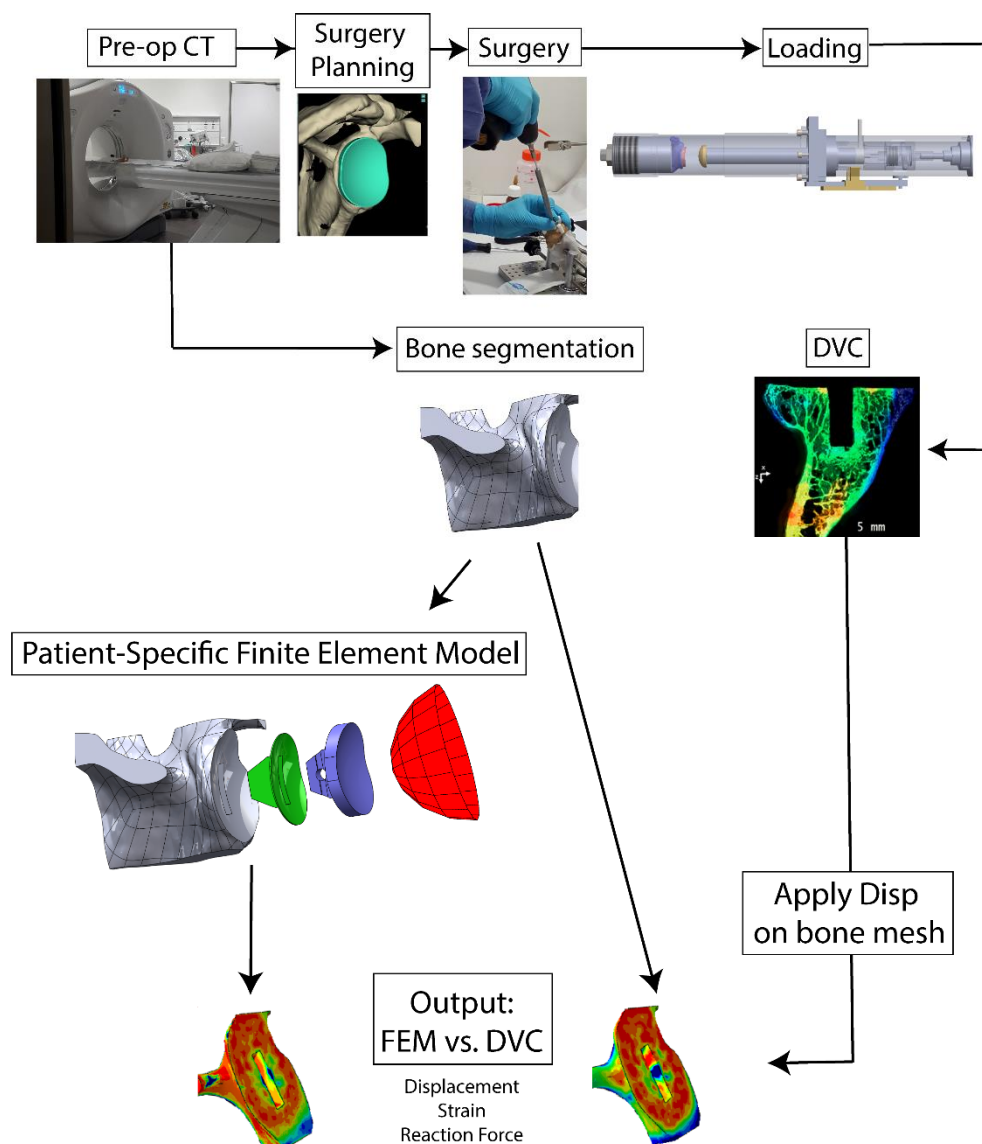
3.1   Abstract

CT-derived finite element (FE) models of glenoid bone can be used to answer clinical questions, but experimental validation is challenging. The goal of the study was to compare FE model predictions against Digital Volume Correlation (DVC) results. Five cadaveric glenoid samples were loaded (750 N) after total shoulder arthroplasty (TSA) and their displacement, strain, and reaction force were compared to FE models. 35 different bone constitutive laws were simulated for each FE model. Displacement correlation was very strong (R^2 = 1.00), but moderate for strain (R^2 = 0.37) and for force (R^2 = 0.66). Validation of FE models of TSA with DVC remains challenging.

Keywords: finite element model; glenoid; micro-CT; bone strain; digital volume correlation; total shoulder arthroplasty.

3.2   Introduction

Specimen-specific finite element (FE) models of the shoulder joint are very useful non-invasive tools to predict general bone biomechanical behaviour [19,71,73,74] However, they rely on a series of assumptions and simplifications and one of their recurrent limitation is the lack of experimental validation [69,73,74]. Especially, in the context of anatomical Total Shoulder Arthroplasty (aTSA), FE models are helpful to identify the causes of glenoid implant loosening which was reported as the most common sort of implant failure [19,21–23].

The emerging Digital Volume Correlation (DVC) combined to micro-Computed Tomography (µCT) and mechanical loading set-up enables the measurement of full-field quantities such as displacement and strain. DVC was used in hip arthroplasty and vertrebroplasty to measure strain in trabecular bone [82,84,86,89], cortical bone [83,84], whole bones [85,88,91] and on in situ mice tibiae [87,90]. In the context of shoulder joint, it was used to quantify micromotion around cementless porcine glenoid implants after aTSA [69] and strain on cemented glenoid bone [74] under concentric, anterior and posterior loading (750 N). Recently, two studies aimed at validating FE models against DVC measurements: [73] correlated the displacements predicted by Quantitative Computer Tomography (QCT)-derived FE model of four cadaveric scapulae against displacements measured by DVC. The specimens were imaged in a µCT during loading. A very good correlation ($R^2 = 0.79 - 1.99$, slope $= 0.87 - 1.09$) was found between DVC-measured displacements and FE model-predicted displacements when the boundary conditions of the experiments were applied on the model. The second study [76] investigated FE model predictions of displacement and reaction force of glenoid under loading for 15 different bone constitutive laws against DVC measurements. Excellent DVC – FE model agreement was achieved when boundary conditions of the experiment were used ($R^2 = 0.82 - 1.00$, slope $= 0.86 - 1.06$). Most recently, compressive strains of osteoarthritic humeral head [77] resp. of scapula [78] predicted by specimen – specific FE models were compared to DVC – measured strains. Excellent agreement was found ($R^2 = 0.80$, slope $= 0.83$) [77] resp. good agreement ($R^2 = 0.73 - 0.75$, slope $= 0.54$–0.59) [78] were found when boundary conditions of the experiment were used.

One commonly cited limitation of recent FE models was the lack of realistic constitutive material law used to mechanically describe bone behavior. Although many constitutive laws exist [75,76] and more and more FE models use Density-Young's Modulus (ρ-E) relationships, with density derived from computed tomography (CT) data [5,65,69–72], there is no consensus regarding the best-suited material law for glenoid bone under loading [75,76] which has a direct impact on the validation potential of said models [69,76].

The primary goal of the present study was to quantify the accuracy of bone displacement, bone strain and bone reaction force after aTSA predicted by CT-derived specimen-specific FE models against experimental

DVC values. The secondary goal of this study was to determine the best-suited bone material law among reported ones in the literature. Five specimens were used for this comparison. They were first implanted with a polyethylene glenoid component, then loaded within μCT loading device. The aTSA specimens were imaged before and during loading to derive experimental displacement and strain using DVC. A FE model was created for each specimen, from preoperative CT data, and 35 bone material laws were tested in order to find the one that would enable the best experiment-model agreement.

3.3   Materials and Methods

3.3.1   Digital Volume Correlation

Five fresh-frozen male cadaveric scapulae were used for this study (Table 3:1). Each specimen scanned using typical clinical CT parameters (Discovery CT750 HD, GE Healthcare, Waukesha, WI, USA). An anthropomorphic thorax K2HPO4 phantom (QRM, Moehrendorf, Germany) with a synthetic humerus (Sawbones, Vashon Island, WA, USA) and saline plastic bags simulating rotator cuff muscles were used to replicate in-vivo x-ray attenuation in the experimental setup. Only keeled cemented glenoid implants were used (AEQUALIS™ PERFORM, Tornier-Wright Medical, Montbonnot-Saint-Martin, France). To avoid beam hardening metal artifacts, metallic radiopaque markers within the implant keel were removed by the manufacturer. A senior shoulder surgeon (AF) used a 3D preoperative planning software and patient-specific instrumentation (BLUEPRINT™ 3D Planning, Tornier-Wright Medical, Montbonnot-Saint-Martin, France) to perform the arthroplasty. All specimens were cut frozen and potted in polyurethan resin for mechanical testing.

Each specimen was inserted in a µCT loading device, scanned unloaded, and then loaded (750 N). Preconditioning and relaxation delay were performed between unloaded and loaded scan. The scanning resolution was 36 µm. Images were reconstructed using a ring artifact reduction (NRecon v1.6.10.4, Bruker micro-CT, Kontich, Belgium). DVC was used to estimate the displacement field of each specimen. We used Elastix-Transformix open-source registration software [111], with non-rigid registration, multi-resolution B-spline transform and gradient-descent optimization of normalized correlation coefficient similarity metric (1.4 mm nodal spacing, precision = 440.3 µε, accuracy = 694.3 µε). Strain was derived from displacement using Abaqus FE solver (v.6.14, Simulia, Dassault Systèmes, Providence, RI, USA). Details of this experimental setup are already reported [121].

Specimens	Age	Height [cm]	Weight [kg]	Density, ρK2HPO4 [g/cm3]	Side
S1	77	175	91	0.228 ± 0.141	R
S2	84	180	78	0.185 ±0.129	L
S3	67	178	77	0.157 ±0.109	L
S4	59	188	86	0.161 ±0.088	L
S5	85	155	73	0.177 ±0.127	L

Table 3:1 Description of the specimens used in the study. In order to calculate the density of each specimen, the K2HPO4 calibration phantom was used to convert HU into K2HPO4 equivalent density (ρ_{K2HPO4}): ρ_{K2HPO4} [g/cm3] = HU/1460.

3.3.2 Finite Element Model

For each specimen, the preoperative CT was rigidly registered to the unloaded µCT, in order to replicate the experiment positioning. Bone was segmented from CT. The Computer Aided Design (CAD) file of the implant was provided by the manufacturer, and was positioned as in the µCT. These above steps were performed using Amira 2019.2 (FEI SAS, Burlington, MA, USA). Bone surface triangular mesh creation and smoothing were performed with Geomagic Design X (3D Systems, Inc). The glenoid bone geometry and placed glenoid implant were imported in Solidworks 2019 (Dassault Systèmes SolidWorks Corporation). Virtual implantation was performed according to the 3D preoperative planning. A cement layer with a uniform thickness of 0.5 mm was considered, except at the backside of the keel, where the cement thickness was 2 mm, due to 1.5 mm polyethylene removal by the manufacturer during radiopaque markers removal. The scapular bone cut, glenoid implant, and cement layer were imported into Abaqus. A rigid hemisphere was added in the Abaqus model to replicate the articular surface of the humeral component (Figure 3:1). Quadratic tetrahedral elements (C3D10) were used for bone, implant and cement. The bone was assigned 1.5 mm sized mesh. Mesh size was chosen based on a mesh convergence study presented in section 5.6.2.
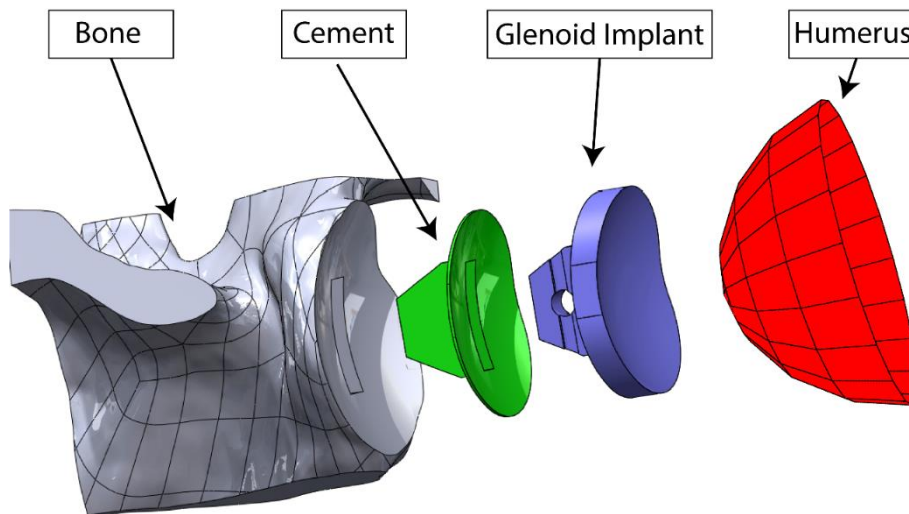
Figure 3:1 Specimen-specific finite element model.

For the implant and cement, the material properties were provided by the manufacturer. For bone, Young's Modulus was assigned based on several reported density-elasticity relationships [69,71,122–129]. A MATLAB (R2017b, The Mathworks Inc, Natick, USA) script was written to assign CT numbers as Hounsfield units (HU) on each node of the FE mesh from the preoperative CT. The K2HPO4 calibration phantom scanned with each specimen during preoperative CT provided the following HU to K2HPO4 equivalent density ($\rho_{K_2HPO_4}$) conversion, $\rho_{K_2HPO_4}$ was called hereafter "ρ_{CT}".

$$\rho_{CT}[\text{g/cm}^3] = \text{HU}/1460$$

Equation 3:1: HU to K2HPO4 equivalent density (ρK2HPO4) conversion

Most of the density-elasticity relationships (ρ-E) investigated expressed Young's Modulus with apparent density ρ_{app}, thus, the following ρ_{CT} to apparent density ρ_{app} conversion was used [129] :

$$\rho_{app} = 2.192 * \rho_{CT} + 0.007$$

Equation 3:2: ρCT to apparent density ρapp conversion

Specifically for Keller's law [124], apparent density ρ_{app} was converted to ash density ρ_{ash} using [130] :

$$\rho_{ash} = 0.6 * \rho_{app}$$

Equation 3:3: ρash to apparent density ρapp conversion

We also considered several values for the threshold of apparent density (ρ_{app}) distinguishing trabecular and cortical bone. Different values for this threshold are reported in the literature [76], but only the following most commonly used were chosen: $\rho_{app} = 1.00 \; g/cm^3$ [131] and $\rho_{app} = 1.8 \; g/cm^3$ [132]. Additionally, $\rho_{app} = 1.2 \; g/cm^3$ was used. The combination of ρ-E and density threshold resulted in 35 different bone material laws (Table 3:2).

To replicate the boundary conditions of the experiment, bone nodal displacements from the experiment were assigned on the articular surface, on the medial surface (5 mm from the back of the keel of the implant), on the scapular spine and on the coracoid.

ρ-E	Density transition	Equation
L1 [125]	n.a.	$E_{Bone} = 15'000 * (\frac{\rho_{app}}{1.8})^2$
L2 [124,125]	$\rho_{app} = 1 \, g/cm^3$	$E_{trab} = 15'000 * (\frac{\rho_{app}}{1.8})^2$ $E_{cort} = 10'200 * \rho_{ash}^{2.01}$
L3	$\rho_{app} = 1.2 \, g/cm^3$	$E_{trab} = 15'000 * (\frac{\rho_{app}}{1.8})^2$ $E_{cort} = 10'200 * \rho_{ash}^{2.01}$
L4	$\rho_{app} = 1.8 \, g/cm^3$	$E_{trab} = 15'000 * (\frac{\rho_{app}}{1.8})^2$ $E_{cort} = 10'200 * \rho_{ash}^{2.01}$
L5 [122,125]	$\rho_{app} = 1 \, g/cm^3$	$E_{trab} = 15'000 * (\frac{\rho_{app}}{1.8})^2$ $E_{cort} = 90 * \rho_{app}^{7.4}$
L6	$\rho_{app} = 1.2 \, g/cm^3$	$E_{trab} = 15'000 * (\frac{\rho_{app}}{1.8})^2$ $E_{cort} = 90 * \rho_{app}^{7.4}$
L7	$\rho_{app} = 1.8 \, g/cm^3$	$E_{trab} = 15'000 * (\frac{\rho_{app}}{1.8})^2$ $E_{cort} = 90 * \rho_{app}^{7.4}$
L8 [127]	n.a.	$\rho_{app} < 0.35, E_{Bone} = 1049.45 * 10^6 * \rho_{app}^2$ $0.35 < \rho_{app} < 1.8, E_{Bone} = 3 * 10^{-6} * \rho_{app}^3$
L9 [124,127]	$\rho_{app} = 1 \, g/cm^3$	$\rho_{app} < 0.35, E = 1049.45 * 10^6 * \rho_{app}^2$ $0.35 < \rho_{app} < 1, E = 3 * 10^{-6} * \rho_{app}^3$ $\rho_{app} > 1, E = 10'200 * \rho_{ash}^{2.01}$
L10	$\rho_{app} = 1.2 \, g/cm^3$	$\rho_{app} < 0.35, E = 1049.45 * 10^6 * \rho_{app}^2$ $0.35 < \rho_{app} < 1, E = 3 * 10^{-6} * \rho_{app}^3$ $\rho_{app} > 1.2, E = 10'200 * \rho_{ash}^{2.01}$
L11	$\rho_{app} = 1.8 \, g/cm^3$	$\rho_{app} < 0.35, E = 1049.45 * 10^6 * \rho_{app}^2$ $0.35 < \rho_{app} < 1, E = 3 * 10^{-6} * \rho_{app}^3$ $\rho_{app} > 1.8, E = 10'200 * \rho_{ash}^{2.01}$
L12 [129]	n.a.	$E_{Bone} = 32'790 * \rho_{CT}^{2.307}$
L13 [124,129]	$\rho_{app} = 1 \, g/cm^3$	$E_{trab} = 32'790 * \rho_{CT}^{2.307}$ $E_{cort} = 10'200 * \rho_{ash}^{2.01}$
L14	$\rho_{app} = 1.2 \, g/cm^3$	$E_{trab} = 32'790 * \rho_{CT}^{2.307}$ $E_{cort} = 10'200 * \rho_{ash}^{2.01}$
L15	$\rho_{app} = 1.8 \, g/cm^3$	$E_{trab} = 32'790 * \rho_{CT}^{2.307}$ $E_{cort} = 10'200 * \rho_{ash}^{2.01}$
L16 [122,129]	$\rho_{app} = 1 \, g/cm^3$	$E_{trab} = 32'790 * \rho_{CT}^{2.307}$ $E_{cort} = 90 * \rho_{app}^{7.4}$
L17	$\rho_{app} = 1.2 \, g/cm^3$	$E_{trab} = 32'790 * \rho_{CT}^{2.307}$ $E_{cort} = 90 * \rho_{app}^{7.4}$
L18	$\rho_{app} = 1.8 \, g/cm^3$	$E_{trab} = 32'790 * \rho_{CT}^{2.307}$ $E_{cort} = 90 * \rho_{app}^{7.4}$
L19 [128]	n.a.	$E_{bone} = 11'035.9 * \rho_{app}^{2.13}$
L20 [124,128]	$\rho_{app} = 1.8 \, g/cm^3$	$E_{trab} = 11'035.9 * \rho_{app}^{2.13}$ $E_{cort} = 10'200 * \rho_{ash}^{2.01}$
L21 [122,128]	$\rho_{app} = 1 \, g/cm^3$	$E_{trab} = 11'035.9 * \rho_{app}^{2.13}$ $E_{cort} = 90 * \rho_{app}^{7.4}$

L22	$\rho_{app} = 1.8 \ g/cm^3$	$E_{bone} = 11'035.9 * \rho_{app}{}^{2.13}$ $E_{cort} = 90 * \rho_{app}{}^{7.4}$
L23 [126]	n.a.	$E_{Bone} = 8'920 * \rho_{app}{}^{1.83}$
L24 [124,126]	$\rho_{app} = 1 \ g/cm^3$	$E_{trab} = 8'920 * \rho_{app}{}^{1.83}$ $E_{cort} = 10'200 * \rho_{ash}{}^{2.01}$
L25	$\rho_{app} = 1.2 \ g/cm^3$	$E_{trab} = 8'920 * \rho_{app}{}^{1.83}$ $E_{cort} = 10'200 * \rho_{ash}{}^{2.01}$
L26	$\rho_{app} = 1.8 \ g/cm^3$	$E_{trab} = 8'920 * \rho_{app}{}^{1.83}$ $E_{cort} = 10'200 * \rho_{ash}{}^{2.01}$
L27 [71]	n.a.	$0.35 < \rho_{app} < 1.8, E = 3 * 10^{-6} * \rho_{app}{}^{3}$ $\rho_{app} > 1.8, E = 17'500 MPa$
L28 [123]	n.a.	$E = 60 + 900 * \rho_{app}{}^{2}$
L29 [123,124]	$\rho_{app} = 1 \ g/cm^3$	$E_{trab} = 60 + 900 * \rho_{app}{}^{2}$ $E_{cort} = 10'200 * \rho_{ash}{}^{2.01}$
L30	$\rho_{app} = 1.2 \ g/cm^3$	$E_{trab} = 60 + 900 * \rho_{app}{}^{2}$ $E_{cort} = 10'200 * \rho_{ash}{}^{2.01}$
L31	$\rho_{app} = 1.8 \ g/cm^3$	$E_{trab} = 60 + 900 * \rho_{app}{}^{2}$ $E_{cort} = 10'200 * \rho_{ash}{}^{2.01}$
L32 [122,123]	$\rho_{app} = 1 \ g/cm^3$	$E_{trab} = 60 + 900 * \rho_{app}{}^{2}$ $E_{cort} = 90 * \rho_{app}{}^{7.4}$
L33	$\rho_{app} = 1.2 \ g/cm^3$	$E_{trab} = 60 + 900 * \rho_{app}{}^{2}$ $E_{cort} = 90 * \rho_{app}{}^{7.4}$
L34	$\rho_{app} = 1.8 \ g/cm^3$	$E_{trab} = 60 + 900 * \rho_{app}{}^{2}$ $E_{cort} = 90 * \rho_{app}{}^{7.4}$
L35 [69]	n.a.	$0.1 < \rho_{app} < 1.3, E = 60 + 900 * \rho_{app}{}^{2}$ $\rho_{app} > 1.3, E = 90 * \rho_{app}{}^{7.4}$

Table 3:2 Material laws used, (n.a. = not applicable). Following relationships were used: ρ_{CT} [g/cm3] = ρ_{K2HPO4} = HU/ 1460. ρ_{app} =2.192* ρ_{CT} +0.007 [129] and ρ_{ash} = 0.6* ρ_{app} [130].

3.3.3 Output

To compare FE model predictions and DVC measurements, the following three metrics were used: 1) displacement of the bone in three orthogonal directions, 2) minimum principal strain of the bone and 3) reaction force of the bone in the loading direction. These three metrics were considered at each node of the FE model and compared to the corresponding DVC measurements. Linear correlation between FE model and DVC was quantified by the coefficient of determination (R^2), slope (A), y-intercept (B), Root Mean Square Error (RMSE) and maximum error (MaxError = maximum difference between FE model and DVC). We excluded from this correlation the nodes where boundary conditions were applied. Outlier nodes were excluded from the analysis using 5x the Cook's distance [73,133]. We performed this linear regression for each of the 35 material laws, for each of the five specimens, and also with all five specimens pooled together. This resulted in a total of 210 DVC to FE model statistical comparisons. The performance of the material law was quantified first according to the closest slope and R^2 to unity scored by each metric when all specimens were pooled. In a

second step, the laws that presented the best FE model-DVC agreement for reaction force and the lowest RMSE were considered the best-suited laws.

3.4   Results

Extended results are reported in Supplementary Material Section 3.6.

3.4.1   Displacement

Across all material laws and for pooled specimens, the correlation was very strong in the three directions of displacement: coefficient of determination R^2 = 1.00, slope A = 1.00 and y-intercept B from -2.93 to 0.63, RMSE from 9.18 to 13.94 and MaxError µm from 52.60 to 74.74 µm (Table 3:4).

Across all material laws and for each specimen, the correlation between FE model and DVC displacement was strong (Table 3:3). In the direction of loading (Uz), R^2 ranged from 0.76 to 0.99, A ranged from 0.90 to 1.00, B ranged from -12.3 µm to 9.6 µm, RMSE ranged between 7.15 and 14.63 and MaxError ranged between 31.95 and 68.96 µm. In the other two directions Ux and Uy, R^2 ranged from 0.70 to 0.98, A from 0.78 to 1.00, B from -17.10 µm to 33.89 µm, RMSE from 3.76 to 16.95 µm and MaxError from 13.74 to 85.09 µm. The weakest correlations were observed for specimens S1 and S4.

DISPLACEMENT	Ux			Uy			Uz		
	R^2	Slope A	y-intercept B	R^2	Slope A	y-intercept B	R^2	Slope A	y-intercept B
S1	0.71-0.79	0.82-0.97	-17.10 to -4.06	0.89-0.91	0.94-0.96	-10.6 to -4.83	0.98	1	2.69 to 3.58
S2	0.95-0.97	0.95-0.97	6.47 to 17.84	0.84-0.91	0.87-1.00	-5.32 to 9.11	0.99	0.97-0.99	-0.15 to 3.10
S3	0.96-0.98	1	-1.22 to 2.13	0.89-0.93	0.96-1.00	-11.60 to -4.81	0.98	1	-12.33 to -10.37
S4	0.70-0.72	0.78-0.81	5.25 to 6.23	0.75-0.8	0.78-0.86	-6.95 to -4.04	0.76-0.82	0.9-0.94	6.73 to 9.64
S5	0.88-0.92	0.97-1.00	3.23 to 9.08	0.88-0.92	0.91-0.94	21.14 to 33.89	0.99	1	1.23 to 6.67

DISPLACEMENT	Ux		Uy		Uz	
	RMSE	MaxError	RMSE	MaxError	RMSE	MaxError
S1	6.45 - 7.58	26.24 - 32.94	7.78 - 8.70	30.03 - 34.76	7.74 - 8.41	36.20 - 39.63
S2	10.44 – 13.87	38.11 - 51.69	6.02 - 8.06	18.85 - 25.24	10.14 - 11.96	31.95 - 41.69
S3	11.40 - 15.68	54.80 - 74.74	9.41 - 11.31	49.60 - 65.25	13.20 - 14.63	61.31 - 68.96
S4	6.03 - 6.22	26.41 - 27.90	3.76 - 4.16	13.53 - 15.72	7.15 - 8.26	35.97 - 45.60
S5	14.01 - 16.95	60.58 - 71.03	11.62 to 14.04	45.33 - 86.27	12.20 - 12.97	61.81 - 67.50

Table 3:3 linear regression results for displacement for each specimen.

	Ux					Uy					Uz				
	R²	A	B	RMSE	MaxError	R²	A	B	RMSE	MaxError	R²	A	B	RMSE	MaxError
all ρ-E	1	1	-1.95 to -1.58	11.41 to 13.94	60.58 to 74.74	1	1	-2.93 to -0.24	9.18 to 10.44	52.60 to 86.27	1	1	-0.73 to 0.63	11.62 to 12.52	54.48 to 68.96

Table 3:4 Linear regression results for displacement for all specimens pooled and across all material laws investigated expressed with coefficient of determination R^2, slope A, y-intercept b, RMSE and MaxError.

3.4.2 Minimum Principal Strain

For Minimum Principal Strain, the correlation between FE model and DVC was weak across all material laws and for all specimens pooled (Figure 3:2): R^2 ranged between 0.28 and 0.37 while A ranged between 0.51 and 0.70. RMSE ranged between 7190 and 7618 µε and MaxError ranged between 86770 and 90210 µε (Suppl. Material, Table 3:11).

Investigating each specimen separately, the correlation was moderate for S4 and S5 (R^2 = 0.38 to 0.53 and A = 0.53 – 0.88), weak for S1 and S3 (R^2 = 0.15 to 0.36 and A = 0.49 – 0.74) and very weak for S2 (R^2 = 0.07 to 0.14 and A = 0.31 – 0.53) (Table 3:5).
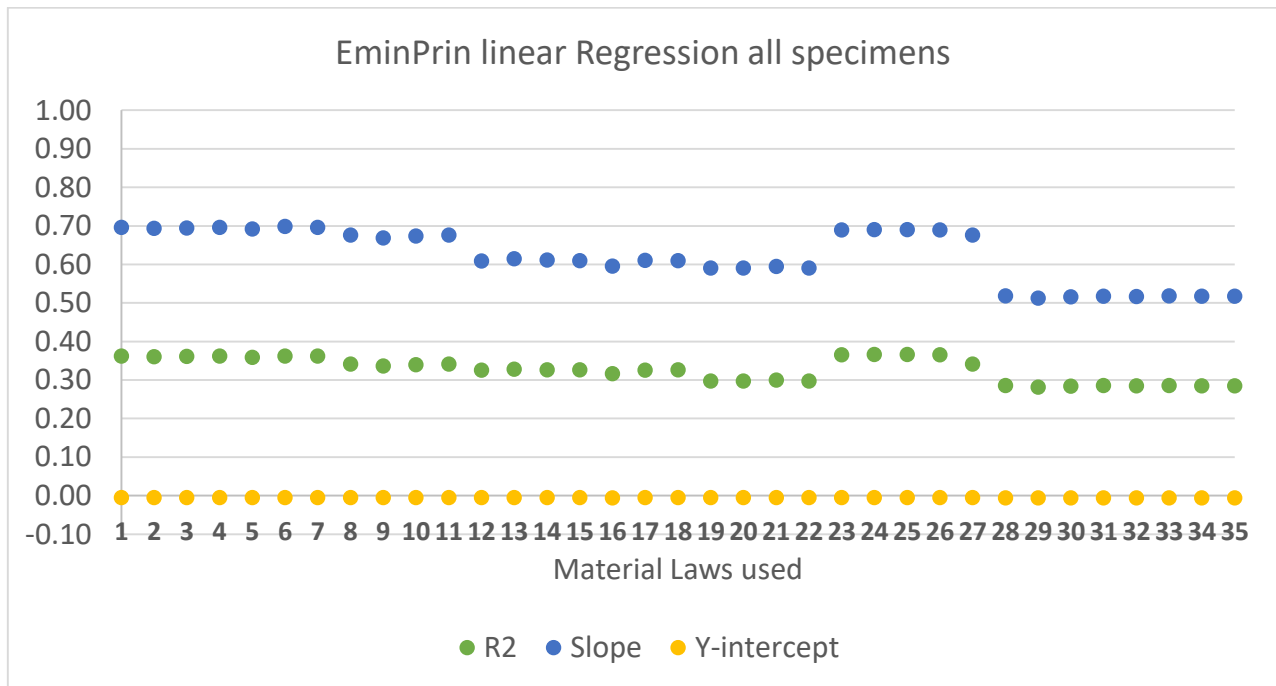
Figure 3:2 Minimum Principal Strain linear regression for all specimens pooled and for all material laws.

	R²	Slope	y-intercept
S1	0.15-0.23	0.57-0.74	0.00
S2	0.07-0.14	0.31-0.53	-0.01
S3	0.28-0.36	0.49-0.65	-0.01 to 0.0
S4	0.38-0.46	0.61-0.68	0.00
S5	0.35-0.53	0.53-0.88	-0.01 to 0.0

Table 3:5 linear regression results for reaction force for each specimen and for all material laws.

3.4.3 Reaction Force

High variation was found in the agreement between FE model-predicted and experimentally applied reaction force (Figure 3:3). The difference between predicted and experimental reaction force varied across all material laws for pooled specimens: R^2 ranged between 0.22 to 0.66 while slope ranged between 0.03 and 0.96. RMSE ranged between 0.52 and 0.78 N while MaxError ranged between 8.60 and 24.90 N.
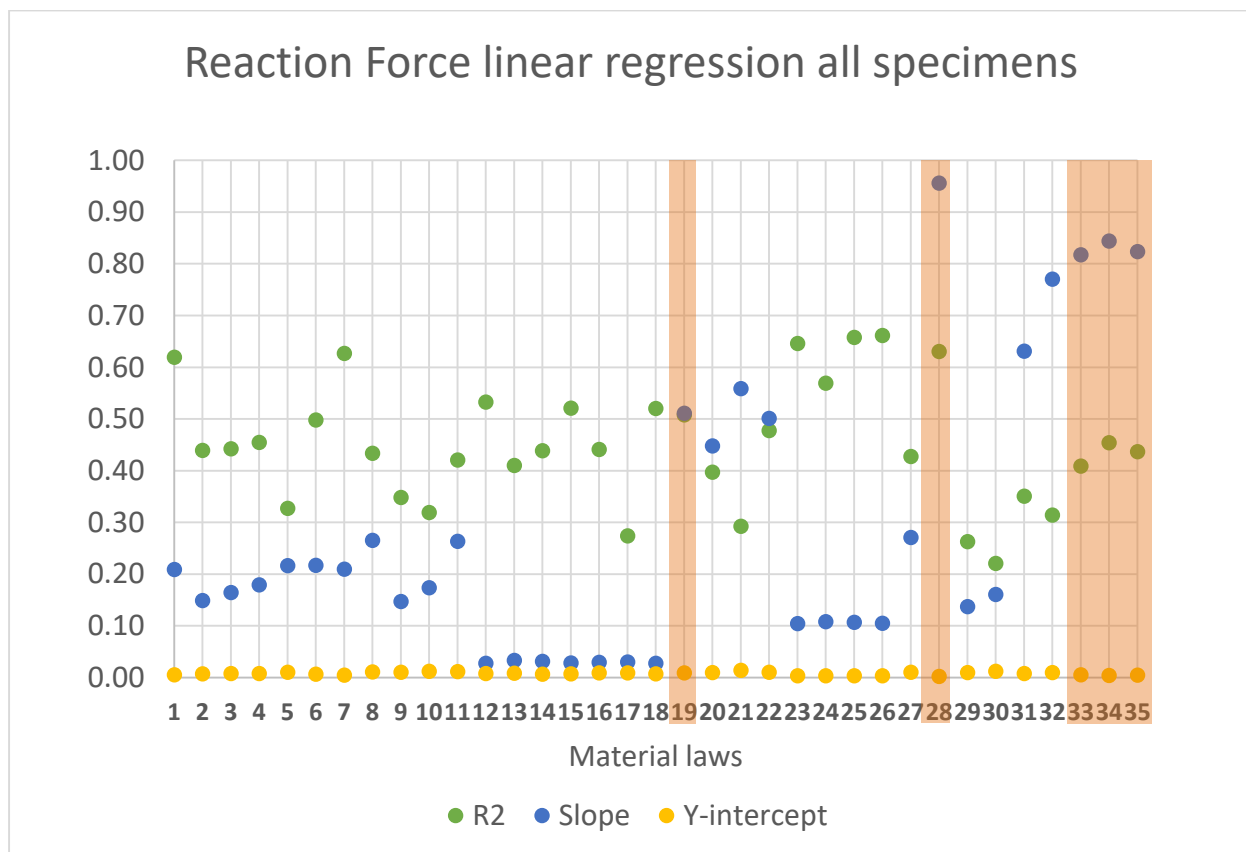
Figure 3:3 High variation in reaction force linear regression for all specimens pooled and for all material laws. Best agreement found for material laws L19, L28, L33-L35, in red.

3.4.4   Material law

For displacements, L32 provided the highest correlation for each specimen separately, but L19, L28, and L33-L35 presented extremely similar results, with differences lower than 1 µm (Section 3.6.1, Tables A1 to A3).

For minimum principal strain, L19, L28, L33-L35 presented very similar, but weak correlation for pooled specimens. When each specimen was investigated separately, S1, S3 and S4 presented a clear advantage for L33-L35, while specimen S5 had better results with L19. Specimen S4 did not show any clear tendency (Supplementary Material section 3.5.2, Tables 3:12 to 3:14).

For reaction force, L19, L28, L33-L35 (red in Figure 3:3) presented the best correlation (R^2 between 0.41 – 0.63 and slope between 0.51 – 0.95). Particularly L28 presented the closest correlation to DVC (R^2 = 0.63, A = 0.96, B = 0.00) and scored the lowest errors (RMSE = 0.52 N and MaxError = 8.60 N).

From these results, L28 was the optimal material law to predict DVC measurements of displacement (Figure 3:4) with FE model. For illustration, we present displacement (Figure 3:5) and minimum principal strain (Figure 3:6) of the five specimens with L28.
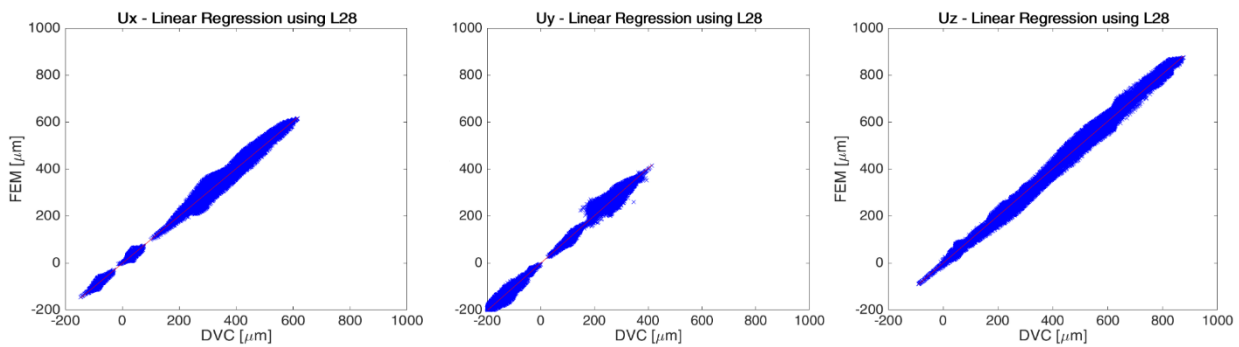
Figure 3:4 Linear regression for displacement along the three directions using material law L28 for all specimens pooled.

DVC

	Ux				Uy				Uz			
	R^2	A	B	RMSE	R^2	A	B	RMSE	R^2	A	B	RMSE
L28	1.00	1.01	-1.74	12.18	1.00	1.01	-1.90	10.44	1.00	1.01	-0.41	11.74
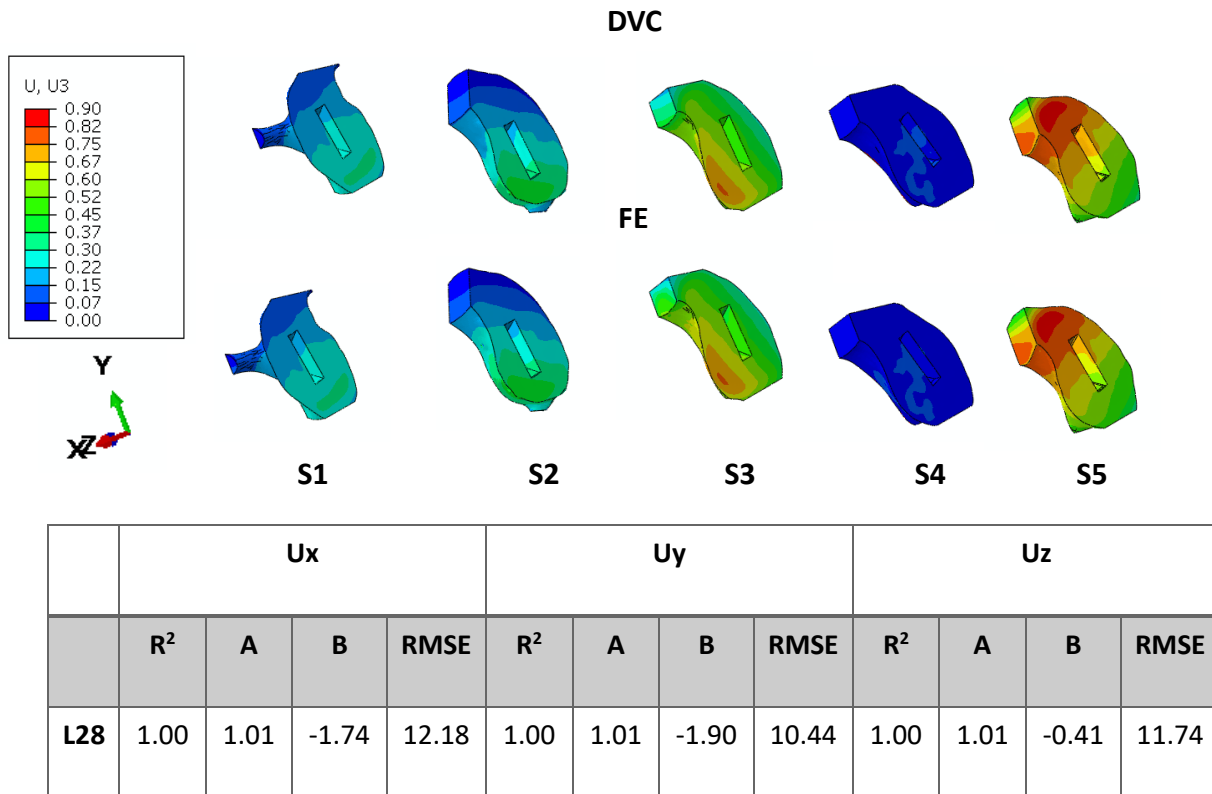
Figure 3:5 Displacement from DVC (top) vs. FE model-predicted displacement using material law L28 (bottom) for specimens S1 to S5 (from left to right) and linear regression results for all specimens pooled.

DVC

	R^2	A	B	RMSE
L28	0.29	0.52	-0.01	7598.72
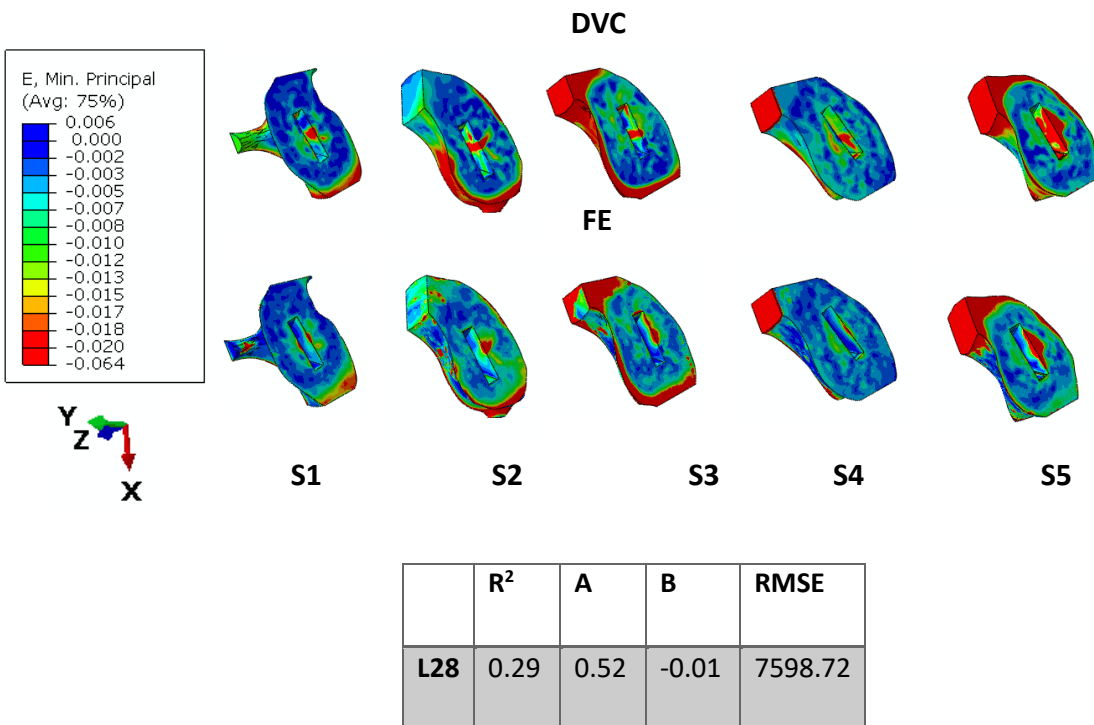
Figure 3:6: DVC minimum principal strain (top) vs. FE model-predicted minimum principal strain using material law L28 (bottom) for specimens S1 to S5 (from left to right) and linear regression results for all specimens pooled.

3.5   Discussion

The goal of the present study was to evaluate the accuracy of displacement, compressive strain and reaction force predictions of CT-derived specimen-specific FE models compared to DVC measurements. An excellent agreement was found for displacement in all three directions. The displacements were in general not very sensitive to the change in material law. The correlation was poor to moderate for strain.

One recently published study on loaded scapulae also found an excellent correlation between experimental displacements (calculated by DVC) and QCT-derived specimen-specific FE model when boundary conditions of the experiment were replicated. Findings were: R^2 = 0.83-1.00, A = 0.93-1.05 and B = -0.02 – 0.01 for concentrated load at 500 N and R^2 = 0.79 – 1.00, A = 0.87 – 1.09 and B = -0.03 to 0.03 for off-axis load [73]. The published study used material law L33 with transition between trabecular and cortical bone of $\rho_{app} = 1.54\ g/cm^3$. This corresponds to material laws L33 ($\rho_{app} = 1.00\ g/cm^3$) and L34 ($\rho_{app} = 1.8\ g/cm^3$) in our study; both of which scored similar results: R^2=0.72-0.99, A = 0.81-1.03 and B = (-12.06 – 32.91 µm). Previous studies used commonly $\rho_{app} = 1.00\ g/cm^3$ and $\rho_{app} = 1.8\ g/cm^3$ as trabecular to cortical transition density [76]. In our case, the intermediate value $\rho_{app} = 1.2\ g/cm^3$ was added because specimens S3 to S5 exhibited this transition density.

Poor correlation was found for minimum principal strain predicted by the model for all specimens pooled: R^2 = 0.28 – 0.37 and A = 0.51 – 0.70. Specimen S2 presented the weakest agreement for all material laws investigated: R^2 = 0.07 – 0.14 and A = 0.31 – 0.53. Compared to published data, these correlations are indeed weak: One recently published study on humeral head osteotomies under loading investigated tensile and compressive strain and found a very good agreement between experiment and derived FE model R^2 = 0.80 and A = 0.83 across 6 specimens; while another most recent study published linear regression results of compressive strain of scapulae under loading with R^2 ranging between 0.73 – 0.75 and a slope ranging between 0.54 – 0.59 [77]. One published study hinted at the higher uncertainty of strain predictions [73].

Specimens S3 to S5 presented a better correlation with respect to minimum principal strain when using relationships L23-L26 compared to material laws L19, L28, L33-L35 while the opposite was observed for specimens S1 and S2. This is probably due to the difference in relative density: S3 to S5 had a relatively lower mean density and thus the deformation was probably more exaggerated using the L19, L28, L33-L35 group.

In general, the poor agreement of strain hints that the DVC technique used was not accurate enough for investigating strain at an applied loading of 750 N and needs in any case further investigation.

Across all material laws investigated, L19, L28 and L33-L35 presented the best agreement with respect to reaction force replication. These material laws (except L19) all use Rice [123] as trabecular bone material law

with different trabecular to cortical bone transitions but they usually provide less stiff models than the L24-L26 group. Relationship L19, although developed on patellar bone, also provides a relatively soft trabecular bone which explains the similar behavior. Two studies on scapulae also used Rice as trabecular bone material law [69,73] with different trabecular-cortical bone transition, both of which were included in our study (L33 to L35).

One study on loaded cadaveric scapulae investigated reaction force errors predicted by QCT-FE models of specimens and found the lowest errors when using Rice as trabecular bone material law (L13-L15 in [76]). This study claimed that the best trabecular to cortical bone transition was $\rho_{app} = 1.00 \ g/cm^3$ when investigating reaction force. This was not confirmed in our study which showed that the best correlation was obtained by either using $\rho_{app} = 1.8 \ g/cm^3$ or by extrapolating the trabecular material law to the cortical bone (Table 3:17 in supplementary material section 3.6.3). This difference in findings between the studies is probably due to lower average density of the specimens in the present study. Minimum principal strain and displacement showed only a rather negligible influence of the trabecular transition level and were more impacted when the power law was changed (Table 3:6 to Table 3:11 in the supplementary material 3.6.1 and 3.6.2).

Similar to the previous study, displacements were quite robust to change in material law while reaction forces presented more variation. Variation in minimum principal strain was also observed in our case. This may support the theory that micro-architecture may be the reason for these variations [76,134]. Thus, more FE models investigating sensitivity of compressive strains to different material laws are needed to confirm the tendency. Bone mesh size was assigned to 1.5 mm, to be consistent with the DVC nodal spacing of 1.4 mm and after mesh convergence study where maximum displacement, average axial strain and minimum principal strain were investigated for bone mesh sizes 0.5, 1, 1.5, 2 and 3. The mesh convergence study was performed in the context of the previously published work [135]. Moreover, the area around the implant was chosen because our interest lies in the bone behavior around the implant.

This study has a number of limitations. First the number of specimens used is too small for any conclusive and especially any strong statistical analysis. Second, the model introduces several simplifications: bone was segmented from the CT data and not the µCT data. Second, µCT data and CT-data were rigidly registered, which may introduce a slight difference in positioning. Third, the implant was positioned using µCT data and virtual implantation was performed. All these steps may have introduced cumulative errors. Moreover, the 0.5 mm thick cement is idealized while in reality, the hot cement diffused into the trabecular bone and destroyed some trabeculae. Also, and as stated previously [76,136], material mapping from density may introduce some errors in density quantification, especially that assumptions were introduced with equations (2) and (3). Partial volume effect was clearly present as shown in Figure 3:6 where the outer contour of the

surface was clearly assigned lower density modulus than in reality, thus contributing to reduce agreement between DVC and FE model.

Lastly, this study used boundary conditions from the experiment, which is a strength since most validation studies are limited by the lack of correct boundary conditions and using them has shown a great improvement in experiment-model correspondence [73,76,77,90,133,134,137,138]. However, using boundary conditions from the experiment may be considered as a limitation to the applicability in vivo since the boundary conditions for each patient cannot be replicated to the FE model.

Nonetheless, the present study is among the first ones to present a CT to FE workflow which compares DVC versus FE model-predicted displacement, minimum principal strain and reaction force results on loaded cadaveric specimens. This study is the first one to present strain validation data from DVC measurements on implanted cadaveric scapulae.

To conclude, this study presents specimen-specific CT-derived FE model that very well replicated displacements measured experimentally. The best suited ρ-E relationship was $E = 60 + 900 * \rho_{app}^2$ [123] at the most suitable transition depending on the average density of the specimens. The workflow presented may be extended for patient-specific FE model generation in the context of implant design comparison. However compressive strain results need to be handled with caution.

3.6   Supplementary Material

3.6.1   Displacement

R^2			Ux					Uy					Uz		
ρ-E	S1	S2	S3	S4	S5	S1	S2	S3	S4	S5	S1	S2	S3	S4	S5
L1	0.77	0.97	0.97	0.71	0.91	0.91	0.89	0.92	0.78	0.91	0.98	0.99	0.98	0.79	0.99
L2	0.76	0.96	0.97	0.71	0.91	0.90	0.88	0.92	0.78	0.91	0.98	0.99	0.98	0.79	0.99
L3	0.76	0.97	0.97	0.71	0.91	0.90	0.89	0.92	0.78	0.91	0.98	0.99	0.98	0.79	0.99
L4	0.76	0.97	0.97	0.71	0.91	0.90	0.89	0.92	0.78	0.91	0.98	0.99	0.98	0.79	0.99
L5	0.79	0.97	0.97	0.71	0.92	0.91	0.91	0.92	0.78	0.91	0.98	0.99	0.98	0.79	0.99
L6	0.78	0.97	0.97	0.71	0.91	0.91	0.90	0.92	0.78	0.91	0.98	0.99	0.98	0.79	0.99
L7	0.77	0.97	0.97	0.71	0.91	0.91	0.89	0.92	0.78	0.91	0.98	0.99	0.98	0.79	0.99
L8	0.72	0.96	0.97	0.70	0.89	0.89	0.87	0.91	0.77	0.91	0.98	0.99	0.98	0.80	0.99
L9	0.71	0.95	0.97	0.70	0.89	0.89	0.84	0.91	0.77	0.92	0.98	0.99	0.98	0.80	0.99
L10	0.72	0.96	0.97	0.70	0.89	0.89	0.86	0.91	0.77	0.91	0.98	0.99	0.98	0.80	0.99
L11	0.72	0.96	0.97	0.70	0.89	0.89	0.87	0.91	0.77	0.91	0.98	0.99	0.98	0.80	0.99
L12	0.75	0.97	0.97	0.70	0.90	0.90	0.89	0.91	0.76	0.91	0.98	0.99	0.98	0.76	0.99
L13	0.77	0.97	0.97	0.71	0.90	0.90	0.91	0.91	0.77	0.91	0.98	0.99	0.98	0.76	0.99
L14	0.76	0.97	0.97	0.70	0.90	0.90	0.89	0.91	0.76	0.91	0.98	0.99	0.98	0.76	0.99
L15	0.75	0.97	0.97	0.70	0.90	0.90	0.89	0.91	0.76	0.91	0.98	0.99	0.98	0.76	0.99
L16	0.79	0.97	0.97	0.71	0.91	0.91	0.91	0.91	0.77	0.91	0.98	0.99	0.98	0.76	0.99
L17	0.77	0.97	0.97	0.70	0.90	0.90	0.90	0.91	0.76	0.91	0.98	0.99	0.98	0.76	0.99
L18	0.75	0.97	0.97	0.70	0.90	0.90	0.89	0.91	0.76	0.91	0.98	0.99	0.98	0.76	0.99
L19	0.72	0.96	0.96	0.70	0.88	0.89	0.86	0.89	0.75	0.91	0.98	0.99	0.98	0.79	0.99
L20	0.72	0.96	0.96	0.70	0.88	0.89	0.86	0.89	0.75	0.91	0.98	0.99	0.98	0.79	0.99
L21	0.72	0.96	0.96	0.70	0.88	0.89	0.86	0.89	0.75	0.91	0.98	0.99	0.98	0.79	0.99
L22	0.77	0.97	0.98	0.71	0.91	0.91	0.90	0.92	0.78	0.91	0.98	0.99	0.98	0.78	0.99
L23	0.78	0.97	0.98	0.71	0.91	0.91	0.90	0.92	0.78	0.91	0.98	0.99	0.98	0.78	0.99
L24	0.77	0.97	0.98	0.71	0.91	0.91	0.90	0.92	0.78	0.91	0.98	0.99	0.98	0.78	0.99
L25	0.77	0.97	0.98	0.71	0.91	0.91	0.90	0.92	0.78	0.91	0.98	0.99	0.98	0.78	0.99
L26	0.72	0.96	0.97	0.70	0.89	0.89	0.87	0.91	0.77	0.91	0.98	0.99	0.98	0.80	0.99
L27	0.78	0.96	0.98	0.72	0.91	0.91	0.90	0.93	0.80	0.88	0.98	0.99	0.98	0.82	0.99
L28	0.74	0.95	0.98	0.72	0.90	0.90	0.84	0.93	0.80	0.88	0.98	0.99	0.98	0.82	0.99
L29	0.76	0.96	0.98	0.72	0.91	0.91	0.88	0.93	0.80	0.88	0.98	0.99	0.98	0.82	0.99
L30	0.76	0.96	0.98	0.72	0.91	0.91	0.88	0.93	0.80	0.88	0.98	0.99	0.98	0.82	0.99
L31	0.78	0.96	0.98	0.72	0.91	0.91	0.90	0.93	0.80	0.88	0.98	0.99	0.98	0.82	0.99
L32	0.79	0.97	0.98	0.72	0.92	0.91	0.91	0.93	0.80	0.88	0.98	0.99	0.98	0.82	0.99
L33	0.78	0.96	0.98	0.72	0.92	0.91	0.90	0.93	0.80	0.88	0.98	0.99	0.98	0.82	0.99
L34	0.78	0.96	0.98	0.72	0.91	0.91	0.90	0.93	0.80	0.88	0.98	0.99	0.98	0.82	0.99
L35	0.78	0.96	0.98	0.72	0.91	0.91	0.90	0.93	0.80	0.88	0.98	0.99	0.98	0.82	0.99

Table 3:6 Coefficient of determination (R^2) for displacement in three directions for each specimen across all material laws.

Slope	Ux					Uy					Uz				
ρ-E	S1	S2	S3	S4	S5	S1	S2	S3	S4	S5	S1	S2	S3	S4	S5
L1	0.91	0.96	1.02	0.79	1.00	0.95	0.97	0.98	0.82	0.94	1.00	0.98	1.03	0.92	1.00
L2	0.90	0.96	1.02	0.79	1.00	0.95	0.95	0.98	0.82	0.94	1.00	0.98	1.03	0.92	1.00
L3	0.91	0.96	1.02	0.79	1.00	0.95	0.96	0.98	0.82	0.94	1.00	0.98	1.03	0.92	1.00
L4	0.91	0.96	1.02	0.79	1.00	0.95	0.97	0.98	0.82	0.94	1.00	0.98	1.03	0.92	1.00
L5	0.95	0.97	1.02	0.80	1.01	0.96	1.01	0.98	0.83	0.93	1.00	0.98	1.04	0.92	1.00
L6	0.93	0.96	1.02	0.79	1.00	0.96	0.98	0.98	0.82	0.94	1.00	0.98	1.04	0.92	1.00
L7	0.91	0.96	1.02	0.79	1.00	0.96	0.97	0.98	0.82	0.94	1.00	0.98	1.03	0.92	1.00
L8	0.84	0.96	1.01	0.78	0.98	0.95	0.93	0.97	0.80	0.94	1.00	0.98	1.03	0.91	1.00
L9	0.82	0.95	1.01	0.78	0.98	0.94	0.87	0.97	0.80	0.93	1.00	0.98	1.03	0.91	1.00
L10	0.83	0.96	1.01	0.78	0.98	0.94	0.92	0.97	0.80	0.94	1.00	0.98	1.03	0.91	1.00
L11	0.84	0.96	1.01	0.78	0.98	0.95	0.93	0.97	0.80	0.94	1.00	0.98	1.03	0.91	1.00
L12	0.89	0.96	1.02	0.79	1.00	0.95	0.94	0.97	0.80	0.94	1.00	0.98	1.04	0.90	1.00
L13	0.92	0.97	1.02	0.79	1.00	0.96	0.99	0.97	0.81	0.94	1.01	0.98	1.04	0.90	1.00
L14	0.90	0.96	1.02	0.79	1.00	0.96	0.96	0.97	0.80	0.94	1.01	0.98	1.04	0.90	1.00
L15	0.89	0.96	1.02	0.79	1.00	0.95	0.94	0.97	0.80	0.94	1.00	0.98	1.03	0.90	1.00
L16	0.94	0.96	1.01	0.79	1.00	0.96	0.99	0.97	0.81	0.94	1.01	0.99	1.04	0.90	1.00
L17	0.91	0.96	1.02	0.79	0.99	0.96	0.96	0.97	0.81	0.94	1.00	0.98	1.04	0.90	1.00
L18	0.89	0.96	1.02	0.79	0.99	0.96	0.94	0.97	0.80	0.94	1.00	0.98	1.03	0.90	1.00
L19	0.83	0.96	1.01	0.78	0.97	0.94	0.94	0.96	0.78	0.93	1.00	0.97	1.03	0.90	1.00
L20	0.83	0.96	1.01	0.78	0.97	0.94	0.94	0.96	0.78	0.93	1.00	0.97	1.03	0.90	1.00
L21	0.83	0.96	1.01	0.78	0.97	0.94	0.94	0.96	0.78	0.93	1.00	0.97	1.03	0.90	1.00
L22	0.93	0.96	1.02	0.79	1.01	0.95	0.97	0.98	0.82	0.94	1.00	0.98	1.04	0.92	1.00
L23	0.93	0.96	1.02	0.80	1.01	0.96	0.98	0.98	0.82	0.94	1.00	0.98	1.04	0.92	1.00
L24	0.93	0.96	1.02	0.80	1.01	0.96	0.97	0.98	0.82	0.94	1.00	0.98	1.04	0.92	1.00
L25	0.93	0.96	1.02	0.79	1.01	0.96	0.97	0.98	0.82	0.94	1.00	0.98	1.04	0.92	1.00
L26	0.84	0.96	1.01	0.78	0.98	0.95	0.93	0.97	0.80	0.94	1.00	0.98	1.03	0.91	1.00
L27	0.94	0.96	1.02	0.81	1.02	0.96	0.99	0.99	0.85	0.91	1.00	0.98	1.03	0.94	1.01
L28	0.89	0.95	1.02	0.80	1.01	0.94	0.87	0.99	0.84	0.91	1.00	0.98	1.03	0.94	1.01
L29	0.92	0.96	1.02	0.81	1.01	0.95	0.97	0.99	0.85	0.91	1.00	0.98	1.03	0.94	1.01
L30	0.92	0.96	1.02	0.81	1.01	0.95	0.97	0.99	0.85	0.91	1.00	0.98	1.03	0.94	1.01
L31	0.94	0.96	1.02	0.81	1.02	0.95	0.99	0.99	0.85	0.91	1.00	0.98	1.03	0.94	1.01
L32	0.97	0.96	1.02	0.81	1.02	0.95	1.02	1.00	0.86	0.91	1.00	0.98	1.03	0.94	1.00
L33	0.95	0.96	1.02	0.81	1.02	0.95	1.00	0.99	0.85	0.91	1.00	0.98	1.03	0.94	1.01
L34	0.94	0.96	1.02	0.81	1.02	0.95	0.99	0.99	0.85	0.91	1.00	0.98	1.03	0.94	1.01
L35	0.94	0.96	1.02	0.81	1.02	0.95	1.00	0.99	0.85	0.91	1.00	0.98	1.03	0.94	1.01

Table 3:7 Slope of linear regression for displacement in three directions for each specimen across all material laws.

y-intercept	Ux					Uy					Uz				
ρ-E	S1	S2	S3	S4	S5	S1	S2	S3	S4	S5	S1	S2	S3	S4	S5
L1	-8.67	11.84	-1.02	5.47	0.97	-6.81	-0.52	-7.84	-5.49	23.00	3.07	1.07	-11.72	8.40	3.64
L2	-9.83	13.36	-1.02	5.48	1.43	-7.62	1.58	-7.96	-5.61	22.52	3.18	1.12	-11.64	8.42	3.49
L3	-9.24	12.22	-0.96	5.47	1.02	-7.37	-0.05	-7.84	-5.53	22.81	3.14	1.14	-11.68	8.40	3.59
L4	-8.99	11.91	-0.97	5.47	0.93	-7.17	-0.47	-7.83	-5.51	22.91	3.11	1.09	-11.70	8.40	3.62
L5	-4.86	7.46	-0.70	5.44	0.35	-5.22	-2.92	-7.55	-5.15	24.83	2.71	0.22	-12.26	8.33	4.97
L6	-7.07	10.55	-1.11	5.45	1.02	-5.80	-1.57	-7.85	-5.34	23.58	2.89	0.82	-11.90	8.42	4.03
L7	-8.61	11.84	-1.02	5.47	1.02	-6.65	-0.52	-7.84	-5.49	23.00	3.09	1.07	-11.72	8.40	3.63
L8	-15.24	14.99	-0.46	5.93	5.47	-9.61	3.52	-9.30	-6.31	22.46	2.92	1.98	-10.44	8.67	3.40
L9	-17.10	17.84	-0.47	5.97	6.62	-10.60	9.11	-9.59	-6.52	22.28	3.07	1.92	-10.37	8.69	3.26
L10	-15.93	15.41	-0.35	5.94	5.63	-10.16	4.55	-9.30	-6.40	22.32	2.97	2.06	-10.41	8.67	3.34
L11	-15.31	14.99	-0.46	5.93	5.44	-9.70	3.52	-9.30	-6.31	22.47	2.93	1.98	-10.45	8.67	3.40
L12	-10.71	13.95	-0.16	5.66	2.60	-7.86	1.89	-9.80	-6.38	21.20	2.99	1.35	-11.22	9.58	4.96
L13	-7.75	10.38	-0.13	5.63	2.05	-5.64	-1.92	-9.56	-6.08	22.20	2.69	0.89	-11.53	9.54	5.63
L14	-9.24	13.03	-0.33	5.66	2.87	-6.28	0.81	-9.81	-6.24	21.56	2.84	1.15	-11.33	9.60	5.20
L15	-10.52	13.95	-0.16	5.66	2.80	-7.26	1.90	-9.80	-6.38	21.16	3.06	1.35	-11.22	9.58	4.96
L16	-5.83	9.35	0.12	5.64	2.51	-4.83	-0.95	-9.51	-5.92	22.95	2.75	0.34	-11.93	9.55	6.67
L17	-8.63	12.36	-0.34	5.66	3.49	-5.57	0.59	-9.83	-6.14	21.74	2.91	1.01	-11.47	9.64	5.54
L18	-10.48	13.95	-0.16	5.66	2.89	-7.05	1.90	-9.80	-6.38	21.14	3.10	1.35	-11.22	9.58	4.96
L19	-15.85	15.56	2.13	6.23	9.08	-9.83	1.94	-11.60	-6.95	23.53	3.57	3.10	-11.65	9.46	5.31
L20	-16.11	15.56	2.13	6.23	8.96	-10.32	1.94	-11.60	-6.95	23.53	3.58	3.10	-11.65	9.46	5.31
L21	-15.88	15.56	2.13	6.23	9.06	-9.94	1.94	-11.60	-6.95	23.53	3.56	3.10	-11.65	9.46	5.31
L22	-7.34	11.63	-0.92	5.38	-0.01	-6.42	-0.63	-7.68	-5.38	22.96	3.07	0.76	-11.93	8.57	3.93
L23	-6.91	11.06	-0.90	5.38	-0.16	-6.20	-1.26	-7.64	-5.35	23.14	3.03	0.73	-11.96	8.56	4.03
L24	-7.17	11.51	-0.93	5.38	-0.05	-6.28	-0.77	-7.69	-5.37	23.02	3.05	0.74	-11.94	8.57	3.96
L25	-7.33	11.63	-0.92	5.38	-0.01	-6.38	-0.63	-7.68	-5.38	22.97	3.07	0.76	-11.93	8.57	3.94
L26	-15.19	14.99	-0.46	5.93	5.48	-9.53	3.52	-9.30	-6.31	22.46	2.93	1.98	-10.44	8.67	3.40
L27	-5.98	9.86	-1.19	5.26	-2.33	-5.89	-3.10	-5.06	-4.25	32.75	3.05	0.30	-11.98	6.82	1.92
L28	-11.41	17.75	-1.22	5.31	0.43	-9.46	9.04	-5.61	-4.69	31.19	3.35	0.11	-11.72	6.89	1.23
L29	-8.55	11.71	-0.96	5.25	-1.74	-8.15	-0.58	-5.06	-4.43	31.97	3.25	0.49	-11.85	6.82	1.69
L30	-8.55	11.71	-0.96	5.25	-1.74	-8.15	-0.58	-5.06	-4.43	31.97	3.25	0.49	-11.85	6.82	1.69
L31	-6.42	9.86	-1.19	5.26	-2.43	-6.75	-3.11	-5.06	-4.25	32.73	3.06	0.30	-11.98	6.82	1.91
L32	-4.06	6.47	-0.90	5.25	-3.23	-5.80	-5.32	-4.81	-4.04	33.89	2.88	-0.15	-12.33	6.73	2.65
L33	-5.61	9.13	-1.20	5.26	-2.63	-6.18	-3.70	-5.06	-4.19	32.99	3.01	0.19	-12.06	6.82	2.06
L34	-6.22	9.86	-1.19	5.26	-2.39	-6.37	-3.10	-5.06	-4.25	32.74	3.04	0.30	-11.98	6.82	1.93
L35	-6.13	9.78	-1.21	5.26	-2.46	-6.43	-3.16	-5.06	-4.23	32.80	3.05	0.28	-11.99	6.82	1.96

Table 3:8 y-intercept of linear regression for displacement in three directions for each specimen across all material laws.

RMSE			Ux					Uy					Uz		
ρ-E	S1	S2	S3	S4	S5	S1	S2	S3	S4	S5	S1	S2	S3	S4	S5
L1	6.85	11.41	12.61	6.10	14.55	7.93	6.58	9.86	3.94	11.92	8.10	11.12	13.99	7.80	12.34
L2	6.97	11.88	12.59	6.11	14.72	7.99	6.87	9.86	3.95	11.88	8.09	11.27	13.98	7.80	12.36
L3	6.90	11.54	12.61	6.10	14.59	7.97	6.68	9.86	3.94	11.91	8.09	11.18	13.99	7.79	12.35
L4	6.87	11.43	12.61	6.10	14.54	7.96	6.58	9.86	3.94	11.92	8.09	11.13	13.99	7.79	12.35
L5	6.47	10.70	12.65	6.08	14.03	7.88	6.02	9.89	3.93	12.13	8.16	10.14	14.10	7.79	12.30
L6	6.68	10.93	12.61	6.10	14.46	7.87	6.25	9.86	3.94	11.95	8.14	10.86	14.01	7.80	12.32
L7	6.85	11.41	12.61	6.10	14.56	7.91	6.58	9.86	3.94	11.92	8.10	11.12	13.99	7.80	12.34
L8	7.39	12.55	13.08	6.20	15.80	8.49	7.37	10.41	4.00	11.64	8.23	11.74	13.97	7.46	12.29
L9	7.58	13.35	13.04	6.22	16.20	8.63	8.06	10.42	4.01	11.62	8.18	11.96	13.95	7.47	12.30
L10	7.46	12.66	13.07	6.21	15.88	8.55	7.56	10.41	4.00	11.65	8.21	11.81	13.96	7.46	12.30
L11	7.39	12.55	13.08	6.20	15.79	8.50	7.37	10.41	4.00	11.64	8.23	11.74	13.97	7.46	12.29
L12	7.02	11.55	13.09	6.20	15.43	8.11	6.84	10.52	4.09	11.73	8.25	11.40	14.39	8.26	12.97
L13	6.75	10.44	13.13	6.18	15.05	7.95	6.18	10.53	4.07	11.81	8.31	10.81	14.44	8.25	12.90
L14	6.90	11.16	13.09	6.19	15.40	8.00	6.55	10.52	4.09	11.71	8.28	11.21	14.40	8.26	12.92
L15	7.04	11.55	13.09	6.20	15.47	8.06	6.84	10.52	4.09	11.72	8.24	11.40	14.39	8.26	12.96
L16	6.54	10.74	13.14	6.17	14.92	7.92	6.20	10.55	4.07	11.94	8.33	10.26	14.52	8.25	12.85
L17	6.84	10.88	13.09	6.19	15.48	7.95	6.39	10.52	4.09	11.76	8.31	11.06	14.41	8.26	12.88
L18	7.04	11.55	13.09	6.20	15.49	8.05	6.84	10.52	4.09	11.71	8.24	11.40	14.39	8.26	12.95
L19	7.44	12.52	15.68	6.20	16.95	8.66	7.48	11.31	4.16	12.31	8.41	11.96	14.63	7.63	12.96
L20	7.44	12.52	15.68	6.20	16.92	8.70	7.48	11.31	4.16	12.31	8.41	11.96	14.63	7.63	12.96
L21	7.44	12.52	15.68	6.20	16.95	8.67	7.48	11.31	4.16	12.31	8.41	11.96	14.63	7.63	12.96
L22	6.74	11.22	12.40	6.12	14.32	7.86	6.47	9.77	3.95	11.86	8.08	11.04	13.98	8.03	12.44
L23	6.70	11.06	12.40	6.11	14.24	7.84	6.38	9.77	3.95	11.87	8.08	10.96	13.99	8.03	12.43
L24	6.72	11.18	12.40	6.12	14.30	7.85	6.44	9.77	3.95	11.86	8.08	11.01	13.99	8.03	12.43
L25	6.74	11.22	12.40	6.12	14.32	7.85	6.47	9.77	3.95	11.86	8.08	11.04	13.98	8.03	12.43
L26	7.39	12.55	13.08	6.20	15.80	8.49	7.37	10.41	4.00	11.64	8.23	11.74	13.97	7.46	12.28
L27	6.68	12.01	11.46	6.04	14.38	7.78	6.58	9.41	3.77	13.95	7.85	10.98	13.25	7.16	12.24
L28	7.22	13.87	11.40	6.07	15.22	8.05	8.06	9.42	3.81	13.92	7.74	11.45	13.20	7.18	12.37
L29	6.93	12.48	11.45	6.05	14.60	7.90	7.05	9.41	3.78	14.01	7.80	11.19	13.24	7.17	12.31
L30	6.93	12.48	11.45	6.05	14.60	7.90	7.05	9.41	3.78	14.01	7.80	11.19	13.24	7.17	12.31
L31	6.67	12.01	11.46	6.04	14.36	7.85	6.58	9.41	3.77	13.96	7.85	10.98	13.25	7.16	12.25
L32	6.45	11.47	11.48	6.03	14.01	7.86	6.22	9.43	3.76	14.04	7.88	10.44	13.32	7.15	12.20
L33	6.59	11.78	11.46	6.03	14.29	7.83	6.42	9.41	3.77	13.94	7.87	10.86	13.26	7.16	12.23
L34	6.67	12.01	11.46	6.04	14.37	7.82	6.58	9.41	3.77	13.95	7.86	10.98	13.25	7.16	12.25
L35	6.65	11.98	11.46	6.04	14.35	7.82	6.56	9.41	3.77	13.95	7.86	10.96	13.25	7.16	12.24

Table 3:9 RMSE of linear regression for displacement in three directions for each specimen across all material laws.

MaxError	Ux					Uy					Uz				
ρ-E	S1	S2	S3	S4	S5	S1	S2	S3	S4	S5	S1	S2	S3	S4	S5
L1	28.26	41.57	59.59	26.44	61.88	31.81	20.52	52.64	14.82	47.86	38.34	32.31	66.30	41.83	62.30
L2	29.11	43.57	59.58	26.44	61.63	32.61	18.85	52.60	14.85	47.38	38.40	33.71	66.30	41.88	62.55
L3	28.45	42.24	59.59	26.45	61.81	32.38	19.80	52.61	14.82	47.77	38.32	32.47	66.30	41.83	62.51
L4	28.45	41.64	59.59	26.44	61.85	32.36	20.47	52.62	14.80	47.81	38.33	32.58	66.30	41.83	62.48
L5	26.24	40.42	59.57	26.43	61.03	30.15	22.02	52.74	14.51	48.94	38.17	34.20	66.30	42.23	62.54
L6	27.73	40.69	59.60	26.41	61.70	30.82	19.62	52.66	14.69	47.81	38.35	38.09	66.30	41.83	62.26
L7	28.20	41.57	59.59	26.44	61.88	31.67	20.52	52.64	14.82	47.87	38.40	32.31	66.30	41.83	61.81
L8	31.74	45.73	62.27	27.53	65.54	34.51	22.28	56.67	15.11	45.82	39.14	33.64	64.48	38.67	62.74
L9	32.94	50.38	62.20	27.83	67.22	34.76	22.33	56.62	15.28	45.33	38.65	38.33	64.48	38.73	62.54
L10	32.20	46.51	62.27	27.55	66.08	34.55	21.09	56.63	15.17	45.68	38.69	34.66	64.48	38.65	62.75
L11	31.89	45.73	62.27	27.53	65.54	34.51	22.28	56.67	15.11	45.82	39.36	33.64	64.48	38.67	62.74
L12	29.28	44.05	62.22	27.45	65.12	32.88	20.80	63.74	15.72	47.26	39.31	32.63	68.52	45.52	64.12
L13	27.76	39.48	62.25	27.28	63.13	30.62	21.22	63.94	15.42	47.91	39.23	32.63	68.52	45.58	64.35
L14	28.66	42.77	62.22	27.44	65.16	31.46	21.17	63.89	15.62	47.38	39.12	34.33	68.52	45.57	64.25
L15	29.03	44.05	62.22	27.45	65.09	32.42	20.80	63.74	15.72	47.29	39.29	32.63	68.52	45.52	64.36
L16	26.79	45.02	62.23	27.28	63.43	30.03	22.35	64.16	15.29	48.31	39.37	40.29	68.96	45.17	64.35
L17	28.30	41.98	62.23	27.43	65.11	31.02	21.39	64.06	15.48	47.56	39.11	41.37	68.52	45.60	64.47
L18	28.96	44.05	62.22	27.45	65.08	32.41	20.80	63.74	15.72	47.30	39.28	32.63	68.52	45.52	64.35
L19	31.78	45.10	74.74	27.90	71.03	33.98	23.04	65.25	15.54	47.56	39.63	32.74	67.94	38.60	66.28
L20	32.00	45.10	74.74	27.90	70.27	34.08	23.04	65.25	15.54	47.54	39.49	32.74	67.94	38.60	66.28
L21	31.90	45.10	74.74	27.90	71.03	33.99	23.04	65.25	15.54	47.55	39.59	32.74	67.94	38.60	66.28
L22	27.90	41.50	58.96	26.96	60.58	31.36	21.12	52.99	14.94	47.67	38.06	32.29	66.57	43.65	61.95
L23	27.36	40.63	58.98	26.96	60.64	31.16	20.46	53.00	14.92	47.76	38.10	31.95	66.57	43.65	62.02
L24	27.84	40.96	58.96	26.96	60.61	31.23	20.07	53.00	14.93	47.71	38.07	32.31	66.57	43.65	62.05
L25	27.88	41.50	58.96	26.96	60.58	31.33	21.12	52.99	14.94	47.67	38.06	32.29	66.57	43.65	61.97
L26	31.65	45.73	62.27	27.53	65.53	34.51	22.28	56.67	15.11	45.83	38.52	33.64	64.48	38.67	62.75
L27	27.49	39.94	54.85	26.58	69.30	30.80	24.24	49.61	13.78	85.08	36.82	32.35	61.68	36.10	67.18
L28	30.97	51.69	54.80	26.57	69.46	33.51	22.39	49.63	14.21	86.27	36.88	41.69	61.31	36.26	67.50
L29	29.25	42.18	54.84	26.60	69.47	32.55	23.57	49.60	13.92	80.69	36.94	34.32	61.68	36.10	66.85
L30	29.25	42.18	54.84	26.60	69.47	32.55	23.57	49.60	13.92	80.69	36.94	34.32	61.68	36.10	66.85
L31	27.77	39.94	54.85	26.58	68.64	31.96	24.24	49.61	13.78	84.70	36.66	32.35	61.68	36.10	66.95
L32	26.47	38.11	54.89	26.45	67.89	31.29	25.24	49.95	13.53	84.92	36.20	32.35	61.68	35.97	66.70
L33	27.26	39.42	54.85	26.57	68.78	31.04	24.53	49.62	13.74	84.68	36.70	33.34	61.68	36.11	67.03
L34	27.57	39.94	54.85	26.58	69.30	31.14	24.24	49.61	13.78	85.09	36.76	32.35	61.68	36.10	67.05
L35	27.62	39.88	54.85	26.57	68.67	31.15	24.24	49.61	13.78	84.24	36.79	32.60	61.68	36.11	67.08

Table 3:10 MaxError of linear regression for displacement in three directions for each specimen across all material laws.

3.6.2 Minimum Principal Strain

	R²	Slope	Y-intercept	RMSE	MaxError
L1	0.36	0.70	0.00	7191.45	89840.00
L2	0.36	0.69	0.00	7199.54	89840.00
L3	0.36	0.70	0.00	7193.79	89840.00
L4	0.36	0.70	0.00	7190.65	89840.00
L5	0.36	0.69	0.00	7212.58	89840.00
L6	0.36	0.70	0.00	7194.37	89840.00
L7	0.36	0.70	0.00	7190.23	89840.00
L8	0.34	0.68	0.00	7270.03	90210.00
L9	0.34	0.67	0.00	7293.89	90210.00
L10	0.34	0.67	0.00	7276.48	90210.00
L11	0.34	0.68	0.00	7270.19	90210.00
L12	0.33	0.61	-0.01	7418.37	90050.00
L13	0.33	0.61	-0.01	7407.54	90050.00
L14	0.33	0.61	-0.01	7418.07	90050.00
L15	0.33	0.61	-0.01	7410.42	90050.00
L16	0.32	0.60	-0.01	7481.65	90050.00
L17	0.33	0.61	-0.01	7418.82	90050.00
L18	0.33	0.61	-0.01	7408.94	90050.00
L19	0.30	0.59	-0.01	7515.05	86770.00
L20	0.30	0.59	-0.01	7516.27	86770.00
L21	0.30	0.60	-0.01	7507.09	86790.00
L22	0.30	0.59	-0.01	7515.14	86770.00
L23	0.37	0.69	0.00	7206.04	89690.00
L24	0.37	0.69	0.00	7203.51	89690.00
L25	0.37	0.69	0.00	7205.26	89690.00
L26	0.37	0.69	0.00	7205.55	89690.00
L27	0.34	0.68	0.00	7269.96	90210.00
L28	0.29	0.52	-0.01	7598.72	90080.00
L29	0.28	0.51	-0.01	7617.63	90080.00
L30	0.28	0.52	-0.01	7601.85	90080.00
L31	0.29	0.52	-0.01	7599.84	90080.00
L32	0.28	0.52	-0.01	7603.31	90080.00
L33	0.29	0.52	-0.01	7599.29	90080.00
L34	0.29	0.52	-0.01	7600.15	90080.00
L35	0.29	0.52	-0.01	7600.61	90080.00
MIN	0.28	0.51	-0.01	7190.23	86770.00
MAX	0.37	0.70	0.0	7617.63	90210.00

Table 3:11 Linear regression for minimum principal strain across all material laws and for all pooled specimens.

			R²		
ρ-E	S1	S2	S3	S4	S5
L1	0.19	0.13	0.36	0.42	0.52
L2	0.19	0.12	0.36	0.42	0.52
L3	0.19	0.13	0.36	0.42	0.52
L4	0.19	0.13	0.36	0.42	0.52
L5	0.19	0.13	0.36	0.42	0.51
L6	0.18	0.13	0.36	0.42	0.52
L7	0.19	0.13	0.36	0.42	0.52
L8	0.17	0.09	0.35	0.41	0.50
L9	0.16	0.08	0.35	0.41	0.50
L10	0.17	0.09	0.35	0.41	0.50
L11	0.17	0.09	0.35	0.41	0.50
L12	0.17	0.12	0.30	0.42	0.49
L13	0.17	0.13	0.30	0.43	0.49
L14	0.16	0.12	0.30	0.43	0.49
L15	0.17	0.12	0.30	0.42	0.49
L16	0.16	0.11	0.30	0.43	0.49
L17	0.16	0.12	0.30	0.43	0.49
L18	0.17	0.12	0.30	0.42	0.49
L19	0.15	0.09	0.28	0.38	0.45
L20	0.15	0.09	0.28	0.38	0.45
L21	0.15	0.09	0.28	0.38	0.45
L22	0.19	0.14	0.35	0.46	0.53
L23	0.19	0.14	0.35	0.46	0.53
L24	0.19	0.14	0.35	0.46	0.53
L25	0.19	0.14	0.35	0.46	0.53
L26	0.17	0.09	0.35	0.41	0.50
L27	0.22	0.09	0.30	0.38	0.35
L28	0.21	0.07	0.30	0.38	0.35
L29	0.22	0.08	0.30	0.38	0.35
L30	0.22	0.08	0.30	0.38	0.35
L31	0.22	0.09	0.30	0.38	0.35
L32	0.23	0.09	0.30	0.38	0.35
L33	0.22	0.09	0.30	0.38	0.35
L34	0.22	0.09	0.30	0.38	0.35
L35	0.22	0.09	0.30	0.38	0.35
MIN	0.15	0.07	0.28	0.38	0.35
MAX	0.23	0.14	0.36	0.46	0.53

Table 3:12 Coefficient of determination (R^2) for minimum principal strain for each specimen across all material laws.

			Slope		
ρ-E	**S1**	**S2**	**S3**	**S4**	**S5**
L1	0.68	0.49	0.62	0.64	0.86
L2	0.67	0.48	0.62	0.64	0.86
L3	0.68	0.49	0.62	0.64	0.86
L4	0.68	0.49	0.62	0.64	0.86
L5	0.67	0.48	0.62	0.65	0.86
L6	0.67	0.51	0.62	0.64	0.86
L7	0.68	0.49	0.62	0.64	0.86
L8	0.60	0.37	0.65	0.68	0.83
L9	0.59	0.34	0.65	0.68	0.83
L10	0.60	0.36	0.65	0.68	0.83
L11	0.60	0.37	0.65	0.68	0.83
L12	0.62	0.46	0.49	0.61	0.82
L13	0.63	0.50	0.49	0.61	0.83
L14	0.62	0.47	0.49	0.61	0.83
L15	0.63	0.46	0.49	0.61	0.82
L16	0.60	0.40	0.49	0.61	0.82
L17	0.61	0.47	0.49	0.61	0.82
L18	0.63	0.46	0.49	0.61	0.82
L19	0.57	0.35	0.51	0.63	0.76
L20	0.57	0.35	0.51	0.63	0.76
L21	0.57	0.35	0.51	0.63	0.76
L22	0.69	0.53	0.59	0.64	0.88
L23	0.70	0.53	0.59	0.64	0.88
L24	0.69	0.53	0.59	0.64	0.88
L25	0.69	0.53	0.59	0.64	0.88
L26	0.60	0.37	0.65	0.68	0.83
L27	0.74	0.34	0.50	0.68	0.53
L28	0.71	0.31	0.50	0.68	0.53
L29	0.73	0.33	0.50	0.68	0.53
L30	0.73	0.33	0.50	0.68	0.53
L31	0.74	0.34	0.50	0.68	0.53
L32	0.74	0.34	0.50	0.68	0.53
L33	0.74	0.34	0.50	0.68	0.53
L34	0.74	0.34	0.50	0.68	0.53
L35	0.74	0.34	0.50	0.68	0.53
MIN	0.57	0.31	0.49	0.61	0.53
MAX	0.74	0.53	0.65	0.68	0.88

Table 3:13 Slope of linear regression for minimum principal strain for each specimen across all material laws.

			y-intercept		
ρ-E	**S1**	**S2**	**S3**	**S4**	**S5**
L1	0.00	-0.01	-0.01	0.00	0.00
L2	0.00	-0.01	-0.01	0.00	0.00
L3	0.00	-0.01	-0.01	0.00	0.00
L4	0.00	-0.01	-0.01	0.00	0.00
L5	0.00	-0.01	-0.01	0.00	0.00
L6	0.00	-0.01	-0.01	0.00	0.00
L7	0.00	-0.01	-0.01	0.00	0.00
L8	0.00	-0.01	0.00	0.00	0.00
L9	0.00	-0.01	0.00	0.00	0.00
L10	0.00	-0.01	0.00	0.00	0.00
L11	0.00	-0.01	0.00	0.00	0.00
L12	0.00	-0.01	-0.01	0.00	0.00
L13	0.00	-0.01	-0.01	0.00	0.00
L14	0.00	-0.01	-0.01	0.00	0.00
L15	0.00	-0.01	-0.01	0.00	0.00
L16	0.00	-0.01	-0.01	0.00	0.00
L17	0.00	-0.01	-0.01	0.00	0.00
L18	0.00	-0.01	-0.01	0.00	0.00
L19	0.00	-0.01	-0.01	0.00	0.00
L20	0.00	-0.01	-0.01	0.00	0.00
L21	0.00	-0.01	-0.01	0.00	0.00
L22	0.00	-0.01	-0.01	0.00	0.00
L23	0.00	-0.01	-0.01	0.00	0.00
L24	0.00	-0.01	-0.01	0.00	0.00
L25	0.00	-0.01	-0.01	0.00	0.00
L26	0.00	-0.01	0.00	0.00	0.00
L27	0.00	-0.01	-0.01	0.00	-0.01
L28	0.00	-0.01	-0.01	0.00	-0.01
L29	0.00	-0.01	-0.01	0.00	-0.01
L30	0.00	-0.01	-0.01	0.00	-0.01
L31	0.00	-0.01	-0.01	0.00	-0.01
L32	0.00	-0.01	-0.01	0.00	-0.01
L33	0.00	-0.01	-0.01	0.00	-0.01
L34	0.00	-0.01	-0.01	0.00	-0.01
L35	0.00	-0.01	-0.01	0.00	-0.01
MIN	0.00	-0.01	-0.01	0.00	-0.01
MAX	0.00	-0.01	0.00	0.00	0.00

Table 3:14 y-intercept of linear regression for minimum principal strain for each specimen across all material laws.

	RMSE				
ρ-E	S1	S2	S3	S4	S5
L1	5335.21	7080.86	8029.81	4236.37	8919.37
L2	5336.46	7104.39	8027.87	4238.80	8915.55
L3	5328.03	7087.94	8029.62	4237.69	8920.54
L4	5323.43	7081.94	8029.46	4237.36	8920.87
L5	5414.73	7087.25	8037.49	4234.99	8936.32
L6	5423.53	7060.89	8029.62	4236.62	8924.82
L7	5324.26	7080.85	8029.79	4236.32	8918.90
L8	5248.38	7237.82	8041.60	4067.57	9071.04
L9	5262.55	7271.49	8040.75	4069.83	9082.11
L10	5243.55	7245.91	8042.11	4069.60	9077.95
L11	5249.22	7237.82	8041.61	4067.63	9071.68
L12	5431.85	7113.12	8389.45	4404.80	9135.39
L13	5481.03	7061.58	8392.88	4401.32	9131.32
L14	5488.88	7095.31	8389.30	4404.61	9130.27
L15	5358.71	7113.13	8389.40	4404.69	9131.76
L16	5655.29	7167.46	8400.43	4402.36	9166.94
L17	5458.38	7097.43	8390.85	4405.27	9143.28
L18	5345.46	7113.16	8389.39	4404.68	9129.96
L19	5310.21	7249.07	8520.22	4113.76	9517.91
L20	5322.25	7249.09	8520.29	4113.55	9518.20
L21	5311.43	7249.07	8520.23	4113.75	9517.64
L22	5317.09	7041.76	8082.82	4418.02	8829.49
L23	5316.58	7032.72	8084.72	4416.49	8828.73
L24	5320.27	7039.08	8082.78	4417.81	8828.18
L25	5314.41	7041.76	8082.81	4418.01	8827.60
L26	5248.60	7237.82	8041.58	4067.57	9070.38
L27	5102.37	7239.78	8381.47	4040.25	10405.77
L28	5123.49	7292.51	8377.79	4039.28	10411.91
L29	5075.40	7253.37	8382.03	4041.17	10410.71
L30	5075.40	7253.37	8382.03	4041.17	10410.71
L31	5113.24	7239.82	8381.58	4040.06	10406.15
L32	5110.15	7230.59	8388.65	4039.40	10420.04
L33	5112.98	7235.03	8381.86	4040.30	10410.53
L34	5109.70	7239.79	8381.53	4040.29	10409.17
L35	5114.68	7239.87	8381.62	4040.48	10407.95
MIN	5075.40	7032.72	8027.87	4039.28	8827.60
MAX	5655.29	7292.51	8520.29	4418.02	10420.04

Table 3:15 RMSE of linear regression for minimum principal strain for each specimen across all material laws.

			MaxError		
ρ-E	S1	S2	S3	S4	S5
L1	60490.00	65500.00	89840.00	46620.00	87760.00
L2	60490.00	65500.00	89840.00	46630.00	87590.00
L3	60230.00	65500.00	89840.00	46630.00	87680.00
L4	59900.00	65500.00	89840.00	46620.00	87720.00
L5	65540.00	65470.00	89840.00	46580.00	88110.00
L6	66730.00	65490.00	89840.00	46620.00	87980.00
L7	59350.00	65500.00	89840.00	46620.00	87770.00
L8	50860.00	65480.00	90210.00	44340.00	86590.00
L9	51420.00	65490.00	90210.00	44360.00	86290.00
L10	50730.00	65480.00	90210.00	44350.00	86480.00
L11	51230.00	65480.00	90210.00	44340.00	86590.00
L12	61580.00	65540.00	90050.00	48260.00	88880.00
L13	64890.00	65530.00	90050.00	48230.00	89130.00
L14	65810.00	65540.00	90050.00	48260.00	89080.00
L15	57760.00	65540.00	90050.00	48260.00	88910.00
L16	74350.00	65510.00	90050.00	48210.00	89250.00
L17	62600.00	65540.00	90050.00	48260.00	89150.00
L18	57290.00	65540.00	90050.00	48260.00	88920.00
L19	52600.00	65790.00	86770.00	44020.00	86400.00
L20	53410.00	65790.00	86770.00	44020.00	86380.00
L21	52870.00	65790.00	86770.00	44020.00	86400.00
L22	60070.00	65480.00	89690.00	47660.00	88410.00
L23	60060.00	65480.00	89690.00	47660.00	88460.00
L24	60080.00	65480.00	89690.00	47660.00	88430.00
L25	59870.00	65480.00	89690.00	47660.00	88410.00
L26	50870.00	65480.00	90210.00	44340.00	86600.00
L27	52180.00	65340.00	90080.00	44900.00	86030.00
L28	51880.00	65380.00	90080.00	44930.00	84600.00
L29	50700.00	65350.00	90080.00	44910.00	85560.00
L30	50700.00	65350.00	90080.00	44910.00	85560.00
L31	52910.00	65340.00	90080.00	44900.00	86010.00
L32	53490.00	65310.00	90080.00	44880.00	86390.00
L33	52870.00	65330.00	90080.00	44900.00	86140.00
L34	52930.00	65340.00	90080.00	44900.00	86020.00
L35	52930.00	65330.00	90080.00	44900.00	86040.00
MIN	50700.00	65310.00	86770.00	44020.00	84600.00
MAX	74350.00	65790.00	90210.00	48260.00	89250.00

Table 3:16 MaxError of linear regression for minimum principal strain for each specimen across all material laws.

3.6.3   Reaction Force

ρ-E	Slope	Y-intercept	R²	RMSE	MaxError
L1	0.21	0.01	0.62	0.55	8.60
L2	0.15	0.01	0.44	0.62	12.24
L3	0.16	0.01	0.44	0.63	12.24
L4	0.18	0.01	0.46	0.63	12.24
L5	0.22	0.01	0.33	0.75	23.13
L6	0.22	0.01	0.50	0.67	20.41
L7	0.21	0.01	0.63	0.54	8.60
L8	0.27	0.01	0.43	0.66	20.54
L9	0.15	0.01	0.35	0.70	17.03
L10	0.17	0.01	0.32	0.70	17.03
L11	0.26	0.01	0.42	0.68	20.54
L12	0.03	0.01	0.53	0.59	11.30
L13	0.03	0.01	0.41	0.71	17.12
L14	0.03	0.01	0.44	0.65	16.62
L15	0.03	0.01	0.52	0.58	10.47
L16	0.03	0.01	0.44	0.65	18.25
L17	0.03	0.01	0.27	0.77	17.04
L18	0.03	0.01	0.52	0.58	10.95
L19	0.51	0.01	0.51	0.61	16.01
L20	0.45	0.01	0.40	0.74	24.90
L21	0.56	0.01	0.29	0.77	24.90
L22	0.50	0.01	0.48	0.67	20.54
L23	0.10	0.00	0.65	0.53	8.60
L24	0.11	0.00	0.57	0.53	8.60
L25	0.11	0.00	0.66	0.52	8.60
L26	0.11	0.00	0.66	0.53	8.60
L27	0.27	0.01	0.43	0.65	20.54
L28	0.96	0.00	0.63	0.52	8.60
L29	0.14	0.01	0.26	0.76	17.03
L30	0.16	0.01	0.22	0.77	17.03
L31	0.63	0.01	0.35	0.77	24.90
L32	0.77	0.01	0.31	0.78	24.90
L33	0.82	0.01	0.41	0.73	24.90
L34	0.84	0.00	0.45	0.71	24.90
L35	0.82	0.00	0.44	0.72	24.90
min	0.03	0.00	0.22	0.52	8.60
max	0.96	0.01	0.66	0.78	24.90

Table 3:17 Linear regression results for reaction force across all material laws and for all specimens pooled.

Chapter 4 Patient-specific musculoskeletal model

The musculoskeletal model described in this chapter was used to estimate patient-specific gleno-humeral joint reaction force, which will be used for the patient-specific FE model presented in chapter 5. The development of the musculoskeletal model presented here as well as its outcome were described in a publication submitted to Source Code for Biology and Medicine journal titled "A Matlab toolbox for scaled-generic modeling of shoulder and elbow". Authors: Sarshari, E; Boulanaache, Y; Terrier, A; Farron, A; Mullhaupt, P and Pioletti, D.
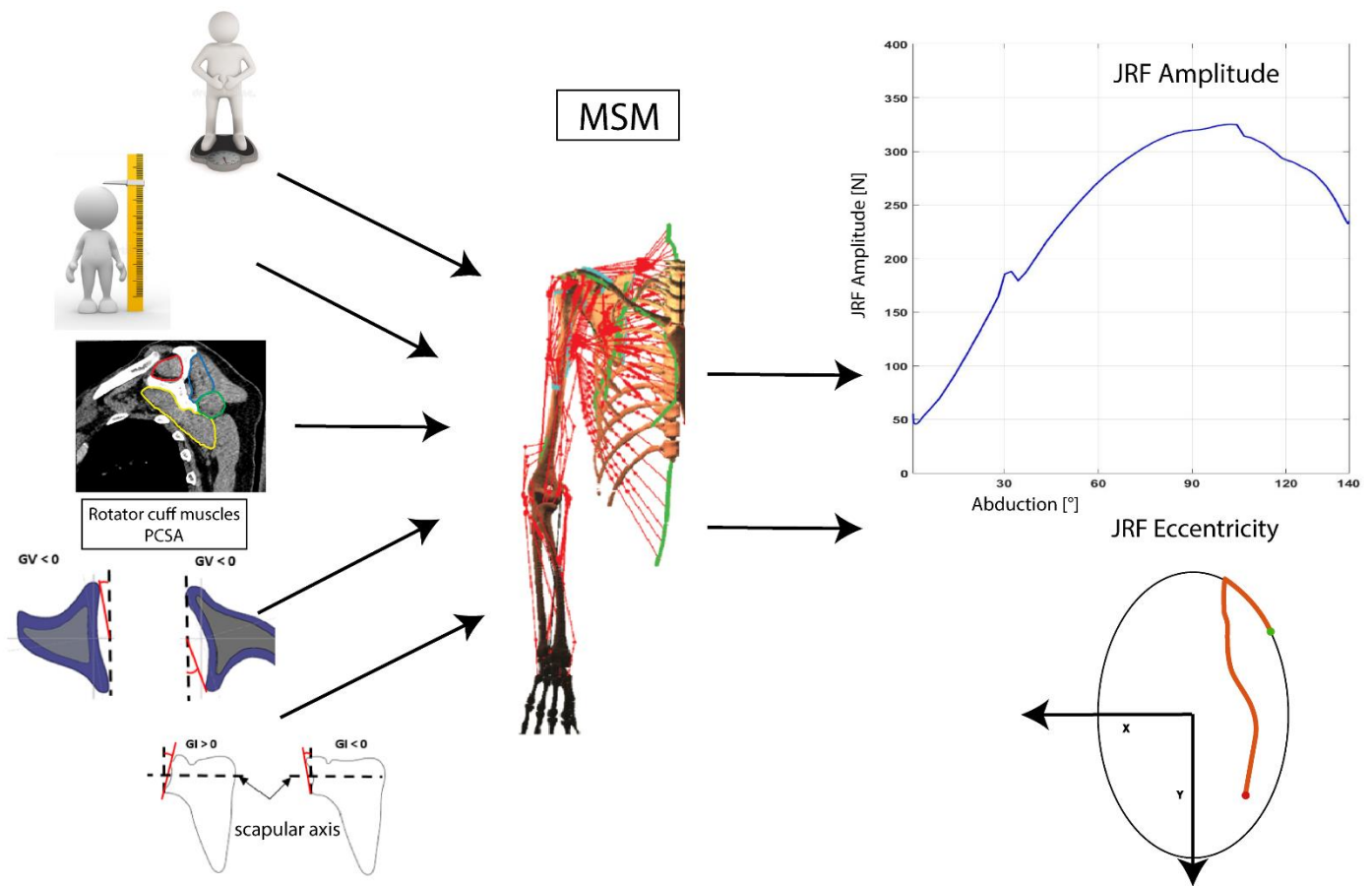
4.1 Abstract

Patient-specific musculoskeletal modeling is needed to estimate joint reaction forces (JRF) of a specific patient, but its development represents a challenge: the choice of personalized parameters, the optimization techniques used, the inputs chosen and validation processes used are not obvious and difficult to quantify. Starting from a generic upper limb musculoskeletal model [48,139,140] of a healthy volunteer, we considered five parameters to adapt for each patient: bodyweight, height, physiological cross-sectional area of muscles, glenoid inclination and glenoid version. With the help of measured kinematics and electromyography data, the numerical model predicted JRF for eleven activities of daily living. In addition, a sensitivity analysis of the model to its patient-specific inputs and to muscle degeneration was performed for an abduction at 60°. Results were consistent with other models' predictions and instrumented prostheses measurements. Sensitivity analyses highlighted the importance of bodyweight (20%), height (0.83%) and supraspinatus PCSA (0.41%) on JRF amplitude, while glenoid inclination (25%) and version (9%) were most influential on JRF eccentricity. Rotator cuff muscle degeneration (3%) did not strongly influence JRF amplitude for abduction at 60°. In conclusion, this study identifies this musculoskeletal model as a potential clinical tool to help in diagnosis and instability predictions of prosthesis choice for total shoulder arthroplasty.

4.2 Introduction

The shoulder joint is essential in performing simple daily life activities and its dysfunction may prevent people from basic autonomy. The functionality and underlying mechanisms of this joint are not yet well understood because the needed parameters cannot be obtained in a non-invasive manner. For example, the behavior of deep muscles and joint reaction forces cannot be measured in vivo for healthy patients. Numerous musculo-skeletal models (MSM) were developed in the last decades aiming to provide a deeper understanding of the shoulder joint in a non-invasive way. The final goal of most MSM is to be a clinical tool to improve the diag-nosis, pathology, treatment and post-treatment processes [32,33].

Some of the known and used shoulder models are the Delft shoulder and elbow model [36,37], Garner and Pandy model based on the visible human project [38,39], the Swedish model [40], the AnyBody model [41], the Opensim Model [42], the UK National shoulder model [43], the Waterloo model [44], the Case model [45] and the Portuguese model [46]. All these models contain joints of the shoulder complex and their muscles.

Most of the shoulder MSM are based on an inverse dynamics principle, deriving muscle forces from input kinematics, and solving the indeterminacy with static or dynamic cost function minimization. Several cost functions were proposed, as for example the squared muscle forces over the physiological cross sectional area (PCSA) [44], the sum of squares errors between predicted and constrained angles [43], the difference between measured electromyography (EMG) and predicted muscle activity [47], the muscle-energy con-sumption during complete motion [46], a stability function to avoid luxation [48]. The input kinematics can be either mathematically created or measured with 3D motion capture systems. Motion capture systems provide more complex and natural movements, but the soft tissue artefacts remain an important source of uncertainties, especially for the scapula [33].

Validation of MSM is very challenging. For the shoulder, models' predictions were compared to EMG signal measurements [32,33], or instrumented prostheses[49]. These validations remains partial, since surface EMG cannot measure deep muscles, and instrumented prostheses are obviously restricted to patients with a shoulder pathology [33].

The emerging tendency in musculoskeletal modeling of the last decade is the subject-specific modeling [32,33,50], the dream being to create a MSM in a clinical setting that can be adapted quickly to each new patient and thus provide a custom-made diagnosis and treatment approach. The most common and simple approach for patient-specific modeling is to scale the whole model with patient height and bodyweight. Re-cently, specific parameters were adjusted, such as muscle properties based on imaging [50] or kinematic data [32]. However, recent publications [32,50] highlighted the lack of sensitivity analysis and its utmost im-

portance to validate the models. This lack of validation is due to many factors: the huge amount of parameters required in the model steps, the challenge of choosing the correct behavior model for the study, the correct parameters to study and their range; and finally the expensive computational time.

The sensitivity of MSM to predict glenohumeral joint force was reported to be largely determined by glenohumeral joint center location, input kinematics, PCSA of muscles, scapular shape, scaling of muscle insertions and origin locations or segment length. These studies used either parametric approaches, comparisons to experimental data or probabilistic approaches [32,33].

Therefore, the aim of the present study was to extend an existing MSM of the shoulder to add the elbow and make it adaptable to patients planned for anatomical Total Shoulder Arthroplasty (aTSA). This model was used to predict Joint Reaction Forces (JRF) during eleven activities of daily living. The second goal of this study was to perform a sensitivity analysis of this model to patient-specific parameters, and especially to rotator cuff muscle degeneration.

4.3 Materials and Methods

4.3.1 Generic musculoskeletal model

The original MSM [48] was based on MRI data of a healthy male volunteer (Body weight 85.5 kg and Height 186 cm) and included thorax, humerus, scapula, clavicle, and 42 muscles, each represented by three cables. The inverse dynamic method was implemented in MATLAB (MathWorks, USA) to simulate simple abductions in the scapular plane up to 120 ° and output muscle forces and joint reaction forces (JRF). Three optimizations were implemented: first, the minimization of the cost function being the square of muscle stress. The second optimization minimized the eccentricity of the JRF with respect to the glenoid center to avoid luxation. The third optimization used the multicriteria optimization principle to link both cost functions. The model was validated against kinematic and EMG measurements of the volunteer during arm elevation [141].

In the present study, the original model was extended by adding the forearm of the same healthy volunteer. A half-body MRI was made following a specific protocol. The new MRI images were registered on the original ones then the bones: Ulna, Radius and hand were segmented (Figure 4:1 a). Second, the bony landmarks of the forearm and hand were added following the International Society of Biomechanics (ISB) standards [142]. Third, 14 muscles were added: Biceps brachii long and short heads, Triceps brachii long, medial and lateral, Brachialis, Brachioradialis, Supinator, Pronator Teres, Flexor Carpi Ulnaris, Flexor Carpi Radialis, Extensor Carpi Radialis Long and Brevis, Extensor Carpi Ulnaris. Lastly, the insertions and origins of the muscles were placed on the segmented bones using the MRI data and anatomic atlases [143,144]. The above-mentioned steps were all performed using Amira (v. 6.4, FEI Visualization Sciences Group, Burlington, MA, USA).
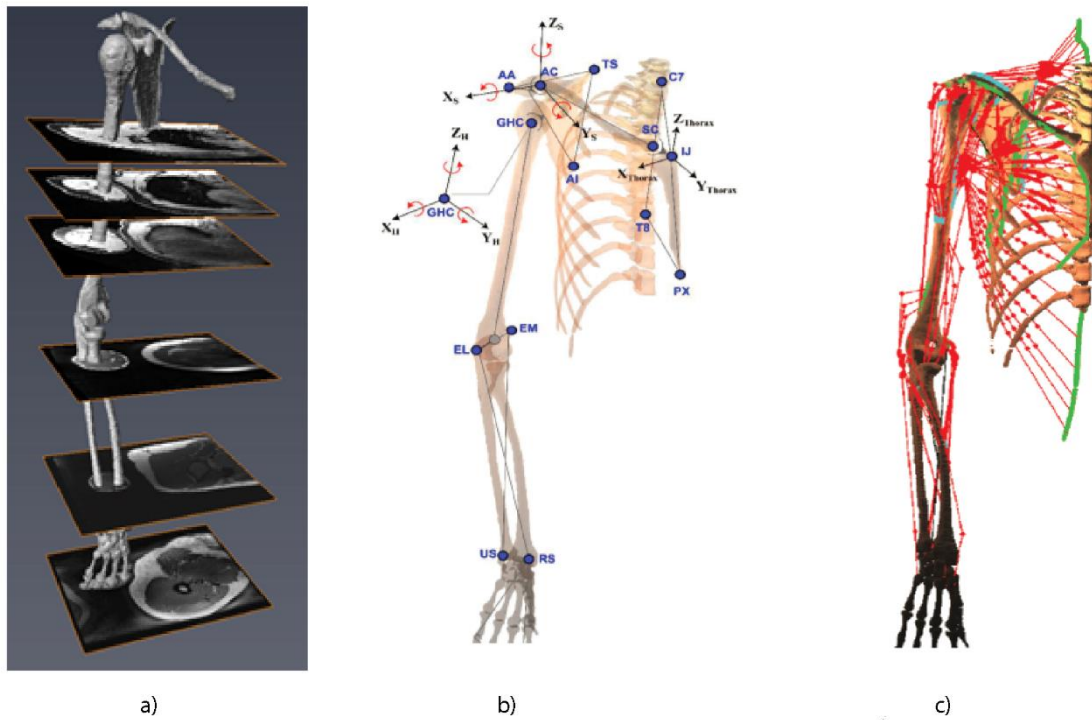
Figure 4:1 a) Reconstructed bone from MRI data b) Bony landmarks and reference frames c) Implemented MSM.

(Images from PhD theses: b) courtesy of Mancuso [145]; c) courtesy of Sarshari [146])

Moreover, kinematic data of 11 palpable bony landmarks using 3D motion capture systems and EMG data of 15 superficial upper limb muscles were collected on the healthy volunteer during 11 activities, 8 of which are considered activities of daily living (ADL). These kinematic and EMG data were incorporated to the MSM in order to bring more stability. The activities recorded were: act1 Abduction frontal plane with 2 kg, act2 Elevation sagittal plane with 2 kg, act3 Abduction scapula plane with 2 kg, act4 Fast abduction scapula plane, act5 Slow abduction scapula plane, act6 Put 2 kg in a shelf at head height, act7 Hand behind the head, act8 Touch the other shoulder, act9 French canes, act10 Counter external rotation (static pose, no motion), act11 Counter internal rotation (static pose, no motion) [145].
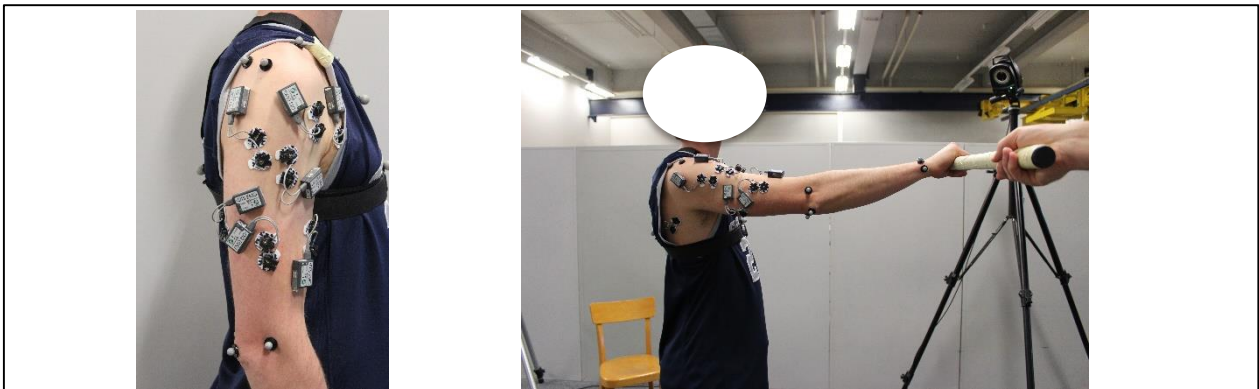
Figure 4:2 Bony markers and EEG of volunteer during activities of daily living.

In order to output the glenohumeral JRF, equations of motion were implemented where bones were considered as rigid bodies, joints as ideal mechanical joints without translations and muscles as elastic strings. Muscle paths were thus needed and they were represented using obstacles, via points and wrapping objects. These were placed following the obstacle-set method described by [147] and using the CT data of the volunteer for each of the 42 muscles. The force exerted by each muscle was calculated using a validated Hill-type musculotendon model [146]. Two important features of the model are first the EMG assisted load sharing (EALS) feature based on measured EMG data of each muscle [148]. The muscle force satisfies the following optimization: the sum of squared muscle stresses was minimized for the force was either zero (lower bound) or it was $F\_c = k*PCSA$, where k is the Fick's constant and PCSA the physiological cross sectional area of the muscle [146]. Each muscle can be represented by up to 20 strings (Figure 4:11 b). The second important feature introduced in this model is the stability constraint: the joint reaction force was constrained such that it would always point towards the glenoid fossa and never fall out of it [146].

The model has 9 degrees of freedom (DOF) [149]:3 ball-and-socket-joints: sternoclavicular, acromioclavicular and glenohumeral joints and two hinge joints for humeroulnar and radioulnar joints. Pronation and supination of the forearm were additionally implemented. The orientation of each bone segment was defined with help of the bony landmarks and 6 bone-reference-coordinate systems were defined for the motion: the thorax frame, the scapula frame, the humerus frame, the cone frame (which represents the glenoid fossa), the Ulna frame and the Radius frame (Figure 4:1 c). The MSM outputs glenohumeral JRF defined as JRF Amplitude (JRFa) and projected JRF on the glenoid fossa, defined as JRF Eccentricity (JRFe).

To validate the new MSM, comparison against available literature data and instrumented prostheses was performed and presented in [146].

4.3.2 Patient-specific musculoskeletal model

The generic MSM was extended in order to be patient-specific by adding the following parameters: gender, bodyweight, height, physiological cross-sectional area (PCSA) for each muscle, glenoid inclination and glenoid version.

To adapt a generic model to a new patient, a scaling was implemented based on height and bodyweight inputs: the ratio of patient's data on the generic data outputs a factor which will scale the maximal muscle force of the patient. The location of the bony landmarks, origin and insertion points of each muscle are scaled as well. The EMG data were scaled according to patient's bodyweight. The scaling factors used were derived from a previous work by [150]. Moreover, the MSM is able to accept PCSA values for patients. The PCSA was

contoured by a professional radiologist and a MATLAB (The Mathworks, Inc) script was written to calculate the area of each muscle which serves as input to the patient-specific MSM (Figure 4:3). Details about the integration of EMG data to stabilize the MSM are found in the following PhD theses [145,146].
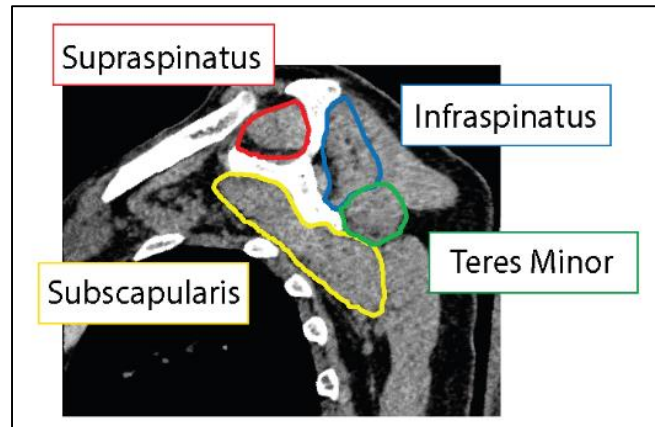
Figure 4:3 CT data of patient's shoulder showing contouring of rotator cuff muscles' PCSA performed by a professional radiologist.

4.3.3 Output

The patient-specific MSM predicted muscle forces, joint reaction force amplitude (JRFa) and joint reaction force eccentricity (JRFe), for given patient-specific anthropometric parameters. The JRF was output with respect to time. JRFe was defined as distance between the glenoid center and the furthest JRF projection on the glenoid surface.

4.3.4 Sensitivity Analysis

A two-part sensitivity analysis (SA) was conducted for this model: first, a global SA was performed with design of experiment (DOE) method, in order to establish a ranking of the most influential patient-specific parameters on JRF. Second, SA of model predictions with respect to rotator cuff muscle degeneration was performed.

4.3.4.1 Global SA using DOE

DOE method was used to investigate the sensitivity of JRFa and JRFe to the five patient-specific parameters described above. For each of these anatomical parameter, mean and standard deviation were chosen as DOE levels (Table 4:1). These values were taken from measurements on preoperative CT scans of 107 patients planned for anatomical total shoulder arthroplasty [29,151,152].

We considered an abduction position in the scapular plane at 60 degrees of elevation. The patient-specific MSM predicted all muscles' and joint forces, but we considered here only JRFa and JRFe. JRFe was defined as distance between the glenoid center and the intersection of JRF with the glenoid surface.

A linear model with first and second order interactions was chosen for this two-level full factorial study. Second and higher-order interactions were not considered. A total of 32 cases were thus investigated for JRFa and JRFe. DOE provided a ranking of the important parameters investigated and their contribution. Main effect plots were used to visualize the contribution of each anatomical parameter to JRFa and JRFe. In a last step, an analysis of variance (ANOVA) with 95% confidence interval was conducted to investigate the significance of the DOE contributions (p-values < 0.05).

Anatomical parameters	Min	Max
Bodyweight (KG)	60	90
Height (CM)	160	174
PCSA Supraspinatus (CM^2)	5	8
Glenoid Inclination (°)	2	15
Glenoid Version (°)	-10	5

Table 4:1: Anatomical parameters considered for the two-level (min and max) full factorial DOE.

4.3.4.2 SA to muscle degeneration

In order to perform a SA of this model to rotator cuff muscle degeneration, the generic model was adapted to 40 aTSA patients. They were 15 men and 25 women, the age was 74 ± 9 years, the body bodyweight (BW) was 77.75 ± 18.5 kg, the height was 64 ± 10 cm, the glenoid version was -9 ± 12° (negative for retroversion), the glenoid inclination was 4 ± 6.7°. The average rotator cuff muscle degeneration was 53% for supraspinatus, 39% for infraspinatus, 42% for subscapularis and 38% for teres minor. These parameters were introduced into MSM to estimate JRF during an abduction movement. JRF was reported as %BW. JRF at 60° and 90° abduction were considered. JRF values with degenerated muscles were compared to JRF obtained with non-degenerated muscles. The differences of JRF were statistically compared with a paired t-test. Finally, the correlation between JRFa and muscle degeneration was evaluated.

4.4 Results

4.4.1 JRF Amplitude and eccentricity in generic musculoskeletal model

For the generic model based on the young volunteer, the peak JRFa was 580 N at 97° abduction, i.e. 68% BW (Figure 4:4). Over the abduction movement, the peak JRFe was 15 mm at 50° abduction and was 7.6 mm at 60° abduction.
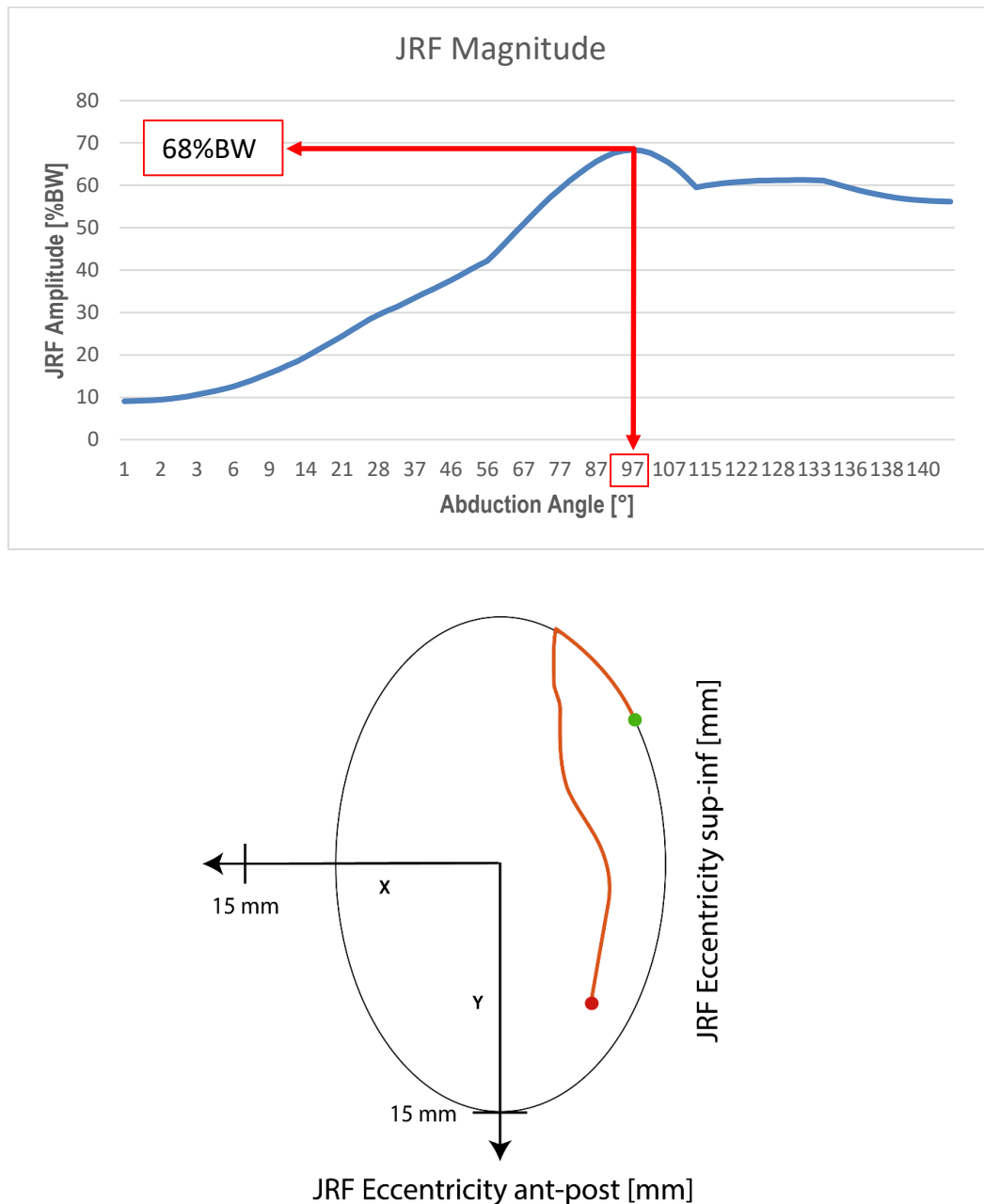
Figure 4:4 Joint reaction force amplitude (top) and eccentricity (bottom) during abduction illustrated on the glenoid fossa: green points marks the start of the movement at 0° abduction and red point marks the end of the movement at 140°. The red line represents the angles comprised between 0° and 140°. Eccentricity was calculated by intersecting JRF with the glenoid surface.

4.4.2 Global SA using DOE

4.4.2.1 Joint reaction force amplitude

The main effect plots (normalized mean value of JRFa (=383 N)) showed that JRFa increased proportionally with BW while Height and Supraspinatus PCSA had almost no influence (Figure 4:5). Subsequent analysis of variance (Table 4:2) confirmed these tendencies: the most influential parameter on JRFa was BW (20%), Height (0.8%) and supraspinatus PCSA (0.4%). All values were highly significant (p < 0.001).
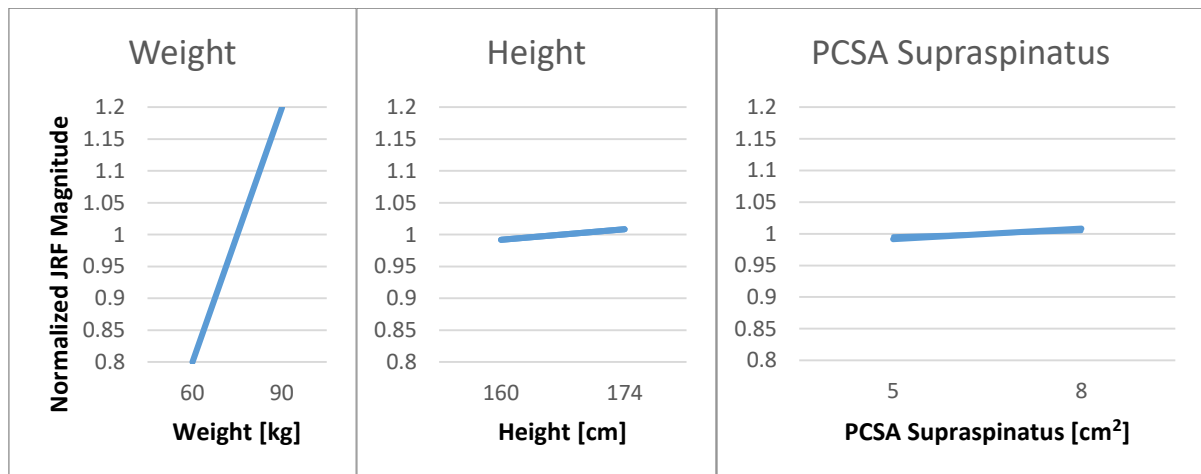
Figure 4:5 Main effect plots of all cases normalized to the mean value of JRFa (=383 N) for all 32 cases.

Anatomical parameters	JRF Amplitude	
	Contribution	p-value
Bodyweight	20.00%	<0.001
Height	0.83%	<0.001
SS PCSA	0.41%	<0.001

Table 4:2 ANOVA results for JRFa.

4.4.3 Joint reaction force eccentricity

The main effect plots (Figure 4:6) show that the JRFe increases proportionally with glenoid inclination and glenoid version while it decreases with increasing height. The influence of both glenoid version and height was similar. Subsequent analysis of variance (Table 4:3) showed the most influential factors on JRF eccentricity to be glenoid inclination (17.1%), height (-4.3%), glenoid version (3.9%) and the combinations version/inclination (3.7%) and height/version (-2.3%). All values were highly significant (p < 0.001) Table 4:3.
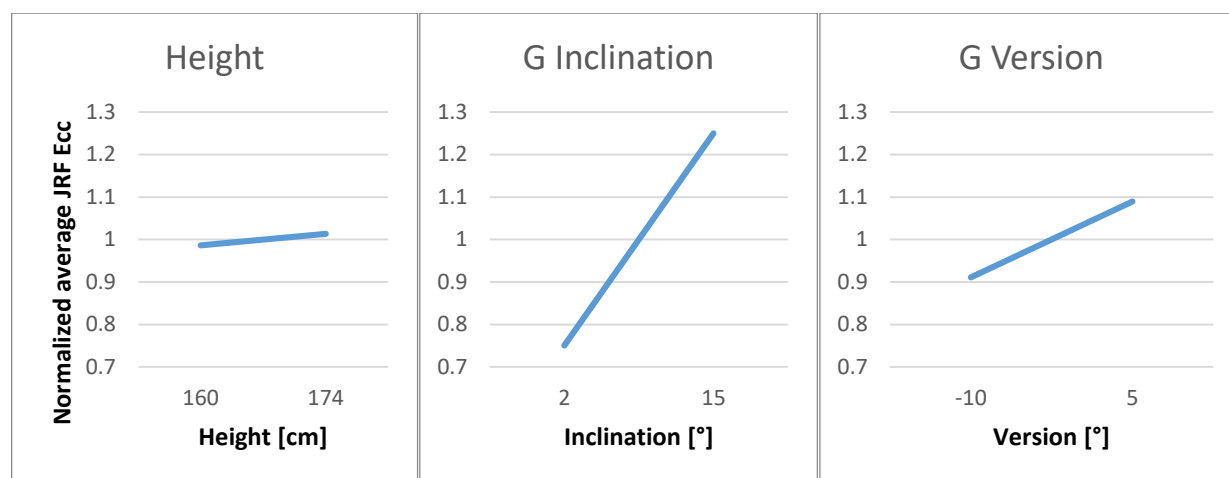
Figure 4:6 Main effect plots of all cases normalized to the mean value of JRFe (11 mm).

Anatomical parameters	JRF Eccentricity	
	Contribution	p-value
Height	1.35%	<0.001
G Inclination	-24.99%	<0.001
G Version	8.92%	<0.001
Height X G Version	-0.62%	<0.001
G Inclination X G Version	1.41%	<0.001

Table 4:3 ANOVA results for JRF eccentricity.

4.4.4 Sensitivity analysis to muscle degeneration

JRF with healthy muscles was 0.50 ± 0.13 BW at 60° and 0.66 ± 0.16 BW at 90° abduction (Table 4:4). When degenerated muscles were considered, JRF decreased to 0.48 ± 0.13 BW at 60° and 0.65 ± 0.14 BW at 90° abduction. Peak JRF difference (in %JRF of healthy muscles) was 0.25 but the average JRF differences were small: 0.03 ±0.05 at 60° and 0.024±0.07 at 90° abduction. The differences were statistically significant (p=0.028) for 60° abduction (0.03±0.05, p=0.028), but effect size was small (0.20), Table 4:4.

JRF [%BW]	Healthy	Affected	Effect size	P-value
60° Abduction	0.50 (±0.13)	0.48 (±0.13)	0.20	P=0.028
90° Abduction	0.66 (±0.16)	0.65 (±0.14)	0.18	P=0.09

Table 4:4: Results t-test: effect of muscle degeneration of JRFa.

The correlation between JRF change and rotator cuff muscle degeneration at 60° and 90° abduction was significant, but weak to moderate. Only the correlation between JRF change and Supraspinatus at 90° abduction was not significant (p = 0.08,Table 4:5). More specifically, as rotator cuff muscle degeneration increases, JRFa decreases (Figure 4:7).

	Supraspinatus	Infraspinatus	Subscapularis	Teres Minor
60° Abduction	R = -0.17. p = 0.02	R = -0.14, p = 0.003	R = -0.37, p < 0.001	R = -0.50, p < 0.001
90° Abduction	R = -0.17, p = 0.08	R = -0.24, p = 0.002	R = -0.37, p = 0.007	R = -0.59, p < 0.0001

Table 4:5 Results: Correlations between JRFa and rotator cuff muscle degeneration.
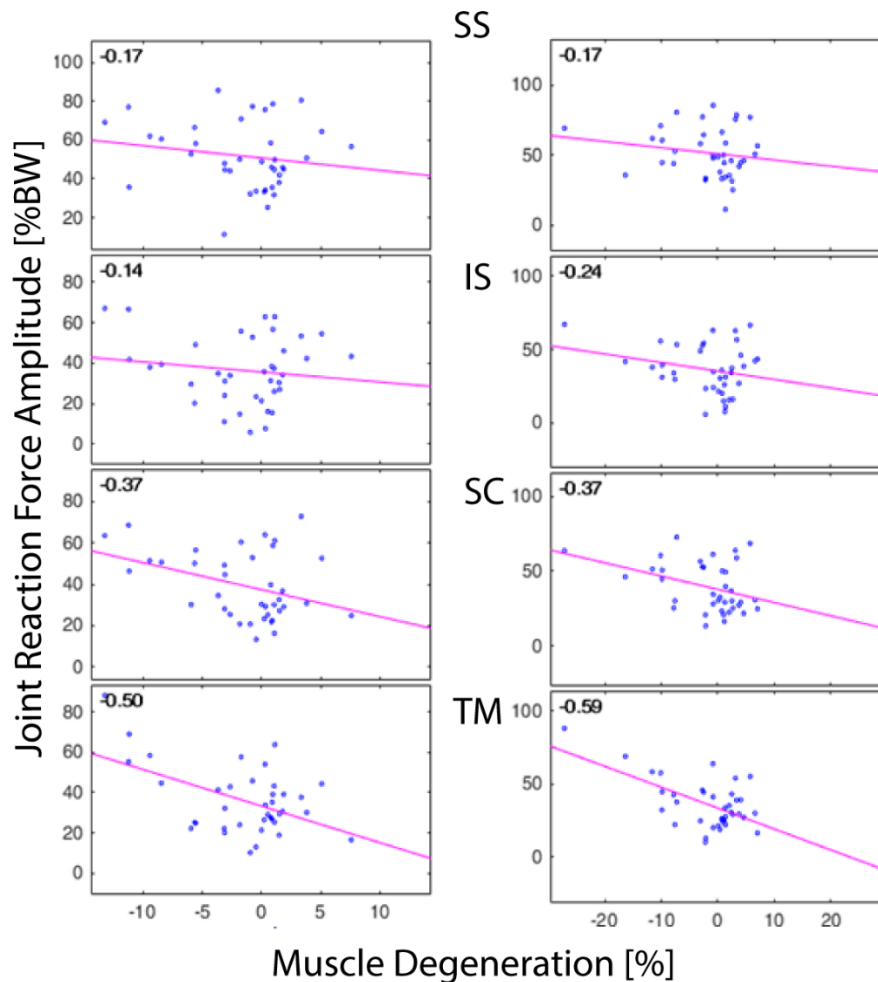
Figure 4:7 Correlation plots at 60°abduction (l.) and 90° abduction (r.) for SS, IS, SC, and TM (from top to bottom) to Joint Reaction Force Amplitude

4.5   Discussion

A generic musculoskeletal model (MSM) of the shoulder was extended to include the forearm and to be adapted to patient-specific anthropometric parameters (bodyweight, height, rotator cuff muscles PCSA, glenoid Inclination and glenoid version). The MSM developed was able to output muscle forces and joint reaction force amplitude and eccentricity values similar to published data (in vivo-measurements, numerical studies and instrumented prostheses) [146].

The anatomical parameters taken into account in this study were bodyweight, height, Supraspinatus PCSA, glenoid version and glenoid inclination of patients planned for anatomical total shoulder arthroplasty. The height and bodyweight are the obvious choices when considering differences amongst patients. The PCSA of Supraspinatus is routinely checked before a total shoulder arthroplasty and is stated to be the most frequently and most severely degenerated rotator cuff muscle [152]. Based on that study, the PCSA of Supraspinatus was chosen. The glenoid inclination plays an important role in the occurrence of osteoarthritis and shoulder joint instability [153–155]. The glenoid version was chosen because it has been associated with rotator cuff tears [156,157] and suggested to be associated to posterior instability [157].

A sensitivity analysis to patient-specific parameter changes (bodyweight, height, supraspinatus PCSA, glenoid Inclination and glenoid version) performed on shoulder joint reaction force (JRF) amplitude (JRFa) and eccentricity (JRFe) during abduction using the design of experiments method (DOE) showed the most influential anatomical parameters on the JRFa to be the bodyweight, the height and the Supraspinatus PCSA. The glenoid orientations had no effect. This result was expected since the scaling of the bodyweight and height leads to a scaling in the muscles PCSA which in turn has an effect on the maximum force achievable by the muscles. Minimizing the muscle force over its corresponding PCSA is a constraint used in musculoskeletal modeling which explains its important influence on the shoulder JRF.

JRF amplitudes at maximum abduction in instrumented prostheses [49] show a clear importance of bodyweight: an increase in bodyweight induces an overall decrease in JRFa for most of the 7 patients performing an abduction up to 150°. However, the opposite tendency was observed in the present study. This is due to the scaling method implemented: a change in bodyweight will scale the PCSA of muscles and the inertia of bone segments no matter how the increased mass is distributed on the body.

DOE predicted an important effect of glenoid inclination and version on the JRF eccentricity while bodyweight, height and Supraspinatus PCSA had almost no impact. This behavior is intuitive and was confirmed by studies which associated glenoid version to posterior instability [153,157] and another study which found a high correlation between glenoid inclination and glenohumeral supero-inferior translation [155].

116

The present work showed rotator cuff muscle degeneration induced a negligible but significant change in JRFa (less than 3%) for 60° abduction. This hints at the recruitment of other muscles to perform the abduction task. This finding is confirmed by a study on six healthy subjects [158] which found a 1.5% change in JRF due to PCSA changes. Another study limited the influence of rotator cuff muscles to less than 50 N [48], meaning that even at PCSA of 2 cm^2, the task will still be performed by the rotator cuff muscles and thus no influence will be seen in JRF [146]. Among our patients, only 27.5% of them had a SS PCSA of less than 2 cm^2 and 30% of them had a TM PCSA of less than 2 cm2.

The main limitations of this study lie first in the statistical approach chosen: some of the combinations investigated in the DOE study may not be representative of the real population, e.g. it is quite unlikely that a very tall person would have a large bodyweight while having a small Supraspinatus PCSA. However, having taken anatomical parameters from an actual patients' database and the standard deviation values (i.e. 65% around the average) reduce the discrepancy. Moreover, DOE needs discrete points of investigation which might hide some effects. Indeed, another parametric study on this MSM was conducted in order to investigate the influence of PCSA on JRFa during abduction and found negligible effect for the motion up to 60° abduction but important effect when abduction was higher [146]. A recent review of rigid MSM highlighted the difficulty to identify the true range of each input parameter in a MSM [32]. Second, the relative importance of bodyweight on the JRF amplitude might be exaggerated due to scaling method chosen: when the bodyweight is entered, the scaling is done on all bone segments of the body, however, in some cases, especially for elder patients, the bodyweight is not uniformly distributed on the body, thus not influencing the mass of the arms and forearms. It would be interesting to compare findings normalized over upper-arm mass. Another limitation is the single abduction movement simulated. It would be interesting to investigate a more extreme rotator cuff muscle degeneration on the four ADL simulated.

The strength of this study was the use of an elaborated statistical approach for sensitivity analysis: to our knowledge, this study is the first to present a ranking of importance of anatomical parameters in a subject-specific shoulder model. Moreover, this model was applied on 40 patients.

To conclude, this study showed that bodyweight, height, supraspinatus PCSA, glenoid inclination and glenoid version influence the joint reaction force predicted by the patient-specific musculoskeletal model. We therefore recommend to account for this information in future clinically related applications of the musculoskeletal model.

Chapter 5   Clinical Application: patient-specific glenoid bone model

This chapter answers the following clinical questions posed earlier in the thesis: 1) Do overcorrected implants reduce postoperative subluxation? 2) Do overcorrected implants transfer excessive stresses within the cement at the bone-implant interface? By creating three patient-specific finite element models, each simulating the implanted prosthesis vs. the overcorrected one. The FE model creation steps are based on the workflow used for specimen-specific glenoid bone FE model as discussed in Chapter 3. The applied loading on the glenoid implants stems from the developed patient-specific musculoskeletal model presented in Chapter 4.
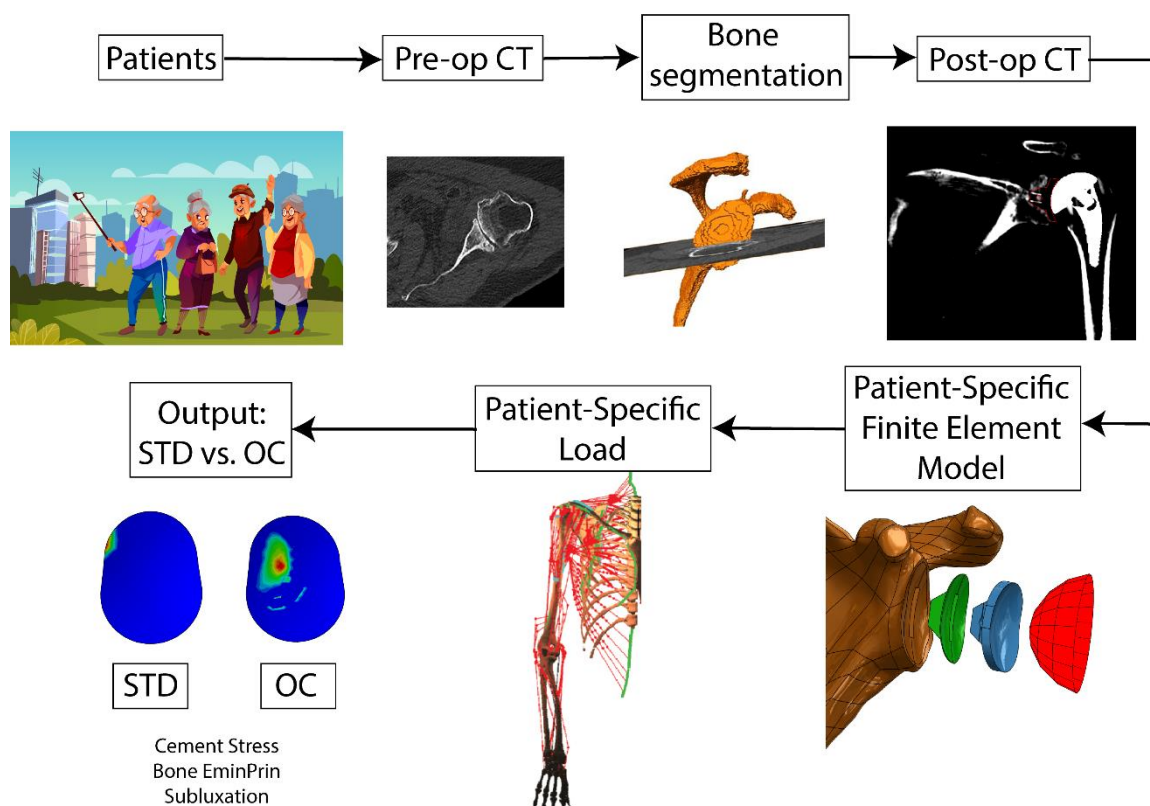
5.1 Abstract

Glenohumeral osteoarthritis is common in the elderly and anatomical total shoulder arthroplasty (aTSA) is recommended in advanced stages. Even though aTSA is an established procedure, its failure rate and revision surgeries are relatively high compared to hip arthroplasty. One of the leading causes of failure is glenoid implant loosening, often associated with off-center loading. The latter may be reinforced by glenohumeral joint subluxation, defined as humeral head center offset from the glenoid surface center. In this case, asymmetrical overcorrected (OC) glenoid implants were suggested as an alternative to standard implants. The present study aimed to evaluate the potential biomechanical advantages of OC implants compared to standard ones using the patient-specific finite element (FE) model.

Three patients needing an aTSA were recruited, preoperative (pre-op), and six weeks postoperative (post-op) CT images were performed. Each patient's bone geometry was reconstructed from the pre-op CTs and the implant positioned using superposed post-op CT-images. Two glenoid FE models were created for each patient simulating aTSA: one model using the standard implant (STD) and another using the overcorrected (OC) implant. For each patient, a musculoskeletal model predicted glenohumeral joint reaction force (JRF) for four load cases that correspond to daily living activities. This JRF was used as a boundary condition on the patient-specific FE model to predict cement volume above fatigue limit of 7 MPa, bone compressive strain above the elastic limit of 1%, and glenohumeral subluxation. These predicted quantities were compared between STD and OC prostheses. Moreover, a sensitivity analysis to assumed uncertainties in the model creation process: 1) systematic error (-2%, 0, +2%) of CT numbers (in Hounsfield Units), 2) Gaussian filter parameter (0.1, 5, 20) and 3) trabecular bone constitutive law was performed on one patient. A full factorial design of experiment (DOE) method was used to investigate bone octahedral shear strain, axial bone strain, cement von Mises stress, and cement axial strain.

Compared to the STD implant, the OC implant changed the glenohumeral subluxation from posterior to anterior for all patients and load cases F2 to F4. For load case F1, posterior subluxation was reduced for patient P3, more centered for patient P2, and not reduced for patient P1. The percentage difference in subluxation lay between 0.5% and 3.2%. No change was observed in critical cement volume when using OC design. Bone volume below the elastic limit mostly increased when using OC design: most important increase was observed at load case F2 for P1 (50.9% bone volume under the elastic limit for STD vs 97.8% for OC) and least substantial increase was observed for patient P3 at F4 (from 99.9% with STD vs 100.0% with OC). Only for P2 at F1 was there an over constrain observed: bone volume under elastic limit was 99.3% for STD vs 22.1% for OC.

Although only applied to three patients, these patient-specific FE models suggest the potential benefit of OC implants when postoperative recurrent subluxation is expected while not overly constraining the underlying bone.

5.2   Introduction

Glenohumeral osteoarthritis is a degenerative joint disease, which causes the breakdown of articular carti-lage and bone. People affected by this disease suffer from severe pain and eventually reduced mobility and life quality. Unfortunately, it is a common pathology. In advanced cases, when rotator cuff muscles are still functional, anatomical total shoulder arthroplasty (aTSA) is suggested. aTSA is an established procedure how-ever, its failure rate and revision surgery are relatively high compared to hip arthroplasty [17]. One of the leading causes of failure is loosening of the glenoid implant, but the mechanisms behind it are still unclear [19,22,23]. Amongst others, this failure may be due to excessive cement stress leading to cement failure, glenoid [54,65,159] implant design [54,59], or to humerus implant-glenoid implant conformity [66,67]. Gle-noid implant loosening is often associated with off-center loading [14]. The latter may be reinforced by shoul-der subluxation, which is an instability present in the glenohumeral joint.

Shoulder subluxation is defined as the humeral head's relative position with respect to the glenoid fossa and/or the scapular axis. Walch et al [26] defined three types of osteoarthritic glenoids. In the absence of subluxation, the glenoid is symmetrically eroded and is called type A. Type B occurs when there is a subluxa-tion: the wear of the joint occurs asymmetrically, in any direction, but more often posteriorly. Type C is not associated with osteoarthritic wear but with dysplasia. It is hypothesized that preoperative shoulder sublux-ation may cause recurrent postoperative instability, resulting in glenoid loosening and eventually, prosthesis failure. As such, for patients planned for aTSA and presenting a risk of recurrent postoperative glenohumeral subluxation, asymmetrical overcorrected glenoid implants have been suggested as an alternative to classical implants. The potential advantages of these asymmetrical implants have however, never been assessed clin-ically.

Finite Element (FE) models have proved their potential to analyze and predict the mechanisms around total joint arthroplasty and have been used for the past 40 years [51]. Many models simulating shoulder arthro-plasty exist and are becoming more sophisticated, with a clear tendency towards patient-specific modeling. However, due to the complexity of the shoulder's musculoskeletal system and the difficulty of getting accu-rate measurements, many simplifications and assumptions need to be made on several levels. Two most common limitations associated with shoulder FE modeling are first the lack of patient-specific parameters: in-vivo loading, exact patient geometry [5], and lack of correct bone constitute law [5,75,76]. The second major limitation of FE models is the lack of experimental validation [5,69,73,74].

On the other hand, musculoskeletal models (MSM) were developed to provide a better understanding of the complex interplay of bones, muscles and tendons in ensuring the shoulder function. Amongst other param-

eters, MSM are able to predict muscle forces and joint reaction forces [33]. In order to get a more comprehensive representation of the population, there is an increasing interest to develop patient-specific MSM [160]. However, most of these models either use cadaveric values based on scaling [32,34] or are based on a small number of subjects [35].

To assess the biomechanical advantage of the overcorrected implant over the classical one, the primary objective of this study was to create patient-specific FE models for three patients. The FE model generation was based on a verified specimen-specific FE model presented in Chapter 3. The shoulder joint reaction force applied to each model was specific to each patient thanks to the validated patient-specific MSM described in Chapter 4. The two main questions asked were: 1) do overcorrected implants reduce posterior subluxation? And 2) do overcorrected implants transfer excessive stresses to the cement at the bone-implant interface?

5.3   Materials and Methods

5.3.1   Patient recruitment and imaging

Three aTSA patients were recruited at the Lausanne University Hospital (CHUV). Both senior orthopedic surgeon (Service of Orthopedics and Traumatology) and radiologist (Department of Diagnostic and Interventional Radiology) collaborating in this project received ethical committee approval to recruit and work with the patients (CER-VD 395-15). A specific shoulder CT scan protocol was established. Each patient underwent one preoperative (pre-op) shoulder CT scan (Discovery CT750 HD, GE Healthcare, Waukesha, WI, USA) and one postoperative (post-op) CT scan. An anthropomorphic thorax K2HPO4 phantom was scanned with each patient (QRM, Moehrendorf, Germany). Following CT scan settings were used: 120 kVp tube potential; 200 mA tube current; 0.7 s gantry revolution time; 64 x 0.625 mm beam collimation; 0.984 pitch. Image reconstruction parameters were: 1.25/0.7 mm section thickness/interval, 488 x 488 μm in-plane spatial resolution; sharp (bone plus) kernel.

Based on the pre-op CT-data, a MATLAB (R2017b, The Mathworks Inc, Natick, USA) code was written to measure patient-specific anthropometric data: apparent density, glenoid inclination, glenoid version (Figure 5:1), and the Physiological Cross-Sectional Area (PCSA) of each of the four rotator cuff (RC) muscles: Infraspinatus (IS), Subscapularis (SC), Supraspinatus (SS) and Teres Minor (TM). Beforehand, each RC muscle was contoured by the expert radiologist on the CT data. Moreover, the senior shoulder surgeon used the pre-op CT data in the 3D preoperative planning software and patient-specific instrumentation (BLUEPRINT™ 3D Planning, Tornier-Wright Medical, Montbonnot-Saint-Martin, France). In this step, both humeral and glenoid implant type, size and positioning were planned ahead of the surgery.

An overview of the patients of this study and their anthropometrics data is presented in Table 5:1.

	Age	Implant	Gender	Height [cm]	Weight [kg]	Version [°]	Inclination [°]	PCSA [cm²]			
								IS	SC	SS	TM
P1	74	S40	M	163	110	-15.45	5.34	2.76	8.58	1.13	0.92
P2	79	M35	F	170	90	-8.73	5.29	7.66	9.00	3.00	0.25
P3	54	M40	M	185	104	-0.37	-3.38	10.69	25.51	6.49	4.86

Table 5:1: aTSA patients of the study.
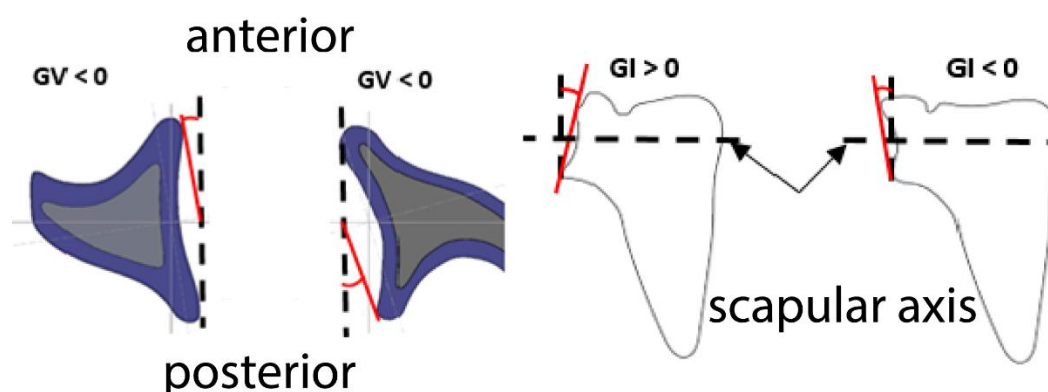
Figure 5:1 Schematic showing glenoid orientations: glenoid version (GV) and glenoid inclination (GI).

5.3.2 Patient-specific geometry

The workflow used to create a patient-specific FE model from CT data was introduced in chapter 2. First, the pre-op CT data of each patient was imported and rigidly registered to post-op CT data. The Computer-Aided Design (CAD) file of the glenoid implant, provided by the manufacturer (AEQUALIS™ PERFORM keeled sizes S and M, Tornier-Wright Medical, Montbonnot-Saint-Martin, France), was superimposed over the post-op CT to replicate its real positioning correctly. These steps were performed using Amira 2019.2 (FEI SAS, Burling-ton, MA, USA), Figure 5:2. In a second step, each patient's scapular bone was segmented from the pre-op CT. This segmentation was based on CT number (Hounsfield Units) thresholds but was manually corrected when required from visual inspection. Bone surface triangular mesh creation and smoothing were performed with Geomagic Design X (3D Systems, Inc).

Figure 5:2 Postoperative CT of patient where glenoid implant is outlined (red, left picture) and then correctly placed using manufacturer's CAD model (blue, right picture).

The segmented bone and the correctly placed glenoid implant were imported in Solidworks 2019 (Dassault Systèmes SolidWorks Corporation) where virtual implantation was performed according to 3D preoperative

planning. A cement layer with a uniform thickness of 0.5 mm was added around the implant with a backside of 2 mm based on the average measured cement thickness on the micro-CT images in chapter 3. The virtually implanted scapular bone, glenoid implant, and cement layer were imported into Abaqus (v.6.14, Simulia, Dassault Systèmes), where a rigid hemisphere was added to account for the metallic humeral component articular surface (Figure 5:3).
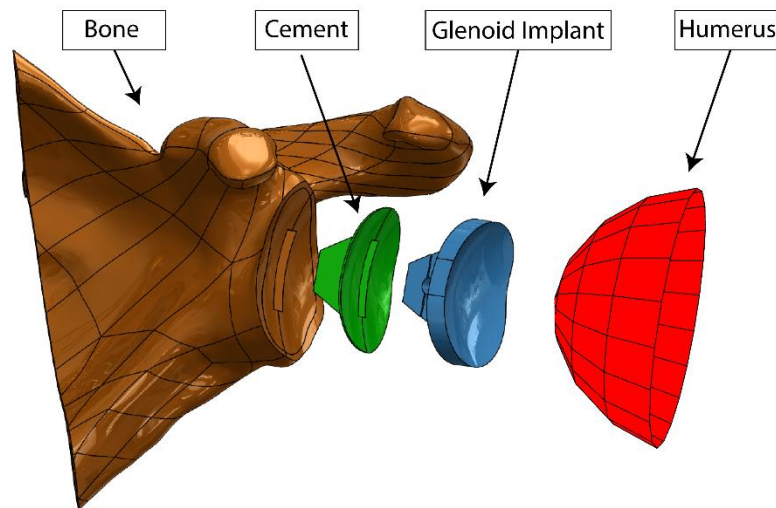
Figure 5:3 FE model for patient P1: brown: implanted glenoid bone, green: cement layer, blue: glenoid implant and red: humerus.

5.3.3 Overcorrected implant design

Based on the surgeon's recommendations and previous testing, the overcorrected implant was designed with a posterior overcorrection of 10°. This overcorrection design modification was performed on the articular side, without changing the bone side of the implant (Figure 5:4).
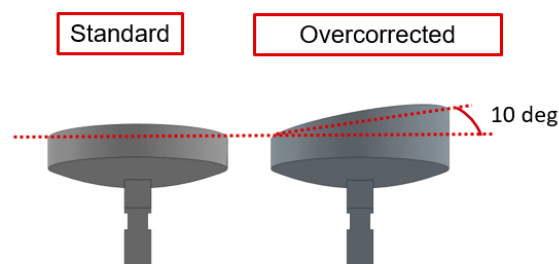
Figure 5:4 Standard implanted prosthesis (left) and its corresponding overcorrected prosthesis (right)

5.3.4   Material properties

Linear elastic homogeneous material properties were assumed for implant and cement, based on manufacturer data (Table 5:2). Based on the findings of chapter 2, the glenoid bone was assigned Rice's density-dependent bone constitutive law (Table 5:2). As described in chapter 2, a MATLAB script was written to give HU values to the glenoid bone mesh based on the K2HPO4 anthropometric phantom ρ_{CT} [g/cm³] = HU/1460. A friction coefficient of 0.3 was applied between the metallic humeral head and the polyethylene glenoid implant. Both implant – cement and cement – bone surfaces were fully bonded using tied constraints. Following a mesh convergence analysis (Supplementary Material Section 5.6), a tetrahedral mesh with an average size of 1 mm was assigned to the glenoid bone, and to the cement, and 2 mm tetrahedral mesh was assigned to the glenoid implant.

Material	Elastic Modulus [MPa]		Poisson's Ratio [-]
Polyethylene (UHMWPE)	720		0.4
Cement (PMMA)	2000		0.23
Humeral head	rigid		rigid
Bone	$E = 60 + 900 * {\rho_{app}}^2$	[123]	0.26 [161]
	$E = 2.192 * \rho_{app} + 0.007$	[162]	
	$\rho_{CT}[\frac{g}{cm^3}] = HU/1460$		

Table 5:2: Material properties used in FE model.

The musculoskeletal model (MSM) developed and described in the previous chapter was used to output the patient-specific joint reaction forces (JRF) during three activities of daily living (ADL) needed in each FE model.

The following patient-specific data were fed into the MSM: weight, height, glenoid implant inclination, glenoid implant version, and PCSA for all four rotator cuff muscles. The glenoid implant orientation (version and inclination) was obtained from the preoperative planning software.

Three ADL were chosen among 7, presented in Chapter 4:

- act3) Abduction in the scapula plane with 2 kg in the hand

- act6) Put 2 kg on a shelf at head height

- act7) Put the behind the head to simulate scratching the head or combing

The JRF was evaluated at 30° and 90°of abduction for act3. For act4 and act7, we considered the abduction angles corresponding to the maximum JRF. For readability ease, the load cases will be reported hereafter: act3 at 30° abduction as F1, act3 at 90° abduction as F2, act6 as F3 and act7 as F4.

The JRF obtained by the MSM for each of the three ADL and three patients were given in the thorax coordinate system [148,163], and thus needed to be transformed into the glenoid implant coordinate system with help of a stability cone coordinate system. Thorax and cone coordinate systems were defined in Sarshari et al. [148] and in Mancuso et al. [163]. The glenoid implant coordinate system was called hereafter GI coordinate system and is presented in red in Figure 5:5.
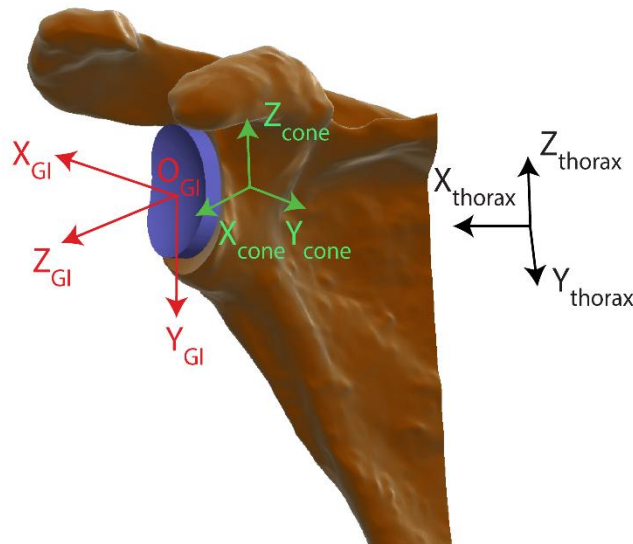
Figure 5:5 Glenoid Implant (GI) coordinate system in red based on thorax coordinate system (black) and on the stability cone coordinate system (green).

(Image courtesy of Mancuso [145])

The GI coordinate system was defined as follows: [145,146]

i)   Origin O_{GI} is the center of the implant

ii) Y_{GI} goes from the most superior to the most inferior rim of the GI. The axis is then projected on the GI plane.

iii) Z_{GI} parallel to Xcone and pointing towards humeral head

iv) X_{GI} was constructed through cross product of Y_{GI} and Z_{GI}

5.3.5   Output

Four load cases were tested for each patient (F1 to F4), for STD and OC glenoid implant.

The outputs investigated in this study were: peak cement von Mises stress and its volume below fatigue limit of 7 MPa. We also considered the bone volume above the reported value of 1% for plastic deformation [89]. Lastly, subluxation is defined as distance of the humeral head center to the glenoid center projected on a plane perpendicular to the glenoid centerline. The glenoid centerline was defined as the axis going through the pre-surgery glenoid surface center and through the center of a sphere fitted in that glenoid surface [29]. Subluxation was expressed as percentage of the humeral head radius and was posterior when pointing in the X_{GI}-direction.

5.3.6   Sensitivity Analysis

The FE model building pipeline needs many steps that may include errors. A sensitivity analysis was conducted in order to identify the most influential factors of the pipeline on the output of the models. The sensitivity analysis was conducted upon three patient models using the Design of Experiment (DOE). The loading applied was based on ASTM 2028 [164]. Three factors were analyzed: First, the Gaussian filter used to average HU values was evaluated: having a Gaussian distribution, the voxels located close to the considered voxel have a larger weight than those located further away. The sensitivity of the FE model to using different Gaussian window length (called distance, d) and dispersion factor or Gaussian window width alpha (α) parameters was assessed by analyzing the possible range of BMD values that an element or region of interest can have. Parameters "d" takes into account the number of neighbouring elements taken into account in the weighing of the HU value of each element, while parameter alpha precises the weight of each element. More details are provided in the supplementary material section 5.6. A total of 21 regions of interest were analyzed and it was observed that no change in BMD values is experienced when α < 0.1 and α > 20. Also, it was observed that the BMD value measured when α = 5 was quite close to the median value of the range. Consequently, the values 0.1, 5 and 20 were considered as factors for the DOE method.

Second, the sensitivity of the model to two different trabecular density-elasticity laws was investigated. Two laws were investigated: Latypova's law [128]:

$$E = 11'035.9 * \rho_{app}^{2.13}$$

Equation 5:1: Latypova's law

And Keller's law [124]

$$E = 10'200 * {\rho_{ash}}^{2.01}$$

Equation 5:2: Keller's law

Third, systematic error of CT numbers (-2%, 0, 2%) was investigated.

A full factorial DOE method was used to investigate variation in bone octahedral strain, bone axial strain, cement von Mises stress, and cement axial strain. In total, 8 simulations were performed and the contributions of the input factors in order of importance was extracted. The results were expressed in terms of top 5% volume. Lastly an analysis of variance using 95% confidence interval was performed on contribution factors calculated.

5.4   Results

5.4.1   Load cases

The MSM output joint reaction forces (JRF) for each patient and each load case, the glenoid implant coordinate system (Table 5:3). JRF for F1 points in the superior-posterior quadrant for patients P1 and P3 while it points in the supero-anterior quadrant for patient P2. JRF for F2 and F4 points in the supero-posterior quadrant for all patients. JRF for F3 points in the inferior-posterior quadrant for all patients. An illustration of these load cases is given for P1 (Figure 5:6)

	P1			P2			P3		
Load cases	Fx [N]	Fy [N]	Fz [N]	Fx [N]	Fy [N]	Fz [N]	Fx [N]	Fy [N]	Fz [N]
F1	97	-706	-400	-223	-714	-161	23	-527	-246
F2	996	-414	-274	1095	-488	-279	1188	134	-326
F3	516	69	-342	595	110	-374	455	181	-238
F4	241	-302	-200	160	-470	-235	167	-283	-194

Table 5:3 Load cases applied for each patient, expressed in the glenoid implant reference system.
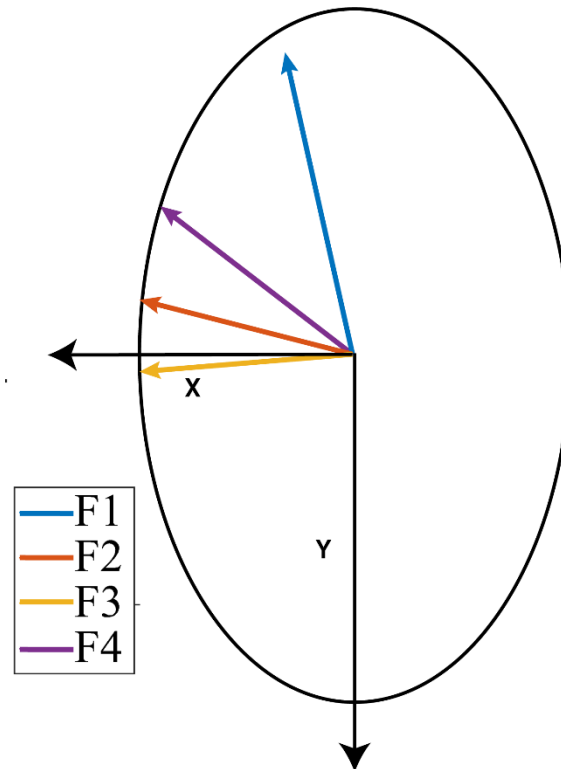
Figure 5:6 Illustration of load cases F1 to F4 for patient P1 given in the GI coordinate system. X-axis points posteriorly and Y-axis inferiorly with respect to glenoid fossa.

5.4.2 Cement stress, bone strain, and subluxation

Compared to the STD design, the OC design made no difference in cement volume above fatigue limit of 7 MPa. Peak cement stress was reduced with load case F2, for all simulated patients when using OC design. No clear difference was observed in peak cement stress for the remaining load cases between STD and OC design (Table 5:4).

With OC implants, volume of bone above the compressive strain elasticity limit of 1% was reduced for all load cases for patient P1 (Figure 5:7) and P3. For patient P2, bone volume below 1% was slightly reduced for F2, F3 and F4. For patient P1 and load case F1, the bone volume above the elastic limit increased when using OC design.

When using OC implant design, posterior subluxation was reduced for all load cases for patient P3. For patient P2, posterior subluxation was reduced for all load cases except load case F1 where the force was pointing in the anterior direction. For patient P1, posterior subluxation was reduced for load cases F2 and F3, stayed similar for F1 but increased for F4 (Table 5:4).

		Cement volume below 7 MPa [%]		Bone volume below 10'000 με [%]		Peak cement Von Mises stress [MPa]		Subluxation [% HH diameter]	
P1		**STD**	**OC**	**STD**	**OC**	**STD**	**OC**	**STD**	**OC**
F1		100.00	100.00	85.42	98.06	44	44	2.47	2.96
F2		99.27	100.00	50.86	97.78	71	36	-1.11	-4.30
F3		99.94	99.99	88.39	96.61	41	50	-0.56	-2.48
F4		100.00	100.00	96.60	98.57	26	39	0.47	1.18
P2									
F1		100.00	98.19	99.31	22.05	47	241	4.78	7.98
F2		100.00	100.00	90.43	90.42	139	92	-13.05	-16.49
F3		100.00	100.00	97.07	92.07	51	114	-8.63	-10.60
F4		100.00	100.00	98.93	94.87	25	82	-0.38	-1.34
P3									
F1		100.00	100.00	90.44	100.00	36	7	-0.09	-0.34
F2		100.00	100.00	98.15	98.23	51	35	-11.46	-14.44
F3		100.00	100.00	99.59	99.19	10	21	-3.29	-4.43
F4		100.00	99.99	99.87	100.00	9	7	-0.79	-0.87

Table 5:4: Cement stress, compressive bone strain and subluxation after application of patient-specific load cases for standard (STD) and overcorrected (OC) implant designs. Negative sign in the subluxation columns corresponds to anterior subluxation.
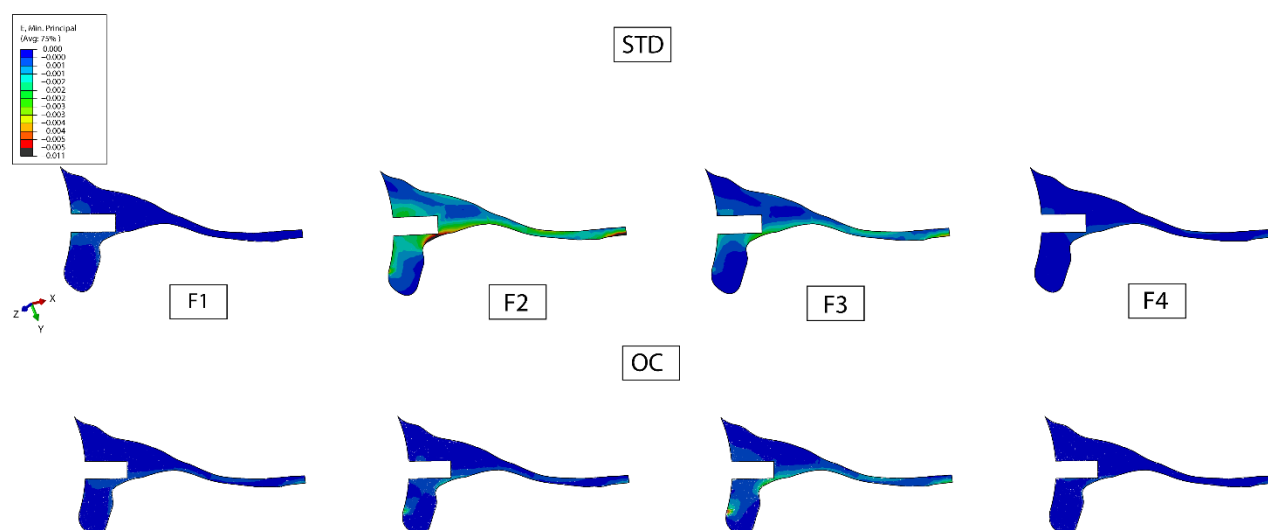
Figure 5:7 Minimum Principal Strain in bone for patient P1 for all simulated load cases and for STD (top) versus OC (bottom) implant designs.

For all simulated load cases and all patients, the contact point between the humerus and glenoid implant was less eccentric with the overcorrected implant than with the STD implant (Figure 5:8)
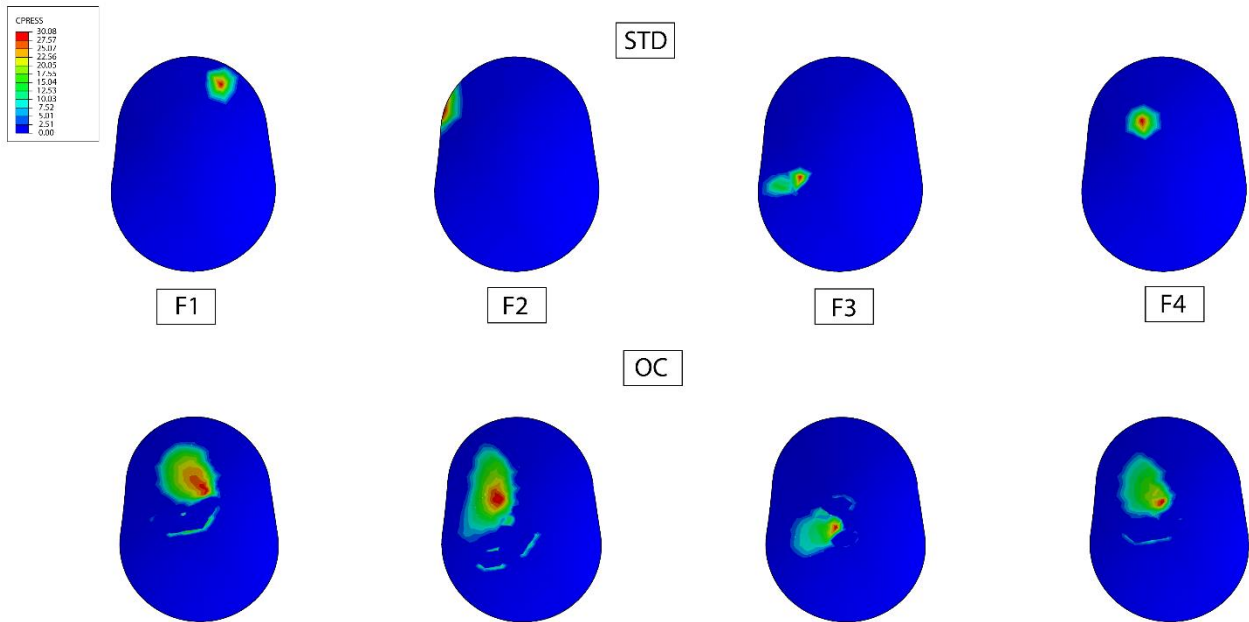
Figure 5:8 Contact pressure on implant for patient P1 for all simulated load cases and for STD (top) versus OC (bottom) implant designs.

5.4.3   Sensitivity Analysis

The results of the factorial analysis are presented in Table 5:5 below and expressed in terms of the top 5% volume.

Material Law	Alpha	CT	Bone		Cement	
			Octahedral Shear Strain	E11	Von Mises Stress	E11
Keller	0.1	-2%	0.0065	0.0023	9.1	0.0009
		2%	0.00664	0.002464	8.80	0.00104
	5	0	0.006	0.0025	8.9	0.00092
	20	-2%	0.0069	0.00312	9.2	0.00146
		2%	0.006	0.00268	8.8	0.00074
Latypova	0.1	-2%	0.0037	0.0022	8.6	0.0011
		2%	0.0035	0.00159	8.5	0.00123
	5	0	0.0034	0.00184	9.6	0.00124
	20	-2%	0.0036	0.0018	8.4	0.00097
		2%	0.0033	0.00169	8.3	0.00114

Table 5:5: Results of Factorial Analysis.

The measured octahedral shear strains respectively axial strains (E11) of the models constructed using Keller's Law were larger than those using Latypova's Law: 1.8 difference factor resp. 1.45 difference factor.

	Material Law	CT Systematic Error	Filter Parameter	R^2
Bone Oct Strain	30%	-3%	-1%	0.99
	$p < 0.001$	$p = 0.11$	$p = 0.08$	
Bone axial strain	18%	-6%	4%	0.78
	$p < 0.01$	$p = 0.13$	$p = 0.2$	
Cement Von Mises Stress	3%	1%	1%	0.96
	$p < 0.01$	$p < 0.05$	$p < 0.05$	
Cement axial strain	3%	-3%	0%	0.07
	$p = 0.7$	$p = 0.5$	$p = 0.7$	

Table 5:6: Contributions of parameters to FE model outcome.

Using DOE analysis, bone octahedral shear strain and axial strain were highly sensitive to constitutive law: -30% and -18%, respectively. The bone strain was much less sensitive to the gaussian filter (4%) and CT error ($\leq 6\%$). Cement stress was slightly altered by all parameters ($\leq 3\%$). Cement strain was not significantly altered by the combinations of constitutive law and CT error ($\leq 10\%$) and by the combination of Gaussian filter and CT error ($\leq 10\%$). The analysis of variance revealed significant results for bone octahedral shear strain ($p < 0.001$), for bone axial strain ($p = 0.028$), for cement stress ($p = 0.006$), but not significant for cement strain ($p = 0.22$) (Table 5:6).

5.5   Discussion

Although total shoulder arthroplasty is an effective procedure to relieve pain and restore shoulder function, glenoid component loosening was listed as one of the most common complications. This failure may be due to several factors, amongst others: excessive cement stress or off-center loading on the glenoid component. The latter may be reinforced in the presence of subluxation. Overcorrected implants (OC) were suggested as an alternative to correct the postoperative subluxation but were never tested clinically nor biomechanically. The present work aimed to develop three patient-specific (PS) finite element (FE) models in order to assess their potential by answering the two research questions: 1) Do overcorrected implants reduce posterior sub-luxation? And 2) Do they transfer excessive stresses to the cement? First results suggest that OC implants indeed reduce the posterior subluxation without overconstraining the cement and the bone.

The PS FE models were based on CT images of patients planned for aTSA. One FE model simulated the im-planted prostheses (STD), and the second one contained the same geometry but with the OC implant. Pa-tient-specific (PS) loading from a MSM was applied to the implants. Four load cases were simulated and cement von Mises stress, bone compressive strain and humeral head subluxation were investigated.

A uniform cement thickness was added instead of a segemted layer because of the difficutly to distinguish the diffused cement and the trabeculae on the CT data.

Excessive cement stress was reported to initiate microcracks, leading to cement damage and eventually in-stability and glenoid implant loosening [54,65,159]. The literature reports different values of critical cement stress ranging between 4 and 14 MPa [54,66,165–168]. Thus, a middle value of 7 MPa as critical stress limit was chosen for this study. Using an OC implant design did not influence the volume of cement above this fatigue limit. Although peak stresses may have been larger than 7 MPa, its proportion was not significant (less than 0.1% for all simulated load cases and across all patients).

When OC implants were used, the volume of bone above the elastic limit of 1% was reduced for all load cases and for patients P1 and P3 for all load cases, but not for patient P2 at load case F1. This is probably due to the force's orientation for this patient which points in the antero-superior quadrant, while the prosthesis is posteriorly overcorrected. Moreover, for this specific case, a more restrictive humerus-glenoid surface inter-action was applied: while for all other cases, humerus-glenoid were allowed to separate during the move-ment, this was not the case for this case due to instability of the numerical model. This probably induced more compression on the glenoid implant and bone.

Posterior subluxation was reduced for most cases and for most patients, which is essential for such worst-case scenarios. However, this OC design moves towards an anterior subluxation. This was expected due to the form of the implant and to the direction of the loads simulated.

Although worst-case scenarios were chosen for the load cases, using an OC design reduced the eccentricity of the humeral head with respect to the glenoid implant, thus enabling a more concentric loading and reducing the rocking horse effect risk. The latter being defined as component instability due to off-center loading [12,14,20].

The conducted sensitivity analysis showed that the trabecular bone constitutive law had the most considerable impact on bone strain, while cement strain was nearly not altered. Our study helped identify sources of highest uncertainties in a multi-step PS model generation and showed that the CT imaging process is sufficiently accurate, while efforts need to be focused on a validated constitutive law of trabecular bone.

The present study overcame two of the major limitations associated with PS FE modeling [5] : first the lack of PS loading due to the complexity of sourcing the in-vivo loading by including PS loading and simulating different activities of daily living from a validated MSM [149]. Second, the lack of validation was overcome using a CT-to-FE workflow which was verified for displacements. Moreover, this study replicated planned implant placement for each patient, making the FE model as PS as possible.

A number of other limitations need to be acknowledged: First, the boundary conditions applied on the glenoid bone were overly simplified: there is no account for muscle or tendon stabilization. However, as stated in a recent review about FE modeling of shoulder arthroplasty [5], one of the major limitations of all cited studies was the lack of a correct representation of the most important anatomical structures of the musculoskeletal shoulder system. Additionally, a 0.3 friction coefficient was applied between the humeral head and glenoid implant, while the reported value for wet sliding of Titanium on UHMWPE is 0.2 and 0.4 for dry sliding [169,170]. Using a friction coefficient of 0.2 and allowing the surfaces to separate induced luxation for most load cases. Moreover, the number of patients and load cases simulated was not statistically strong enough. This is mainly due to the complexity of the patient-specific CT-to-FE model workflow. More patients and load cases need to be further investigated to establish the superiority of the OC design correctly.

To conclude, this study presented an elaborated PS FE model, including rotator cuff muscle deficiencies and PS loading, which, to the author's knowledge, has never been accounted for in patient-specific modeling of aTSA. Moreover, although the comparative tests were only performed on three patients, these preliminary results suggest that overcorrected implants are promising with respect to posterior subluxation, cement stress and bone compressive strain reduction. Further analyses with more patients and more daily living activities still need to be performed to confirm these conclusions.

5.6   Supplementary Material

5.6.1   Bone Material Mapping using Gaussian window

The bone mechanical properties are directly related to the bone mineral density (BMD), which in turn can be related to the grayscale (HU) values measured from the CT images. In order to use density-elasticity relationships, a calibration phantom was used to relate HU to density values at each integration point. A MATLAB script was used to assign HU value to each mesh element. Depending on the mesh density and the CT resolution, a single voxel might not relate to a single mesh element but to several of them. In addition, the HU values at a certain node might not be representative of the density of the area delimited by the element. This situation becomes more evident in areas with high contrast (i.e. trabecular to cortical bone boundary). In order to correct that, the script takes into account the voxels surrounding the node location to a distance (d) defined by the user. The density value at each integration point was then calculated by considering a Gaussian distribution of the HU values of the surrounding pixels that were included in the distance d. In other words, the pixels which were located far from the node had smaller weight than those located close to it. Such Gaussian distribution was implemented in the script by using the built-in MATLAB function $gausswin(N; \alpha)$, where α, called width factor [171], is proportional to the reciprocal of the standard deviation (σ) as shown in Eq.5:3 and Eq. 5:4 and N represented the number of points considered in the build-in function. The sensitivity of the FE model was performed with repsect to using different distance (d) in millimeters and alpha parameters of the Gaussian function.

$$\sigma = \frac{N-1}{2 * \alpha}$$

Equation 5:3: Standard deviation in Gaussian function.

$$y = e^{-\frac{1}{2} * (\frac{N}{\sigma})^2}$$

Equation 5:4: Gaussian window function
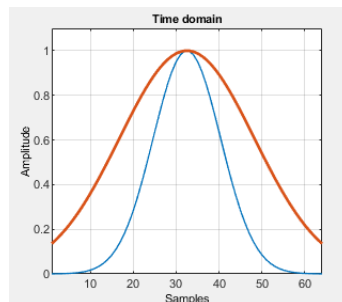
Figure 5:9 Difference between using a smaller or larger alpha factor in the Gaussian function.

(Image courtesy of https://ch.mathworks.com/help/signal/ref/sigwin.gausswin-class.html, [171])

5.6.2   Mesh convergence

Mesh convergence analysis was conducted for both bone and cement meshes: top 5%, 1% and 0.1% values for cement Max and Min Principal stress and bone Minimum principal strain were calculated for different mesh sizes.
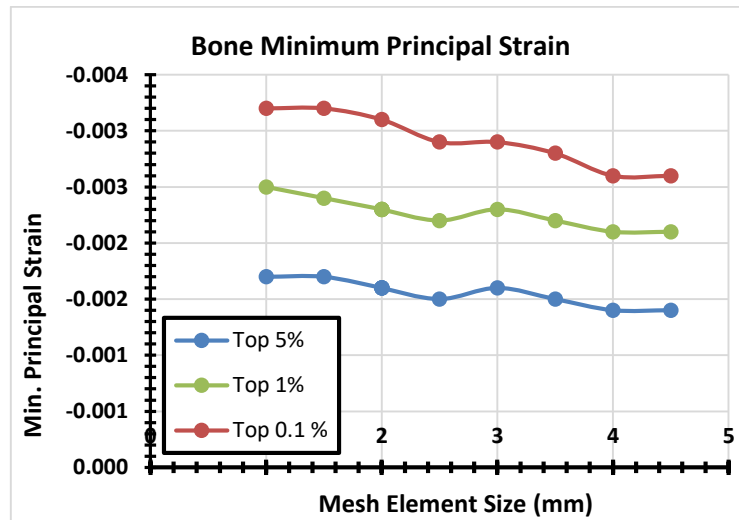
Figure 5:10 Bone minimum principal strain for varying mesh size.
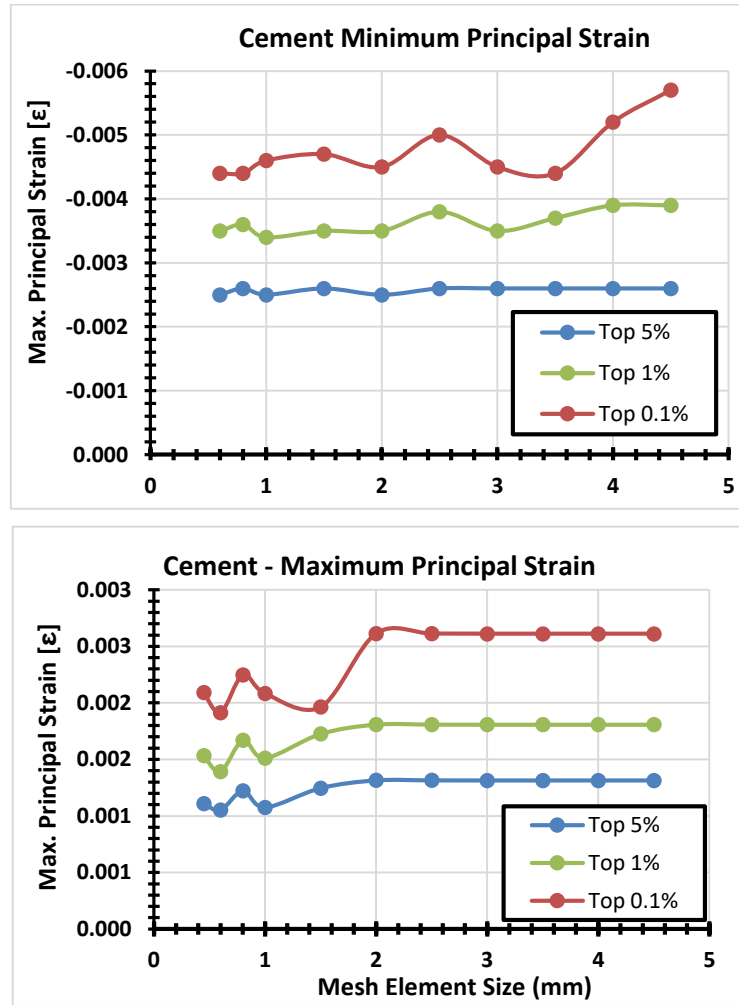
Figure 5:11 Cement minimum (top) and maximum (bottom) principal strain for varying mesh size.

Chapter 6   Conclusion

6.1   Achieved results

This thesis was motivated by the following clinical research question: what is the biomechanical advantage of overcorrected glenoid implants in the context of anatomical total shoulder arthroplasty (aTSA)? To answer this question, a shoulder simulation framework was developed and contains the following building blocks: 1) a procedure to convert preoperative CT data into patient-specific finite element (FE) models of their aTSA, 2) a patient-specific musculoskeletal model (MSM) that estimated the glenohumeral joint reaction forces during seven activities of daily living, 3) an experimental set-up was developed that measured displacements and deformations of the glenoid bone after aTSA under 1500 N axial loading thanks to Digital Volume Correlation (DVC) method. This set-up achieved 694.3 µε accuracy and 440.3 µε precision while displacement random error was 6.1 µm. 4) A bone material law to evaluate the behavior of novel prosthetic designs in a simulated environment was validated. With help of five specimen-specific FE models replicating the experiment, they predicted displacements with a coefficient of determination of R^2 = 1.0 and slope =1. The strain measurements were however poorly replicated (R^2 = 0.28-0.37 and slope = 0.51-0.70). Using these findings to create three patient-specific FE models comparing overcorrected and standard glenoid implants for patients planned for aTSA, the shoulder simulation framework developed in this thesis indicated that overcorrected glenoid implants might present a biomechanical benefit without adverse effect for the implant fixation. This preliminary result needs however to be further analyzed with alternative implant designs, to confirm a potential clinical interest.

The novelty of this work resides first in the development of a micro-CT – DVC method to measure bone deformation and its elaborated error quantification. Although the DVC technique is more and more used, its use in shoulder studies has been very limited until now. To our knowledge, only two groups have such a set-up [73,74] and only one of them published a study on glenoid deformation after aTSA [74]. The second novelty of this thesis is the validation of the specimen-specific FE model based on the experimentally measured displacements. The present study is the second to publish FE model-predicted displacements and strains

versus experimentally measured displacements and strains on implanted glenoid bone. Lastly, having included patient-specific data into our FE models adds to the novelty of the present work. In the following sections, the limitations as well as the perspectives for future works are presented.

6.2 Future development

6.2.1 Workflow CT to FE

The main challenges associated with the developed CT to FE model workflow lie in the complexity and multitude of steps required: Indeed, a combination of five software was necessary and some of the steps required intensive manual labor such as the rigid registration of preoperative to postoperative images. For future use, these steps should be automated to strengthen repeatability.

Although our specimen-specific and patient-specific FE models used key anthropometric data for glenohumeral stability, such as glenoid orientation and bone density, they still lack the contribution of further stabilizing soft tissues, such as rotator cuff muscles [5] and passive stabilizers such as glenohumeral capsule and both subacromial and subcoracoid bursae and the ligaments, especially the coracoacromial ligament which avoids humeral head from superior displacement [172].

An important aspect in bone modeling is the validity of the constitutive law. Although many laws were proposed, there is still no consensus as to the optimal one [5,136,162]. The present work identified four constitutive material laws with different parameters, to find the best replication of measured displacement field. A logical next step would be to test more than three specimens, in order to confirm the suitability of these material laws. Moreover, the partial volume effect needs to be addressed. A possible line of action might be to assign to the elements located at the outer surface of the bone an HU values averaged from HU values of neighboring elements; similar to what has been proposed in Knowles et al [76].

Moreover, bone anisotropy associated with trabecular structure is reported to affect stress and strain predictions of patient-specific numerical models [19,173]. Since it cannot be sufficiently evaluated from clinical CT scan, it should be derived differently. To account for bone anisotropy, we might use micro-CT scan of several specimens, extract the bone anisotropy for each and assign an averaged value, that could me mapped to the patient-specific FE model [173]. Alternatively, machine learning algorithms could be developed for this prediction. For example, the algorithm would have access to a database of μCT scans of scapulae, each of the scapulae would have assigned local anisotropy values. The algorithm would "get trained" on this database. Then, it would be able to assign anisotropy values to patient's glenoid bone from CT data and thus increase the reliability of the FE model developed in this thesis.

6.2.2 DVC experimental set-up

The non-invasive experimental set-up developed in this work to measure displacement and bone deformation under loading is one of the first to be used for the glenoid bone. Although it enabled us to study glenoid bone deformation under loading, the number of specimens studied should be extended to assess the preliminary observations. For three specimens analysed here, central loading was applied at 500 N, 750 N then 1500 N. We should replicate the experiment on more samples, but also with different loading conditions, such as controlled eccentric loading and different loading amplitudes. Possible future exploration might be to investigate how the bone deformations behave for increasing loads or if the bone constitutive material law used in the specimen-specific model was appropriate for all of the three loading cases, and for both the elastic deformation range (less than 1% compressive strain) and for the plastic deformation strain tested.

Another interesting development would be to use other available DVC software such as BoneDVC [81,84] in order to compare the displacement and stain predicted by both software.

6.2.3 Clinical application

The overcorrected implants investigated in the present study showed functional improvements by reducing the posterior subluxation without endangering the underlying bone and cement. However, this study was only applied to three patients and thus no statistical analysis was performed. More patient-specific models need to be created and more activities of daily living loading cases should be investigated to confirm our preliminary findings. Lastly, as shown in the results section of chapter 5, an overcorrection of 10° might be too severe, as it may induce anterior subluxation. Therefore, smaller overcorrection angles could be investigated to avoid anterior subluxation.

An interesting future step would be to compare the predictions of the patient-specific models with the measurements of a shoulder robotic simulator [145]. This robotic simulator was used to investigate glenohumeral subluxation using loaded glenoid prostheses during three activities of daily living. It would require to create patient-specific FE models of patients after aTSA, and use the same patients' characteristics with the robotic simulator, to compare humeral head displacement in the same loading conditions. Given the availability of the aTSA registry of the local university hospital (CHUV), a large number of comparative tests could be performed, and associated to surgery outcome.

To conclude, the different parts of the framework developed in this work could be integrated and automatized, to replicate patients more quickly. It would provide large data for investigating research questions with statistical analyses, and it might also be integrated in a clinical environment, within existing preoperative software. For example, when a patient is planned for aTSA, a preoperative CT scan is routinely performed.

This CT scan could be used for three applications: first, to the surgical planning software, second, to a preparation platform for MSM and third to the FE software in order to create a patient-specific FE model.

The surgeon would plan the surgery following their usual protocol, selecting the implant design and positioning in the glenoid bone. The preparation platform would use the planned glenoid implant orientations and measure the PCSA for each of the rotator cuff muscles from the CT scan, and feed them into the MSM. The later would predict typical glenohumeral joint forces during activities of daily living. The patient-specific FE model would be created using the bone densities extracted from the CT, the positioning of the implant for the preoperative software, and the forces obtained from the MSM. Finally, glenohumeral stability and bone strain would be estimated. These computer predictions could be used by the surgeon to refine the preoperative planning and select the optimal implant design and surgical technique (Figure 6:1).
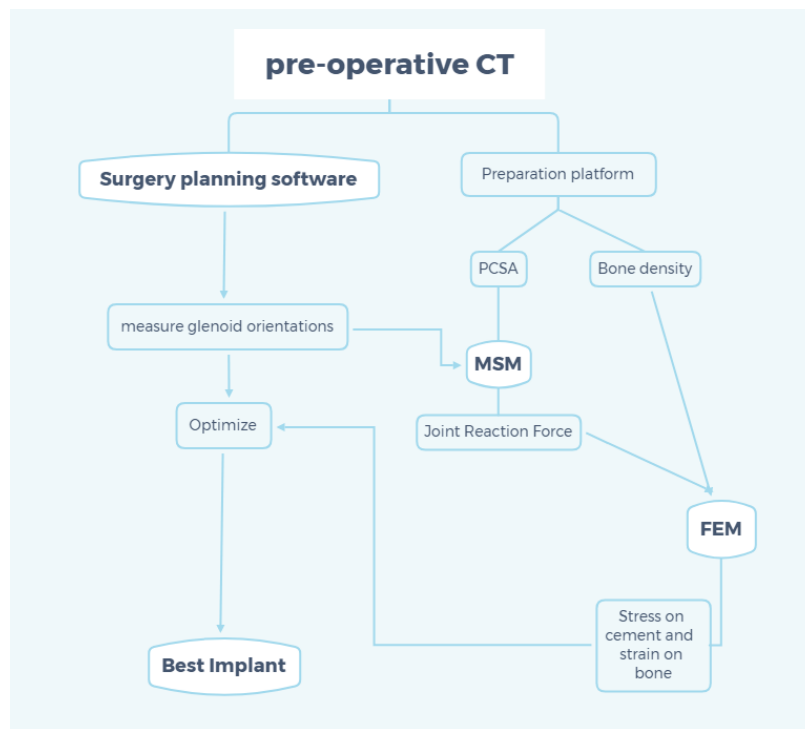

Figure 6:1 Clinical application.

References

[1] "Shoulder," Physiopedia [Online]. Available: https://www.physio-pedia.com/Shoulder. [Accessed: 07-Oct-2020].

[2] 2020, "Shoulder," Wikipedia.

[3] Ahir, S. P., Walker, P. S., Squire-Taylor, C. J., Blunn, G. W., and Bayley, J. I. L., 2004, "Analysis of Glenoid Fixation for a Reversed Anatomy Fixed-Fulcrum Shoulder Replacement," Journal of Biomechanics, **37**(11), pp. 1699–1708.

[4] Gupta, S., and van der Helm, F. C. T., 2004, "Load Transfer across the Scapula during Humeral Abduction," Journal of Biomechanics, **37**(7), pp. 1001–1009.

[5] Zheng, M., Zou, Z., Bartolo, P. J., Peach, C., and Ren, L., 2017, "Finite Element Models of the Human Shoulder Complex: A Review of Their Clinical Implications and Modelling Techniques," International journal for numerical methods in biomedical engineering, **33**(2).

[6] Netgen, "Polyarthrite rhumatoïde : ce qui a changé et ce qu'il reste encore à faire," Revue Médicale Suisse [Online]. Available: https://www.revmed.ch/RMS/2019/RMS-N-641/Polyarthrite-rhumatoide-ce-qui-a-change-et-ce-qu-il-reste-encore-a-faire. [Accessed: 07-Oct-2020].

[7] 2020, "Rheumatoid Arthritis," Wikipedia.

[8] Chillemi, C., and Franceschini, V., 2013, "Shoulder Osteoarthritis," Arthritis, **2013**, p. 370231.

[9] Bruce C Anderson, M. D., 2014, "Glenohumeral Osteoarthritis."

[10] "Shoulder Osteoarthritis (Degenerative Arthritis of the Shoulder)."

[11] Office fédéral de la statistique OFS, 2013, "Office Fédéral de La Statistique Communiqué de Presse 2013."

[12] Virani, N. A., Harman, M., Li, K., Levy, J., Pupello, D. R., and Frankle, M. A., 2008, "In Vitro and Finite Element Analysis of Glenoid Bone/Baseplate Interaction in the Reverse Shoulder Design," Journal of shoulder and elbow surgery / American Shoulder and Elbow Surgeons ... [et al.], **17**(3), pp. 509–21.

[13] 2020, "Bone," Wikipedia.

[14] Couteau, B., Mansat, P., Estivalezes, E., Darmana, R., Mansat, M., and Egan, J., 2001, "Finite Element Analysis of the Mechanical Behavior of a Scapula Implanted with a Glenoid Prosthesis," Clinical biomechanics, **16**(7), pp. 566–75.

[15] Netgen, "Arthroplastie de l'épaule : le point en 2014," Revue Médicale Suisse [Online]. Available: https://www.revmed.ch/RMS/2014/RMS-N-455/Arthroplastie-de-l-epaule-le-point-en-2014. [Accessed: 07-Oct-2020].

[16] Walch, G., Young, A. A., Melis, B., Gazielly, D., Loew, M., and Boileau, P., 2011, "Results of a Convex-Back Cemented Keeled Glenoid Component in Primary Osteoarthritis: Multicenter Study with a Follow-up Greater than 5 Years," Journal of Shoulder and Elbow Surgery, **20**(3), pp. 385–394.

[17] Mueller, U., Braun, S., Schroeder, S., Schroeder, M., Sonntag, R., Jaeger, S., and Kretzer, J. P., 2017, "Influence of Humeral Head Material on Wear Performance in Anatomic Shoulder Joint Arthroplasty," J Shoulder Elb Surg, **26**(10), pp. 1756–1764.

[18] Budinski, K. G., 1991, "Tribological Properties of Titanium Alloys," Wear, **151**(2), pp. 203–217.

[19] Chevalier, Y., Santos, I., Muller, P. E., and Pietschmann, M. F., 2016, "Bone Density and Anisotropy Affect Periprosthetic Cement and Bone Stresses after Anatomical Glenoid Replacement: A Micro Finite Element Analysis," Journal of biomechanics, **49**(9), pp. 1724–33.

[20] Hopkins, A. R., Hansen, U. N., Bull, A. M. J., Emery, R., and Amis, A. A., 2008, "Fixation of the Reversed Shoulder Prosthesis," Journal of Shoulder and Elbow Surgery, **17**(6), pp. 974–980.

[21] Sabesan, V. J., Ackerman, J., Sharma, V., Baker, K. C., Kurdziel, M. D., and Wiater, J. M., 2015, "Glenohumeral Mismatch Affects Micromotion of Cemented Glenoid Components in Total Shoulder Arthroplasty," Journal of shoulder and elbow surgery / American Shoulder and Elbow Surgeons ... [et al.], **24**(5), pp. 814–22.

[22] Wee, H., Armstrong, A. D., Flint, W. W., Kunselman, A. R., and Lewis, G. S., 2015, "Peri-Implant Stress Correlates with Bone and Cement Morphology: Micro-FE Modeling of Implanted Cadaveric Glenoids," Journal of orthopaedic research : official publication of the Orthopaedic Research Society, **33**(11), pp. 1671–9.

[23] Lewis, G. S., Brenza, J. B., Paul, E. M., and Armstrong, A. D., 2016, "Construct Damage and Loosening around Glenoid Implants: A Longitudinal Micro-CT Study of Five Cadaver Specimens," Journal of orthopaedic research : official publication of the Orthopaedic Research Society, **34**(6), pp. 1053–60.

[24] "Shoulder Subluxation," Physiopedia [Online]. Available: https://www.physio-pedia.com/Shoulder_subluxation. [Accessed: 16-Oct-2020].

[25] Jacxsens, M., Van Tongel, A., Henninger, H. B., Tashjian, R. Z., and De Wilde, L., 2017, "The Three-Dimensional Glenohumeral Subluxation Index in Primary Osteoarthritis of the Shoulder," Journal of Shoulder and Elbow Surgery, **26**(5), pp. 878–887.

[26] Walch, G., Badet, R., Boulahia, A., and Khoury, A., 1999, "Morphologic Study of the Glenoid in Primary Glenohumeral Osteoarthritis," The Journal of arthroplasty, **14**(6), pp. 756–60.

[27] Walch, G., Boulahia, A., Boileau, P., and Kempf, J. F., 1998, "Primary Glenohumeral Osteoarthritis: Clinical and Radiographic Classification," Acta Orthopaedica Belgica, **64**(SUPPL. 2), pp. 46–52.

[28] Sabesan, V. J., Callanan, M., Youderian, A., and Iannotti, J. P., 2014, "3D CT Assessment of the Relationship between Humeral Head Alignment and Glenoid Retroversion in Glenohumeral Osteoarthritis," J Bone Joint Surg Am, **96**(8), p. e64.

[29] Terrier, A., Ston, J., and Farron, A., 2015, "Importance of a Three-Dimensional Measure of Humeral Head Subluxation in Osteoarthritic Shoulders," J Shoulder Elb Surg, **24**(2), pp. 295–301.

[30] Bercik, M. J., Kruse, K., Yalizis, M., Gauci, M.-O., Chaoui, J., and Walch, G., 2016, "A Modification to the Walch Classification of the Glenoid in Primary Glenohumeral Osteoarthritis Using Three-Dimensional Imaging," Journal of Shoulder and Elbow Surgery, **25**(10), pp. 1601–1606.

[31] Karelse, A., Van Tongel, A., Verstraeten, T., Poncet, D., and De Wilde, L. F., 2015, "Rocking-Horse Phenomenon of the Glenoid Component: The Importance of Inclination," J Shoulder Elb Surg, **24**(7), pp. 1142–8.

[32] Dao, T. T., 2016, "Rigid Musculoskeletal Models of the Human Body Systems: A Review," Journal of Musculoskeletal Research, **19**(03), p. 1630001.

[33] Prinold, J. A., Masjedi, M., Johnson, G. R., and Bull, A. M., 2013, "Musculoskeletal Shoulder Models: A Technical Review and Proposals for Research Foci," Proceedings of the Institution of Mechanical Engineers. Part H, Journal of engineering in medicine, **227**(10), pp. 1041–57.

[34] Duprey, S., Naaim, A., Moissenet, F., Begon, M., and Chèze, L., 2017, "Kinematic Models of the Upper Limb Joints for Multibody Kinematics Optimisation: An Overview," Journal of Biomechanics, **62**, pp. 87–94.

[35] Bolsterlee, B., Vardy, A. N., van der Helm, F. C., and Veeger, H. E., 2015, "The Effect of Scaling Physiological Cross-Sectional Area on Musculoskeletal Model Predictions," Journal of biomechanics, **48**(10), pp. 1760–8.

[36] van der Helm, F. C. T., 1994, "Analysis of the Kinematic and Dynamic Behavior of the Shoulder Mechanism," Journal of Biomechanics, **27**(5), pp. 527–550.

[37] van der Helm, F. C. T., 1994, "A Finite Element Musculoskeletal Model of the Shoulder Mechanism," Journal of Biomechanics, **27**(5), pp. 551–569.

[38] Garner, B. A., and Pandy, M. G., 1999, "A Kinematic Model of the Upper Limb Based on the Visible Human Project (VHP) Image Dataset," Computer methods in biomechanics and biomedical engineering, **2**(2), pp. 107–124.

[39] Garner, B. A., and Pandy, M. G., 2001, "Musculoskeletal Model of the Upper Limb Based on the Visible Human Male Dataset," Computer methods in biomechanics and biomedical engineering, **4**(2), pp. 93–126.

[40] Hogfors, C., Peterson, B., Sigholm, G., and Herberts, P., 1991, "Biomechanical Model of the Human Shoulder Joint--II. The Shoulder Rhythm," Journal of biomechanics, **24**(8), pp. 699–709.

[41] Damsgaard, M., Rasmussen, J., Christensen, S. T., Surma, E., and de Zee, M., 2006, "Analysis of Musculo-skeletal Systems in the AnyBody Modeling System," Simulation Modelling Practice and Theory, **14**(8), pp. 1100–1111.

[42] Holzbaur, K. R. S., Murray, W. M., and Delp, S. L., 2005, "A Model of the Upper Extremity for Simulating Musculoskeletal Surgery and Analyzing Neuromuscular Control," Annals of biomedical engineering, **33**(6), pp. 829–840.

[43] Charlton, I. W., and Johnson, G. R., 2006, "A Model for the Prediction of the Forces at the Glenohumeral Joint," Proceedings of the Institution of Mechanical Engineers. Part H, Journal of engineering in medicine, **220**(8), pp. 801–12.

[44] Dickerson, C. R., Chaffin, D. B., and Hughes, R. E., 2007, "A Mathematical Musculoskeletal Shoulder Model for Proactive Ergonomic Analysis," Computer methods in biomechanics and biomedical engineering, **10**(6), pp. 389–400.

[45] Blana, D., Hincapie, J. G., Chadwick, E. K., and Kirsch, R. F., 2008, "A Musculoskeletal Model of the Upper Extremity for Use in the Development of Neuroprosthetic Systems," Journal of biomechanics, **41**(8), pp. 1714–21.

[46] Quental, C., Folgado, J., Ambrósio, J., and Monteiro, J., 2012, "A Multibody Biomechanical Model of the Upper Limb Including the Shoulder Girdle," Multibody System Dynamics, **28**(1–2), pp. 83–108.

[47] Terrier, A., Reist, A., Vogel, A., and Farron, A., 2007, "Effect of Supraspinatus Deficiency on Humerus Translation and Glenohumeral Contact Force during Abduction," Clinical biomechanics, **22**(6), pp. 645–51.

[48] Engelhardt, C., Malfroy Camine, V., Ingram, D., Mullhaupt, P., Farron, A., Pioletti, D., and Terrier, A., 2015, "Comparison of an EMG-Based and a Stress-Based Method to Predict Shoulder Muscle Forces," Computer methods in biomechanics and biomedical engineering, **18**(12), pp. 1272–9.

[49] Bergmann, G., Graichen, F., Bender, A., Rohlmann, A., Halder, A., Beier, A., and Westerhoff, P., 2011, "In Vivo Gleno-Humeral Joint Loads during Forward Flexion and Abduction," Journal of biomechanics, **44**(8), pp. 1543–52.

[50] Duprey, S., Naaim, A., Moissenet, F., Begon, M., and Chèze, L., 2017, "Kinematic Models of the Upper Limb Joints for Multibody Kinematics Optimisation: An Overview," J Biomech, **62**, pp. 87–94.

[51] Taylor, M., and Prendergast, P. J., 2015, "Four Decades of Finite Element Analysis of Orthopaedic Devices: Where Are We Now and What Are the Opportunities?," Journal of biomechanics, **48**(5), pp. 767–78.

[52] Cuff, D. J., Virani, N. A., Levy, J., Frankle, M. A., Derasari, A., Hines, B., Pupello, D. R., Cancio, M., and Mighell, M., 2008, "The Treatment of Deep Shoulder Infection and Glenohumeral Instability with Debridement, Reverse Shoulder Arthroplasty and Postoperative Antibiotics," The Journal of bone and joint surgery. British volume, **90**(3), pp. 336–42.

[53] Hopkins, A. R., Hansen, U. N., Amis, A. A., and Emery, R., 2004, "The Effects of Glenoid Component Alignment Variations on Cement Mantle Stresses in Total Shoulder Arthroplasty," Journal of shoulder and elbow surgery / American Shoulder and Elbow Surgeons ... [et al.], **13**(6), pp. 668–75.

[54] Lacroix, D., Murphy, L. A., and Prendergast, P. J., 2000, "Three-Dimensional Finite Element Analysis of Glenoid Replacement Prostheses: A Comparison of Keeled and Pegged Anchorage Systems," Journal of biomechanical engineering, **122**(4), pp. 430–6.

[55] Mansat, P., Briot, J., Mansat, M., and Swider, P., 2007, "Evaluation of the Glenoid Implant Survival Using a Biomechanical Finite Element Analysis: Influence of the Implant Design, Bone Properties, and Loading Location," Journal of shoulder and elbow surgery / American Shoulder and Elbow Surgeons ... [et al.], **16**(3 Suppl), pp. S79-83.

[56] Permeswaran, V. N., Goetz, J. E., Rudert, M. J., Hettrich, C. M., and Anderson, D. D., 2016, "Cadaveric Validation of a Finite Element Modeling Approach for Studying Scapular Notching in Reverse Shoulder Arthroplasty," Journal of biomechanics.

[57] Terrier, A., Brighenti, V., Pioletti, D. P., and Farron, A., 2012, "Importance of Polyethylene Thickness in Total Shoulder Arthroplasty: A Finite Element Analysis," Clinical biomechanics, **27**(5), pp. 443–8.

[58] Yongpravat, C., Kim, H. M., Gardner, T. R., Bigliani, L. U., Levine, W. N., and Ahmad, C. S., 2013, "Glenoid Implant Orientation and Cement Failure in Total Shoulder Arthroplasty: A Finite Element Analysis," J Shoulder Elb Surg, **22**(7), pp. 940–7.

[59] Friedman, R. J., LaBerge, M., Dooley, R. L., and O'Hara, A. L., 1992, "Finite Element Modeling of the Glenoid Component: Effect of Design Parameters on Stress Distribution," Journal of Shoulder and Elbow Surgery, **1**(5), pp. 261–270.

[60] Murphy, L. A., and Prendergast, P. J., 2005, "Acromion-Fixation of Glenoid Components in Total Shoulder Arthroplasty," Journal of Biomechanics, **38**(8), pp. 1702–1711.

[61] Quental, C., Fernandes, P. R., Monteiro, J., and Folgado, J., 2014, "Bone Remodelling of the Scapula after a Total Shoulder Arthroplasty," Biomech Model Mechanobiol, **13**(4), pp. 827–838.

[62] Stone, K. D., Grabowski, J. J., Cofield, R. H., Morrey, B. F., and An, K. N., 1999, "Stress Analyses of Glenoid Components in Total Shoulder Arthroplasty," Journal of Shoulder and Elbow Surgery, **8**(2), pp. 151–158.

[63] Terrier, A., Merlini, F., Pioletti, D. P., and Farron, A., 2009, "Comparison of Polyethylene Wear in Anatomical and Reversed Shoulder Prostheses," The Journal of Bone and Joint Surgery. British volume, **91-B**(7), pp. 977–982.

[64] Gupta, S., van der Helm, F. C. T., and van Keulen, F., 2004, "The Possibilities of Uncemented Glenoid Component—a Finite Element Study," Clinical Biomechanics, **19**(3), pp. 292–302.

[65] Terrier, A., Büchler, P., and Farron, A., 2005, "Bone–Cement Interface of the Glenoid Component: Stress Analysis for Varying Cement Thickness," Clinical Biomechanics, **20**(7), pp. 710–717.

[66] Lacroix, D., and Prendergast, P. J., 1997, "Stress Analysis of Glenoid Component Designs for Shoulder Arthroplasty," Proc Inst Mech Eng H, **211**(6), pp. 467–474.

[67] Terrier, A., Büchler, P., and Farron, A., 2006, "Influence of Glenohumeral Conformity on Glenoid Stresses after Total Shoulder Arthroplasty," Journal of Shoulder and Elbow Surgery, **15**(4), pp. 515–520.

[68] Campoli, G., Bolsterlee, B., van der Helm, F., Weinans, H., and Zadpoor, A. A., 2014, "Effects of Densitometry, Material Mapping and Load Estimation Uncertainties on the Accuracy of Patient-Specific Finite-Element Models of the Scapula," Journal of the Royal Society, Interface, **11**(93), p. 20131146.

[69] Sukjamsri, C., Geraldes, D. M., Gregory, T., Ahmed, F., Hollis, D., Schenk, S., Amis, A., Emery, R., and Hansen, U., 2015, "Digital Volume Correlation and Micro-CT: An in-Vitro Technique for Measuring Full-Field Interface Micromotion around Polyethylene Implants," Journal of biomechanics, **48**(12), pp. 3447–54.

[70] Allred, J. J., Flores-Hernandez, C., Hoenecke, H. R., and D'Lima, D. D., 2016, "Posterior Augmented Glenoid Implants Require Less Bone Removal and Generate Lower Stresses: A Finite Element Analysis," Journal of Shoulder and Elbow Surgery, **25**(5), pp. 823–830.

[71] Pomwenger, W., Entacher, K., Resch, H., and Schuller-Götzburg, P., 2019, "Influence of Glenoid Implant Depth on the Bone–Polymethylmethacrylate Interface," Obere Extremität.

[72] Comenda, M., Quental, C., Folgado, J., Sarmento, M., and Monteiro, J., 2019, "Bone Adaptation Impact of Stemless Shoulder Implants: A Computational Analysis," Journal of Shoulder and Elbow Surgery, **28**(10), pp. 1886–1896.

[73] Kusins, J., Knowles, N., Ryan, M., Dall'Ara, E., and Ferreira, L., 2019, "Performance of QCT-Derived Scapula Finite Element Models in Predicting Local Displacements Using Digital Volume Correlation," Journal of the mechanical behavior of biomedical materials, **97**, pp. 339–345.

[74] Zhou, Y., Gong, C., Lewis, G. S., Armstrong, A. D., and Du, J., 2020, "3D Full-Field Biomechanical Testing of a Glenoid before and after Implant Placement," Extreme Mechanics Letters, **35**, p. 100614.

[75] Knowles, N. K., Carroll, M. J., Keener, J. D., Ferreira, L. M., and Athwal, G. S., 2016, "A Comparison of Normal and Osteoarthritic Humeral Head Size and Morphology," J Shoulder Elb Surg, **25**(3), pp. 502–9.

[76] Knowles, N. K., Kusins, J., Faieghi, M., Ryan, M., Dall'Ara, E., and Ferreira, L. M., 2019, "Material Mapping of QCT-Derived Scapular Models: A Comparison with Micro-CT Loaded Specimens Using Digital Volume Correlation," Annals of biomedical engineering.

[77] Kusins, J., Knowles, N., Columbus, M., Oliviero, S., Dall'Ara, E., Athwal, G. S., and Ferreira, L. M., 2020, "The Application of Digital Volume Correlation (DVC) to Evaluate Strain Predictions Generated by Finite Element Models of the Osteoarthritic Humeral Head," Ann Biomed Eng.

[78] Kusins, J., Knowles, N., Ryan, M., Dall'Ara, E., and Ferreira, L., 2020, "Full-Field Comparisons between Strains Predicted by QCT-Derived Finite Element Models of the Scapula and Experimental Strains Measured by Digital Volume Correlation," Journal of Biomechanics, **113**, p. 110101.

[79] Nuttall, D., Birch, A., Haines, J. E., Watts, A. C., and Trail, I. A., 2017, "Early Migration of a Partially Cemented Fluted Glenoid Component Inserted Using a Cannulated Preparation System," Bone Joint J, **99-B**(5), pp. 674–679.

[80] Bay, 1999, "Digital Volume Correlation: Three-Dimentional Strain Mapping Using X-Ray Tomography," Experimental Mechanics, **39 (1999)**, pp. 217–226.

[81] Dall'Ara, E., Peña-Fernández, M., Palanca, M., Giorgi, M., Cristofolini, L., and Tozzi, G., 2017, "Precision of Digital Volume Correlation Approaches for Strain Analysis in Bone Imaged with Micro-Computed Tomography at Different Dimensional Levels," Frontiers in Materials, **4**.

[82] Roberts, B. C., Perilli, E., and Reynolds, K. J., 2014, "Application of the Digital Volume Correlation Technique for the Measurement of Displacement and Strain Fields in Bone: A Literature Review," Journal of biomechanics, **47**(5), pp. 923–34.

[83] Christen, D., Levchuk, A., Schori, S., Schneider, P., Boyd, S. K., and Muller, R., 2012, "Deformable Image Registration and 3D Strain Mapping for the Quantitative Assessment of Cortical Bone Microdamage," Journal of the mechanical behavior of biomedical materials, **8**, pp. 184–93.

[84] Dall'Ara, E., Barber, D., and Viceconti, M., 2014, "About the Inevitable Compromise between Spatial Resolution and Accuracy of Strain Measurement for Bone Tissue: A 3D Zero-Strain Study," Journal of biomechanics, **47**(12), pp. 2956–63.

[85] Danesi, V., Tozzi, G., and Cristofolini, L., 2016, "Application of Digital Volume Correlation to Study the Efficacy of Prophylactic Vertebral Augmentation," Clinical biomechanics, **39**, pp. 14–24.

[86] Gillard, F., Boardman, R., Mavrogordato, M., Hollis, D., Sinclair, I., Pierron, F., and Browne, M., 2014, "The Application of Digital Volume Correlation (DVC) to Study the Microstructural Behaviour of Trabecular Bone during Compression," Journal of the mechanical behavior of biomedical materials, **29**, pp. 480–99.

[87] Giorgi, M., and Dall'Ara, E., 2018, "Variability in Strain Distribution in the Mice Tibia Loading Model: A Preliminary Study Using Digital Volume Correlation," Medical engineering & physics, **62**, pp. 7–16.

[88] Hussein, A. I., Barbone, P. E., and Morgan, E. F., 2012, "Digital Volume Correlation for Study of the Mechanics of Whole Bones," Procedia IUTAM, **4**, pp. 116–125.

[89] Liu, L., and Morgan, E. F., 2007, "Accuracy and Precision of Digital Volume Correlation in Quantifying Displacements and Strains in Trabecular Bone," Journal of biomechanics, **40**(15), pp. 3516–20.

[90] Oliviero, S., Giorgi, M., and Dall'Ara, E., 2018, "Validation of Finite Element Models of the Mouse Tibia Using Digital Volume Correlation," J Mech Behav Biomed Mater, **86**, pp. 172–184.

[91] Tozzi, G., Danesi, V., Palanca, M., and Cristofolini, L., 2016, "Elastic Full-Field Strain Analysis and Microdamage Progression in the Vertebral Body from Digital Volume Correlation," Strain.

[92] Palanca, M., Tozzi, G., Cristofolini, L., Viceconti, M., and Dall'Ara, E., 2015, "Three-Dimensional Local Measurements of Bone Strain and Displacement: Comparison of Three Digital Volume Correlation Approaches," Journal of biomechanical engineering, **137**(7).

[93] Tozzi, G., Dall'Ara, E., Palanca, M., Curto, M., Innocente, F., and Cristofolini, L., 2017, "Strain Uncertainties from Two Digital Volume Correlation Approaches in Prophylactically Augmented Vertebrae: Local Analysis on Bone and Cement-Bone Microstructures," Journal of the mechanical behavior of biomedical materials, **67**, pp. 117–126.

[94] Zhu, M. L., Zhang, Q. H., Lupton, C., and Tong, J., 2016, "Spatial Resolution and Measurement Uncertainty of Strains in Bone and Bone-Cement Interface Using Digital Volume Correlation," Journal of the mechanical behavior of biomedical materials, **57**, pp. 269–79.

[95] Madi, K., Tozzi, G., Zhang, Q. H., Tong, J., Cossey, A., Au, A., Hollis, D., and Hild, F., 2013, "Computation of Full-Field Displacements in a Scaffold Implant Using Digital Volume Correlation and Finite Element Analysis," Medical engineering & physics, **35**(9), pp. 1298–312.

[96] Comini, F., Palanca, M., Cristofolini, L., and Dall'Ara, E., 2019, "Uncertainties of Synchrotron MicroCT-Based Digital Volume Correlation Bone Strain Measurements under Simulated Deformation," Journal of Biomechanics, **86**, pp. 232–237.

[97] Cafeo, J., and Thacker, B., 2004, "Concepts and Terminology of Validation for Computational Solid Mechanics Models."

[98] Anderson, A. E., Ellis, B. J., and Weiss, J. A., 2007, "Verification, Validation and Sensitivity Studies in Computational Biomechanics," Computer methods in biomechanics and biomedical engineering, **10**(3), pp. 171–84.

[99] Henak, C. R., Anderson, A. E., and Weiss, J. A., 2013, "Subject-Specific Analysis of Joint Contact Mechanics: Application to the Study of Osteoarthritis and Surgical Planning," Journal of biomechanical engineering, **135**(2), p. 021003.

[100]   Saltelli, 2004, "Sensitivity Analysis," Wiley.

[101]   O'Rourke, D., Martelli, S., Bottema, M., and Taylor, M., 2016, "A Computational Efficient Method to Assess the Sensitivity of Finite-Element Models: An Illustration With the Hemipelvis," Journal of biomechanical engineering, **138**(12).

[102]   Clouthier, A. L., Hetzler, M. A., Fedorak, G., Bryant, J. T., Deluzio, K. J., and Bicknell, R. T., 2013, "Factors Affecting the Stability of Reverse Shoulder Arthroplasty: A Biomechanical Study," J Shoulder Elb Surg, **22**(4), pp. 439–44.

[103]   Dar, F. H., Meakin, J. R., and Aspden, R. M., 2002, "Statistical Methods in Finite Element Analysis," Journal of biomechanics, **35**(9), pp. 1155–61.

[104]   Ghezelbash, F., Shirazi-Adl, A., Arjmand, N., El-Ouaaid, Z., Plamondon, A., and Meakin, J. R., 2016, "Effects of Sex, Age, Body Height and Body Weight on Spinal Loads: Sensitivity Analyses in a Subject-Specific Trunk Musculoskeletal Model," Journal of biomechanics, **49**(14), pp. 3492–3501.

[105]   Lin, T. S., Tsai, F. D., Chen, C. Y., and Lin, L. W., 2013, "Factorial Analysis of Variables Affecting Bone Stress Adjacent to the Orthodontic Anchorage Mini-Implant with Finite Element Analysis," American journal of orthodontics and dentofacial orthopedics : official publication of the American Association of Orthodontists, its constituent societies, and the American Board of Orthodontics, **143**(2), pp. 182–9.

[106]   Malandrino, A., Planell, J. A., and Lacroix, D., 2009, "Statistical Factorial Analysis on the Poroelastic Material Properties Sensitivity of the Lumbar Intervertebral Disc under Compression, Flexion and Axial Rotation," Journal of biomechanics, **42**(16), pp. 2780–8.

[107]   Yao, J., Funkenbusch, P. D., Snibbe, J., Maloney, M., and Lerner, A. L., 2006, "Sensitivities of Medial Meniscal Motion and Deformation to Material Properties of Articular Cartilage, Meniscus and Meniscal Attachments Using Design of Experiments Methods," Journal of biomechanical engineering, **128**(3), pp. 399–408.

[108]   Malfroy Camine, V., Rudiger, H. A., Pioletti, D. P., and Terrier, A., 2016, "Full-Field Measurement of Micromotion around a Cementless Femoral Stem Using Micro-CT Imaging and Radiopaque Markers," Journal of biomechanics, **49**(16), pp. 4002–4008.

[109]   Gortchacow, M., Wettstein, M., Pioletti, D. P., Muller-Gerbl, M., and Terrier, A., 2012, "Simultaneous and Multisite Measure of Micromotion, Subsidence and Gap to Evaluate Femoral Stem Stability," Journal of biomechanics, **45**(7), pp. 1232–8.

[110]   Gortchacow, M., Wettstein, M., Pioletti, D. P., and Terrier, A., 2011, "A New Technique to Measure Micromotion Distribution around a Cementless Femoral Stem," Journal of biomechanics, **44**(3), pp. 557–60.

[111]   Klein, S., 2010, "Elastix: A Toolbox for Intensity-Based Medical Image Registration," IEEE TRANSACTIONS ON MEDICAL IMAGING, **VOL. 29, NO. 1**.

[112]   Singh, J. A., Sperling, J. W., and Cofield, R. H., 2011, "Revision Surgery Following Total Shoulder Arthroplasty: Analysis of 2,588 Shoulders over 3 Decades (1976–2008)," J Bone Joint Surg Br, **93**(11).

[113]   Morgan, E. F., 2001, "Dependence of Yield Strain of Human Trabecular Bone on Anatomic Site," Journal of biomechanics, **34**, pp. 569–577.

[114]   Panyasantisuk, J., Pahr, D. H., and Zysset, P. K., 2016, "Effect of Boundary Conditions on Yield Properties of Human Femoral Trabecular Bone," Biomechanics and modeling in mechanobiology, **15**(5), pp. 1043–53.

[115]   Bergmann, G. ; G. F. ; B. A. ; R. A. ; H. A. ; B. A. ; W. P., "Orthoload."

[116]   Brouwer, C. L., 2014, "The Effects of Computed Tomography Image Characteristics and Knot Spacing on the Spatial Accuracy of B-Spline Deformable Image Registration in the Head and Neck Geometry," Radiation Oncology, **9:169**.

[117]   Qiao Y, 2016, "Fast Automatic Step Size Estimation for Gradient Descent Optimization of Image Registration," IEEE TRANSACTIONS ON MEDICAL IMAGING, **35 n2**.

[118]   Fortunati, V., Verhaart, R. F., van der Lijn, F., Niessen, W. J., Veenland, J. F., Paulides, M. M., and van Walsum, T., 2013, "Tissue Segmentation of Head and Neck CT Images for Treatment Planning: A Multi-atlas Approach Combined with Intensity Modeling," Medical physics, **40**(7), p. 071905.

[119]   Pena Fernandez, M., Cipiccia, S., Dall'Ara, E., Bodey, A. J., Parwani, R., Pani, M., Blunn, G. W., Barber, A. H., and Tozzi, G., 2018, "Effect of SR-MicroCT Radiation on the Mechanical Integrity of Trabecular Bone Using in Situ Mechanical Testing and Digital Volume Correlation," Journal of the mechanical behavior of biomedical materials, **88**, pp. 109–119.

[120]   Klein, S., and Staring, M., 2015, "Elastix. The Manual. v4.8."

[121]   Boulanaache, Y., Becce, F., Farron, A., Pioletti, D. P., and Terrier, A., 2020, "Glenoid Bone Strain after Anatomical Total Shoulder Arthroplasty: In Vitro Measurements with Micro-CT and Digital Volume Correlation," Medical Engineering & Physics.

[122]   Schaffler, M. B., and Burr, D. B., 1988, "Stiffness of Compact Bone: Effects of Porosity and Density," Journal of biomechanics, **21**(1), pp. 13–6.

[123]   Rice, J. C., Cowin, S. C., and Bowman, J. A., 1988, "On the Dependence of the Elasticity and Strength of Cancellous Bone on Apparent Density," Journal of Biomechanics, **21**(2), pp. 155–168.

[124]   Keller, T. S., 1994, "Predicting the Compressive Mechanical-Behavior of Bone," Journal of biomechanics, **27**(9), pp. 1159–1168.

[125]   Büchler, P., Ramaniraka, N. A., Rakotomanana, L. R., Iannotti, J. P., and Farron, A., 2002, "A Finite Element Model of the Shoulder: Application to the Comparison of Normal and Osteoarthritic Joints," Clin Biomech (Bristol, Avon), **17**(9–10), pp. 630–639.

[126]   Morgan, E. F., Bayraktar, H. H., and Keaveny, T. M., 2003, "Trabecular Bone Modulus–Density Relationships Depend on Anatomic Site," Journal of biomechanics, **36**(7), pp. 897–904.

[127]   Gupta, S., and Dan, P., 2004, "Bone Geometry And Mechanical Properties Of The Human Scapula Using Computed Tomography Data," Trends Biomater. Artif. Organs, **Vol.17**(2), p. pp 61-70.

[128]   Latypova, A., Maquer, G., Elankumaran, K., Pahr, D., Zysset, P., Pioletti, D. P., and Terrier, A., 2016, "Identification of Elastic Properties of Human Patellae Using Micro-Finite Element Analysis," Journal of biomechanics, **49**(13), pp. 3111–3115.

[129]   Knowles, N. K., G. Langohr, G. D., Faieghi, M., Nelson, A., and Ferreira, L. M., 2019, "Development of a Validated Glenoid Trabecular Density-Modulus Relationship," Journal of the Mechanical Behavior of Biomedical Materials, **90**, pp. 140–145.

[130]   Schileo, E., Dall'Ara, E., Taddei, F., Malandrino, A., Schotkamp, T., Baleani, M., and Viceconti, M., 2008, "An Accurate Estimation of Bone Density Improves the Accuracy of Subject-Specific Finite Element Models," Journal of Biomechanics, **41**(11), pp. 2483–2491.

[131]   Gray, H. A., Taddei, F., Zavatsky, A. B., Cristofolini, L., and Gill, H. S., 2008, "Experimental Validation of a Finite Element Model of a Human Cadaveric Tibia," Journal of biomechanical engineering, **130**(3), p. 031016.

[132]   Carter, D. R., and Hayes, W. C., 1977, "The Compressive Behavior of Bone as a Two-Phase Porous Structure," J Bone Joint Surg Am, **59**(7), pp. 954–962.

[133]   Costa, M. C., Tozzi, G., Cristofolini, L., Danesi, V., Viceconti, M., and Dall'Ara, E., 2017, "Micro Finite Element Models of the Vertebral Body: Validation of Local Displacement Predictions," PLoS ONE, **12**(7), p. e0180151.

[134]   Hussein, A. I., Louzeiro, D. T., Unnikrishnan, G. U., and Morgan, E. F., 2018, "Differences in Trabecular Microarchitecture and Simplified Boundary Conditions Limit the Accuracy of Quantitative Computed Tomography-Based Finite Element Models of Vertebral Failure," J Biomech Eng, **140**(2).

[135] Boulanaache, Y., Becce, F., Farron, A., Pioletti, D. P., and Terrier, A., 2020, "Glenoid Bone Strain after Anatomical Total Shoulder Arthroplasty: In Vitro Measurements with Micro-CT and Digital Volume Correlation," Accepted in Medical Engineering & Physics.

[136] Knowles, N. K., Reeves, J. M., and Ferreira, L. M., 2016, "Quantitative Computed Tomography (QCT) Derived Bone Mineral Density (BMD) in Finite Element Studies: A Review of the Literature," Journal of experimental orthopaedics, **3**(1), p. 36.

[137] Jackman, T. M., DelMonaco, A. M., and Morgan, E. F., 2016, "Accuracy of Finite Element Analyses of CT Scans in Predictions of Vertebral Failure Patterns under Axial Compression and Anterior Flexion," Journal of Biomechanics, **49**(2), pp. 267–275.

[138] Chen, Y., Dall Ara, E., Sales, E., Manda, K., Wallace, R., Pankaj, P., and Viceconti, M., 2017, "Micro-CT Based Finite Element Models of Cancellous Bone Predict Accurately Displacement Once the Boundary Condition Is Well Replicated: A Validation Study," Journal of the mechanical behavior of biomedical materials, **65**, pp. 644–651.

[139] Ingram, D., Engelhardt, C., Farron, A., Terrier, A., and Mullhaupt, P., 2015, "Muscle Moment-Arms: A Key Element in Muscle-Force Estimation," Computer methods in biomechanics and biomedical engineering, **18**(5), pp. 506–13.

[140] Ingram, D., Engelhardt, C., Farron, A., Terrier, A., and Mullhaupt, P., 2016, "Improving Anterior Deltoid Activity in a Musculoskeletal Shoulder Model - an Analysis of the Torque-Feasible Space at the Sternoclavicular Joint," Computer methods in biomechanics and biomedical engineering, **19**(4), pp. 450–63.

[141] Engelhardt, A., 2015, "Effect of Anatomic Parameters on Degenerative Shoulder Diseases," Doctoral Thesis, Ecole Polytechnique Fédérale de Lausanne, Switzerland.

[142] Wu, G., van der Helm, F. C. T., Veeger, H. E. J., Makhsous, M., Van Roy, P., Anglin, C., Nagels, J., Karduna, A. R., McQuade, K., Wang, X., Werner, F. W., and Buchholz, B., 2005, "ISB Recommendation on Definitions of Joint Coordinate Systems of Various Joints for the Reporting of Human Joint Motion—Part II: Shoulder, Elbow, Wrist and Hand," Journal of biomechanics, **38**(5), pp. 981–992.

[143] Zygote, 09Nov2017, "Zygote Anatomy Collection."

[144] Netter, 2015, *Atlas d'Anatomie Humaine*.

[145] Mancuso, M., 2020, "Evaluation and Robotic Simulation of the Glenohumeral Joint," Infoscience [Online]. Available: https://infoscience.epfl.ch/record/274270. [Accessed: 03-Oct-2020].

[146] Sarshari, E., 2018, "A Closed-Loop EMG-Assisted Shoulder Model," Infoscience [Online]. Available: https://infoscience.epfl.ch/record/256396. [Accessed: 18-Oct-2019].

[147] Garner, B. A., and Pandy, M. G., 2000, "The Obstacle-Set Method for Representing Muscle Paths in Musculoskeletal Models," Computer methods in biomechanics and biomedical engineering, **3**(1), pp. 1–30.

[148] Sarshari, E., Mancuso, M., Terrier, A., Farron, A., Mullhaupt, P., and Pioletti, D., 2020, "Muscle Co-Contraction in an Upper Limb Musculoskeletal Model: EMG-Assisted vs. Standard Load-Sharing," Computer Methods in Biomechanics and Biomedical Engineering, **0**(0), pp. 1–14.

[149] Sarshari, E., Mancuso, M., Terrier, A., Farron, A., Mullhaupt, P., and Pioletti, D., 2020, "Feasibility of an Alternative Method to Estimate Glenohumeral Joint Center from Videogrammetry Measurements and CT/MRI of Patients," Computer Methods in Biomechanics and Biomedical Engineering, **0**(0), pp. 1–10.

[150] Dumas, R., Cheze, L., and Verriest, J. P., 2007, "Adjustments to McConville et al. and Young et al. Body Segment Inertial Parameters," Journal of biomechanics, **40**(3), pp. 543–53.

[151] Terrier, A., 2014, "Measurements of Three-Dimensional Glenoid Erosion When Planning the Prosthetic Replacement of Osteoarthritic Shoulders," Bone Joint J, p. 6.

[152] Terrier, A., Ston, J., Dewarrat, A., Becce, F., and Farron, A., 2017, "A Semi-Automated Quantitative CT Method for Measuring Rotator Cuff Muscle Degeneration in Shoulders with Primary Osteoarthritis," Orthopaedics & traumatology, surgery & research : OTSR, **103**(2), pp. 151–157.

[153] Kikuchi, K., Itoi, E., Yamamoto, N., Seki, N., Abe, H., Minagawa, H., and Shimada, Y., 2008, "Scapular Inclination and Glenohumeral Joint Stability: A Cadaveric Study," Journal of orthopaedic science : official journal of the Japanese Orthopaedic Association, **13**(1), pp. 72–7.

[154]   Moor, B. K., Kuster, R., Osterhoff, G., Baumgartner, D., Werner, C. M., Zumstein, M. A., and Bouaicha, S., 2016, "Inclination-Dependent Changes of the Critical Shoulder Angle Significantly Influence Superior Glenohumeral Joint Stability," Clinical biomechanics, **32**, pp. 268–73.

[155]   Engelhardt, C., Farron, A., Becce, F., Place, N., Pioletti, D. P., and Terrier, A., 2017, "Effects of Glenoid Inclination and Acromion Index on Humeral Head Translation and Glenoid Articular Cartilage Strain," J Shoulder Elb Surg, **26**(1), pp. 157–164.

[156]   Tetreault, P., Krueger, A., Zurakowski, D., and Gerber, C., 2004, "Glenoid Version and Rotator Cuff Tears," J Orthopaed Res, **22**(1), pp. 202–207.

[157]   Privitera, D. M., Siegel, E. J., Miller, L. R., Sinz, N. J., and Higgins, L. D., 2016, "Glenoid Version and Its Relationship to Glenohumeral Instability and Labral Tears," Journal of shoulder and elbow surgery / American Shoulder and Elbow Surgeons ... [et al.], **25**(7), pp. 1056–63.

[158]   "Shoulder Osteoarthritis Causes, Symptoms, Treatments" [Online]. Available: https://www.webmd.com/osteoarthritis/shoulder-osteoarthritis-degenerative-arthritis-shoulder#2. [Accessed: 03-Oct-2020].

[159]   Abdul Wahab, A. H., Abdul Kadir, M. R., Kamarul, T., Harun, M. N., and Syahrom, A., 2016, "Analysis on Stress and Micromotion on Various Peg Fixation at Glenoid Implant," Tribology - Materials, Surfaces & Interfaces, **10**(1), pp. 26–32.

[160]   Wu, W., Lee, P. V. S., Bryant, A. L., Galea, M., and Ackland, D. C., 2016, "Subject-Specific Musculoskeletal Modeling in the Evaluation of Shoulder Muscle and Joint Function," Journal of biomechanics, **49**(15), pp. 3626–3634.

[161]   Gross, T., Pahr, D. H., and Zysset, P. K., 2013, "Morphology-Elasticity Relationships Using Decreasing Fabric Information of Human Trabecular Bone from Three Major Anatomical Locations," Biomechanics and modeling in mechanobiology, **12**(4), pp. 793–800.

[162]   Knowles, N. K., Langohr, G. D. G., Faieghi, M., Nelson, A. J., and Ferreira, L. M., 2019, "A Comparison of Density–Modulus Relationships Used in Finite Element Modeling of the Shoulder," Medical Engineering & Physics, **66**, pp. 40–46.

[163]   Mancuso, M., Arami, A., Becce, F., Farron, A., Terrier, A., and Aminian, K., 2020, "A Robotic Glenohumeral Simulator for Investigating Prosthetic Implant Subluxation," J Biomech Eng, **142**(1).

[164]   ASTM-F2028-14, "Standard Test Methods for Dynamic Evaluation of Glenoid Lossening or Disassociation."

[165]   Davies, J. P., O'Connor, D. O., Burke, D. W., Jasty, M., and Harris, W. H., 1988, "The Effect of Centrifugation on the Fatigue Life of Bone Cement in the Presence of Surface Irregularities," Clinical Orthopaedics and Related Research, (229), pp. 156–161.

[166]   Krause, W., Mathis, R. S., and Grimes, L. W., 1988, "Fatigue Properties of Acrylic Bone Cement: S–N, P–N, and P–S–N Data," Journal of Biomedical Materials Research, **22**(S14), pp. 221–244.

[167]   Murphy, B. P., and Prendergast, P. J., 2000, "On the Magnitude and Variability of the Fatigue Strength of Acrylic Bone Cement," International Journal of Fatigue, **22**(10), pp. 855–864.

[168]   CHAPPUIS, J., and EL BANNA, S., 2008, "Le Rôle Du Ciment En Orthopédie," Rev. méd. Brux, **29**(6), pp. 546–551.

[169]   Xiong, D., Gao, Z., and Jin, Z., 2007, "Friction and Wear Properties of UHMWPE against Ion Implanted Titanium Alloy," Surface and Coatings Technology, **201**(15), pp. 6847–6850.

[170]   Xiong, D., Yang, Y., and Deng, Y., 2013, "Bio-Tribological Properties of UHMWPE against Surface Modified Titanium Alloy," Surface and Coatings Technology, **228**, pp. S442–S445.

[171]   "Construct Gaussian Window Object - MATLAB - MathWorks Schweiz" [Online]. Available: https://ch.mathworks.com/help/signal/ref/sigwin.gausswin-class.html. [Accessed: 20-Oct-2020].

[172]   "The Shoulder Joint - Structure - Movement - TeachMeAnatomy."

[173]   Taghizadeh, E., Reyes, M., Zysset, P., Latypova, A., Terrier, A., and Buchler, P., 2016, "Biomechanical Role of Bone Anisotropy Estimated on Clinical CT Scans by Image Registration," Annals of biomedical engineering, **44**(8), pp. 2505–17.

Glossary

µCT	Micro Computed Tomography
2D	Two dimensions
3D	Three dimensions
ASP	Anatomical Shoulder Prosthesis
ASTM	American Society for Testing and Materials
aTSA	Anatomical Total Shoulder Arthroplasty
CHUV	Centre Hospitalier Universitaire Vaudois
CT	Computed Tomography
DOF	Degree of Freedom
DVC	Digital Volume Correlation
DVRT	Differential Variable Reluctance Transducers
EMG	Electromyography
EminPrin	Minimum Principal Strain
FE	Finite Element
GH	Glenohumeral
JRF	Joint Reaction Force
JRFa	Joint Reaction Force Amplitude
JRFe	Joint Reaction Force Eccentricity
MRI	Magnetic Resonance Imaging
MSM	Musculoskeletal Model
OC	Overcorrected Implants
PS	Patient-Specific
QCT	Quantitative Computer Tomography
RMSE	Root Mean Square Error
RSP	Reverse Shoulder Prosthesis
rTSA	Reverse Total Shoulder Arthroplasty
SA	Sensitivity Analysis
STD	Standard Implant
TSA	Total Shoulder Arthroplasty
VOI	Volume Of Interest

Curriculum Vitae

Name	Yasmine Meharzi Boulanaache
E-Mail	yasmine.boulanaache@gmail.com
Nationality	Swiss/Algerian
Place of birth	Berriane, Ghardaia, Algeria

EDUCATION

10.2015 – 11.2020	**Swiss Federal Institute of Technology Lausanne (EPFL)**
	PhD thesis "Overcorrected Implants for Anatomical Total Shoulder Arthroplasty". Doctoral Program in Mechanics (EDME). Supervisors: Prof. Dr. D. Pioletti and Dr. A. Terrier at Laboratory for Orthopedic Biomechanics (LBO).
02.2011-08.2014	**Swiss Federal Institute of Technology Zurich (ETHZ)**
	Master of science in Mechanical Engineering, major: Medical Engineering. Master Tutor: Prof. Dr. Jess Snedeker.
	Master thesis: Institute for Biomechanics and Schulthess Clinic, Zurich. Title: "Biomechanical comparison of anatomical and reverse Shoulder Arthroplasty". Supervisor: Prof. Dr. Stephen Ferguson.
02.2013-06.2013	**Imperial College London,** Department of Bioengineering
	Semester thesis: "Measuring strain in mouse bone using Digital Image Correlation".
10.2006 - 08.2011	**Swiss Federal Institute of Technology Zurich (ETHZ)**
	Bachelor of science in Mechanical Engineering, major: Biomedical Engineering
	Bachelor thesis: ETHZ, Institute of Biomechanics and Uniklinik Balgrist, Zurich. Title: "Separation of the cortical and trabecular structures for an enhanced continuum FE-Model of the human scapula". Supervisor: Dr. Philippe Favre. Advisor: Prof. Dr. Jess Snedeker.
01.07.2006	**Kantonsschule Wettingen**. Swiss bilingual (English/German) maturity with major in Applied Mathematics and Physics.

EMPLOYMENT HISTORY

10.2014-08.2015	**Schulthess Clinic, Zurich and Swiss Federal Institute of Technology Zurich (ETHZ)**: Research Assistant. Project "Biomechanical comparison of Shoulder Arthroplasty Design Variations". Supervisors: Prof. Dr. Stephen Ferguson (ETHZ), Dr. Laurent Audigé (Schulthess Clinic).
09.2012 – 12.2012	**Stryker,** Selzach, Switzerland: Biomechanical Lab (BML)

Execution of mechanical tests on different product and instruments (Insertion, pull-out, different bending tests, corrosion, sterilization, torque-to-failure tests), carrying out some projects autonomously. Preparation of testing samples using different machines (turning and milling machines, power tools). Documentation and writing of reports. General organization of the lab. Introduction to a wide range of products and instruments of the company.

02.2007 – 03.2007	**ABB**, Baden, Switzerland
	Lernzentren: Introduction to different machine tools: material processing, turning, milling, CNC-milling, brazing and soldering, welding.
	Alstom, Birr, Switzerland
	Turbomachinery Technology Center: Measurements of flow through burners
10.2004 – 10.2004	**Paul Scherrer Institut**, Villigen, Switzerland
	Laboratory of Atmospheric Chemistry: measurement of pollution levels in different types of tree leaves.

WORK EXPERIENCE, PART TIME

09.2013 – 09. 2014	**ETHZ**, Department Safety, Security, Health and Environment
	Part-time administrative job: creation of emergency exit plans and evacuation plans for ETHZ buildings using Autocad.
10.2010 - 01.2012	**ETHZ**, Institute for Mechanical Systems, Center of Structure Technologies and Institute for biomechanics.
	Yearly Teaching Assistant positions in "Engineering Design 1" (for 3rd semester mechanical engineers) and :"Mechanics in Biology and Medicine".

SCHOLARSHIPS

Since February 2016	**StartingDoc**: Mentoring Program for women starting their PhD in french-speaking swiss universities
Since March 2013	**Femtec** Alumna
Sept. 2011- March 2013	**Femtec**: Careerbuilding-Program for outstanding female students in engineering and natural sciences to prepare for leadership positions.
	Partners: ABB, BP Europa SE, Daimler AG, Deutsche Telekom AG, EADS, EnBW, E.ON AG, Porsche AG, Robert Bosch GmbH, Siemens AG and ThyssenKrupp AG.

ADDITIONAL SKILLS

Languages	**Arabic** and **French**: Mothertongue
	English: fluent
	German and **Swiss German**: fluent

PUBLICATIONS

ACCEPTED	**Y. Boulanaache**, F. Becce, A. Farron, D. Pioletti, A. Terrier. "Glenoid bone strain after anatomical total shoulder arthroplasty: In vitro measurements with micro-CT and dig-ital volume correlation". Medical Engineering & Physics, Volume 85, November 2020, Pages 48-54. Technical Note.
SUBMITTED	E. Sarshari, **Y. Boulanaache**, A. Terrier, A. Farron, P. Mullhaupt, D. Pioletti. "A Matlab toolbox for scaled-generic modeling of shoulder and elbow". Source Code for Biology and Medicine journal

CONFERENCE TALKS

2017	**Y. Meharzi**, K. Consendey, F. Becce, A. Farron, D. Pioletti, A. Terrier. "A parametric musculoskeletal model based on MRI and IN-VIVO measurements". European Society of Biomechanics, Seville, Spain
	Y. Boulanaache, S. Bergamin, F. Becce, A. Farron, D. Pioletti, A. Terrier "Overcorrected glenoid implants to prevent recurrent glenohumeral subluxation after total shoulder arthroplasty: a patient-specific finite element analysis". Société de Biomécanique, Reims, France
2018	**Y. Boulanaache**, G. Guell Bartrina, F. Becce, A. Farron, D. Pioletti, A. Terrier "Sensitivity analysis of a finite element model of shoulder arthroplasty" for Computer Methods in Biomechanics and Biomedical Engineering, Lisbon, Portugal
	Y. Boulanaache, E.Sarshari, F. Becce, A. Farron, P. Mullhaupt, D. Pioletti, A. Terrier "Effect of rotator cuff degeneration on glenohumeral force" for World Congress of Biomechanics, Dublin, Ireland
	Y. Boulanaache, E.Sarshari, F. Becce, A. Farron, D. Pioletti, A. Terrier."Overcorrected prosthesis design for total shoulder arthroplasty" for International Shoulder Group, Rochester, USA
2019	**Y. Boulanaache**, F. Becce, A. Farron, D. Pioletti, A. Terrier. "Digital Volume Correlation Method to Evaluate Glenoid Bone Deformation After Total Shoulder Arthroplasty". European Society of Biomechanics, Vienna, Austria

CONFERENCE POSTERS

2019	**Y. Boulanaache**, F. Becce, A. Farron, D. Pioletti, A. Terrier. "Micro-CT Imaging and Digital Volume Correlation to Evaluate Glenoid Deformation After Total Shoulder Arthroplasty". Computer Methods in Biomechanics and Biomedical Engineering. New York, USA